National Library of Canada
Acquisitions and Bibliographic Services Branch
395 Wellington Street
Ottawa, Ontario
K1A 0N4

Bibliothèque nationale du Canada
Direction des acquisitions et des services bibliographiques
395, rue Wellington
Ottawa (Ontario)
K1A 0N4

Your file Votre référence

Our file Notre référence

NOTICE

The quality of this microform is heavily dependent upon the quality of the original thesis submitted for microfilming. Every effort has been made to ensure the highest quality of reproduction possible.

If pages are missing, contact the university which granted the degree.

Some pages may have indistinct print especially if the original pages were typed with a poor typewriter ribbon or if the university sent us an inferior photocopy.

Reproduction in full or in part of this microform is governed by the Canadian Copyright Act, R.S.C. 1970, c. C-30, and subsequent amendments.

AVIS

La qualité de cette microforme dépend grandement de la qualité de la thèse soumise au microfilmage. Nous avons tout fait pour assurer une qualité supérieure de reproduction.

S'il manque des pages, veuillez communiquer avec l'université qui a conféré le grade.

La qualité d'impression de certaines pages peut laisser à désirer, surtout si les pages originales ont été dactylographiées à l'aide d'un ruban usé ou si l'université nous a fait parvenir une photocopie de qualité inférieure.

La reproduction, même partielle, de cette microforme est soumise à la Loi canadienne sur le droit d'auteur, SRC 1970, c. C-30, et ses amendements subséquents.

Canada

Design of a Parallel-Series Hybrid Electric Vehicle Using Multi-Objective Optimization Techniques

Petros Frantzeskakis

A Thesis

in

The Department

of

Mechanical Engineering

Presented in Partial Fulfillment of the Requirements
for the Degree of Master of Applied Science at
Concordia University
Montreal, Quebec, Canada

May 1994

National Library of Canada
Acquisitions and Bibliographic Services Branch
395 Wellington Street
Ottawa, Ontario
K1A 0N4

Bibliothèque nationale du Canada
Direction des acquisitions et des services bibliographiques
395, rue Wellington
Ottawa (Ontario)
K1A 0N4

Your file Votre référence

Our file Notre référence

THE AUTHOR HAS GRANTED AN IRREVOCABLE NON-EXCLUSIVE LICENCE ALLOWING THE NATIONAL LIBRARY OF CANADA TO REPRODUCE, LOAN, DISTRIBUTE OR SELL COPIES OF HIS/HER THESIS BY ANY MEANS AND IN ANY FORM OR FORMAT, MAKING THIS THESIS AVAILABLE TO INTERESTED PERSONS.

L'AUTEUR A ACCORDE UNE LICENCE IRREVOCABLE ET NON EXCLUSIVE PERMETTANT A LA BIBLIOTHEQUE NATIONALE DU CANADA DE REPRODUIRE, PRETER, DISTRIBUER OU VENDRE DES COPIES DE SA THESE DE QUELQUE MANIERE ET SOUS QUELQUE FORME QUE CE SOIT POUR METTRE DES EXEMPLAIRES DE CETTE THESE A LA DISPOSITION DES PERSONNE INTERESSEES.

THE AUTHOR RETAINS OWNERSHIP OF THE COPYRIGHT IN HIS/HER THESIS. NEITHER THE THESIS NOR SUBSTANTIAL EXTRACTS FROM IT MAY BE PRINTED OR OTHERWISE REPRODUCED WITHOUT HIS/HER PERMISSION.

L'AUTEUR CONSERVE LA PROPRIETE DU DROIT D'AUTEUR QUI PROTEGE SA THESE. NI LA THESE NI DES EXTRAITS SUBSTANTIELS DE CELLE-CI NE DOIVENT ETRE IMPRIMES OU AUTREMENT REPRODUITS SANS SON AUTORISATION.

ISBN 0-315-97634-9

Canada

ABSTRACT

Design of a Parallel-Series Hybrid Electric Vehicle Using Multi-Objective Optimization Techniques

Petros Frantzeskakis, M.A.Sc.
Concordia University

The objective of this thesis is to experimentally and analytically study and design a parallel-series Hybrid Electric Vehicle. A first order dynamic model, Laplace transform technique and TUTSIM computer programming were used to analyze the time response of several electric motors and controllers. The time response, power to cost ratio and overall electric drive efficiency were the criteria used in the selection of the electric drive unit. The results of constant current battery tests on several lead-acid batteries, namely Eastern-Penn RV31, Delco Voyageur 27FMF, Chloride 6EF7, Optima 800, and Eastern-Penn RV27 are presented. Furthermore, constant power tests results for two nickel-cadmium batteries (Saft Nife STM1.130 and Marathon 44SP100) along with the Eastern-Penn RV31 are presented. The Universal Battery Model was slightly modified and used to evaluate analytically the energy and power density of the RV31, STM1.130, and 44SP100 battery systems. Thereafter the analytical results of these batteries were compared with the experimental constant power battery test results. A mathematical model using governing vehicle dynamics equations was developed in the time domain for this investigation. The good agreement between the calculated and experimental results provided confidence to use the mathematical model for carrying out a multi-objective optimization on the electric drive system of the vehicle. The objectives investigated were specific energy, cost and cycle life of the battery system, range and acceleration. The mass of the battery pack, operating voltage of the electric drive system, specific energy density and final drive gear ratio were selected as design parameters. An experimental investigation was performed on the series mode of operation of the hybrid electric vehicle. The results of this investigation were used in the formulation of a multi-objective optimization procedure, which enabled the optimal tuning of the series mode of operation. The objective functions were net alternator power, fuel consumption, HC, NO_x, and CO exhaust gas emission products, while the governor lever position and speed of the internal combustion engine were the design parameters.

ACKNOWLEDGEMENTS

The author is deeply indebted to Dr. T. Krepec and Dr. S. Sankar, his two supervisors, for their guidance, support and understanding throughout the course of this research.

Furthermore, the author greatly appreciates the technical advise of his colleagues at the Concordia University Fuel Control Laboratory, namely Harry Kekedjian, Manoj Tummala, and Medhat Hanna.

Most of all, the author expresses the deepest gratitude to his father George, mother Maria, and sister Dimitra Frantzeskakis, as well as his fiancee Francine McMullen for their encouragement and understanding throughout the course of this work.

Finally, special thanks to the following granting agencies, whose funds made this investigation possible: "Fonds pour la Formation et l'Aide à la Recherche" (FCAR), " Natural Sciences and Engineering Resources Council Canada" (NSERC), and Energy Mines and Resources Canada.

TABLE OF CONTENTS

LIST OF FIGURES

LIST OF TABLES

NOMENCLATURE

A_f	- Frontal area of vehicle, m^2
AVD	- Allowable voltage drop for ultimate drain, A
C_d	- Drag coefficient
CMA	- Cir Mils Area
Cmn	- Minimum value of C(x), $
Cmx	- Maximum value of C(x), $
COE(x)	- CO exhaust gas emissions, %
COEmn	- Minimum value of COE(x), %
COEmx	- Maximum value of COE(x), %
Cost	- Cost of each energy system, $
C(x)	- Cost, $
d	- Diameter of electric driveshaft extension, m
DOD	- Battery depth of discharge, %
E_v	- Terminal load voltage, V
$F_a(s)$	- Aerodynamic drag force, N
F_{ac}	- Alternating force component, N
F_{am}	- Force developed by the Advance DC motor, N
F_{AD}	- Advanced DC total force on shaft extension, N
F_{AT}	- Force on the tension side of the Advanced DC electric motor, N
F_{AS}	- Force on the slack side of the Advanced DC electric motor, N
FC(x)	- Fuel consumption, ℓ/h

FCmn - Minimum value of FC(x), ℓ/h

FCmx - Maximum value of FC(x), ℓ/h

F_d - Damping coefficient of the differential, N·m·s

F_{dw} max - Maximum limitation of tractive effort, N

$F_{dw}(s)$ - Force developed by the electric motor, N

Feff - Effective damping coefficient, N·m·s

$F_f(s)$ - Drivetrain friction force, N

F_f - Damping coefficient of the flywheel, N·m·s

F_g - Damping coefficient of the sprocket ratio, N·m·s

F_{gi} - Damping coefficient of the gear ratio in the transaxle, N·m·s

$F_{inc}(s)$ - Climbing force, N

F_m - Damping Coefficient of the electric motor, F·m·s

$F_R(s)$ - Resultant force (Tractive Effort), N

$F_{resistive}$ - Total resistive force, N

$F_{ro}(s)$ - Rolling resistive force, N

F_S - Total force produced by the Solectria motor on shaft extension, N

Fsm - Force developed by the Solectria electric motor, N

F_{SS} - Force on the slack side of the Solectria electric motor, N

F_{ST} - Force on the tension side of the Solectria electric motor, N

Ftractive - Tractive effort Solectria and Advanced DC, N

F(x) - Multi-objective function

g - acceleration due to gravity, m/s^2

g_i - Inequality constraint on design parameters

HCE(x) - HC exhaust gas emissions, ppm

HCEmn - Minimum value of HCE(x), ppm

HCEmx - Maximum value of HCE(x), ppm

hcg - Center of gravity height, m

I_d - Battery discharge current, A

I_M - Idle mixture screw setting (ccw) rotational position, degree

I_{max} - Maximum current in the conductor, A

Iy - Second moment of area about y-axis, m^4

Iz - Second moment of area about z-axis, m^4

J_d - Inertia of gear ratio in differential, $kg \cdot m^2$

Jeff - Effective inertia, $kg \cdot m^2$

J_{fw} - Inertia of flywheel, $kg \cdot m^2$

J_g - Inertia of sprocket ratio, $kg \cdot m^2$

J_{gi} - Inertia of gear ratio in transaxle (i=1-5 gear), $kg \cdot m^2$

J_m - Inertia of electric motor (obtained by manufacturer), $kg \cdot m^2$

J_w - Inertia of the wheels, $kg \cdot m^2$

K - Copper constant

k_a - Surface factor

k_b - Size factor

K_b - Slope of torque speed graph, $N \cdot m \cdot s/rads$

k_c - Load factor

k_d - Temperature factor

k_e - Miscellaneous factor

k_f - Stress concentration factor

Kmn - Minimum value of K(x), Wh/kg

Kmx - Maximum value of K(x), Wh/kg

Kr - Increase in rolling resistance coefficient vs. vehicle speed, s/m

K_t - Torque constant, N·m/V

Kv - Velocity coefficient for closed loop speed control, V/m/s

kWh_B - Energy available in the battery system, kWh

K(x) - Specific energy, Wh/kg

L - Wheelbase, m

La - Armature inductance, μH

LF - Conductor loop length, m

m - Mass of the vehicle, kg

m_{AD} - Mass of the Advance DC electric motor, kg

M_B - Battery pack mass, kg

M_{Bn} - Nominal value of M_B, kg

m_{dd} - Differential driver gear mass, kg

m_{di} - Transaxle driver gear mass, kg

m_e - Electric motor sprocket mass, kg

Meff - Effective mass, kg

m_f - Flywheel mass, kg

m_m - Main shaft sprocket mass, kg

m_{pd} - Differential driven gear mass, kg

m_{pi} - Transaxle driven gear mass, kg

m_w - Mass of the wheel, kg

M_{WB} - Mass of vehicle without a battery pack, kg

m_y - Bending moment in the y-direction, N·m

m_z - Bending moment in the z-direction, N·m

n - Safety factor

N_f - Gear ratio in the differential

N_g - Electric drive final gear ratio (Solectria)

N_{ga} - Electric drive final gear ratio (Advanced DC)

N_{gi} - Gear ratio of the selected gear in the transaxle (i=1-5 gear)

N_{gn} - Nominal value of N_g

N_o - Overall gear ratio (No=Ng*Nf) (case 1)

Overall gear ratio (No=Ng*Ng1*Nf) (case 2)

NOE(x) - NO_x exhaust gas emission, ppm

NOEmn - Minimum value of NOE(x), ppm

NOEmx - Maximum value of NOE(x), ppm

N_{sp} - Parallel mode sprocket ratio

N_{wheels} - Number of wheels

P - Desired battery discharge power, W

P_{APUS} - Power of the Apu in series mode of operation, kW

P_{APUP} - Power of the Apu in parallel mode of operation, kW

P_{max} - Maximum battery peak power, W

PN(x) - Net alternator power, kW

PNmn	- Minimum value of PN(x), kW
PNmx	- Maximum value of PN(x), kW
Power	- Power required to maintain HEV at 72 km/h, kW
P_p	- Penalty parameter
Q	- Battery capacity as a function of calculated discharge current, A·h
r	- Wheel radius, m
Ra	- Armature resistance, Ω
Range	- Vehicle range, km
R_B	- Battery internal resistance, Ω
R_{eq}	- Equivalent resistance, Ω
R_i	- Calculted overall gear ratio for each gear (i=1st to 5th gear)
R_L	- Load resistance, Ω
Rmn	- Minimum value of R(x), km
Rmx:	- Maximum value of R(x), km
R_s	- Radius of driven sprocket, m
R(x)	- Range, km
r_{dd}	- Differential driver gear radius, m
r_{di}	- Transaxle driver gear radius, m
r_e	- Electric motor sprocket radius, m
r_f	- Flywheel radius, m
r_m	- Main shaft sprocket radius, m

r_{pd} - Differential driven gear radius, m

r_{pi} - Transaxle driven gear radius, m

S_E - Specific energy of the storage system, Wh/kg

$S_e^{'}$ - Endurance limit, N/m^2

S_e' - Endurance limit of a test specimen, N/m^2

S_{En} - Nominal value of S_E, Wh/kg

S_{yt} - Yield strength of SAE 1006 steel, N/m^2

sX(s) - Vehicle velocity, m/s

$s^2X(s)$ - Vehicle acceleration, m/s^2

t - time required to accelerate the vehicle to a speed of 72 km/h, s

T_{am} - Torque developed by the Advanced DC motor, N· m

Tmn - Minimum value of T(x), s

Tmx - Maximum value of T(x), s

Tm(s) - Torque developed by DC motor, N· m

Trange - Total obtainable range from the energy storage, km

TR(x) - Total range, km

TRmn - Minimum value of TR(x), km

TRmx - Maximum value of TR(x), km

T_s - Stall torque condition, N· m

T_{sm} - Torque developed by the Solectria motor, N· m

T(x) - Acceleration time, s

Va - Armature voltage to DC motor, V

V_{amax} - Maximum armature voltage, V

Vi - Voltage from throttle position sensor, V

V_{HEV} - Velocity of the HEV, m/s

Vimax - Maximum voltage from throttle position sensor, V

V_{OS} - Operating voltage of the electric drive system, V

V_{OSn} - Nominal value of V_{OS}, V

V_w - Wind velocity, m/s

V_y - Shear force in the y-direction, N

V_z - Shear force in the z-direction, N

w - Tract width, m

w_i - Weighting factor

W_{ICE} - Speed of ICE, rpm

WLFT - Weight Left Front Tire

WLRT - Weight Left Rear Tire

WRFT - Weight Right Front Tire

WRRT - Weight Right Rear Tire

X(s) - Vehicle position, m

y - Distance from component center of gravity to left front tire, m

z - Distance from component center of gravity to front axle, m

GREEK SYMBOLS

η - Battery efficiency

η_a - Alternator efficiency

η_e - Electric motor and controller efficiency

η_{ea} - Advanced DC electric motor efficiency as a function of rpm

η_{es} - Solectria motor efficiency as a function of rpm and torque

η_m - Mechanical drivetrain efficiency

η_{po} - Parallel configuration overall efficiency

η_{so} - Series configuration overall efficiency

Θ - Slope of the road surface, degree

ρ - Air density, kg/m^3

σ_a - Alternating stress component, N/m^2

σ_m - Total mean stress, N/m^2

σ_{my} - Mean stress in the y-direction, N/m^2

σ_{mz} - Mean stress in the z-direction, N/m^2

$\Phi(x)$ - Pseudo-objective function

τ - Electric motor time constant, ms

μ_{const} - Static coefficient of rolling resistance

μ_r - Coefficient of rolling resistance

μ_s - Coefficient of road adhesion

$\omega_m(s)$ - Electric motor speed, rad/s

$\omega(s)$ - Speed at the wheel of the vehicle, rad/s

1. INTRODUCTION

Hybrid electric vehicles, which use an electric drive system and a small internal combustion engine, have been investigated for the last three decades. In response to the 1973 and 1978 oil crises, the North American governments sponsored engineering research on hybrid vehicles from 1978 to 1984.

In recent years, the demand for fuel efficient and environmentally clean high performance vehicles has reached an all time high. The United States government's legislation, such as the Energy Policy Act of 1992, has set up an ambitious schedule for purchasing federal fleet cars and light trucks fuelled by alternative fuels namely, methanol, ethanol, compressed natural gas, liquefied petroleum gas and electricity. The main goal of this act is to reduce the pollutant contents in exhaust gas emissions, and improve fuel economy by promoting research and development in alternative fuels, and by imposing fuel consumption quotas. Fig. 1.1 outlines the magnitude of alternatively fuelled federal fleet vehicles which will be purchased during the next five years. By 1999, as many as 37 500 alternative fuel vehicles are projected to be purchased out of the 50 000 vehicles being replaced annually by the US federal government. Moreover, the California Air Resource Board has set its own initiatives which requires:

- 2% of the vehicles sold to be electric by 1998, and
- by 1997 all passenger vehicles which produce exhaust gases, must meet the ultra-low-emissions vehicle (ULEV) standards.

Vehicles must be capable of restricting emissions to less than 0.62 g/km of CO, 0.62 g/km of HC and 0.62 g/km of NOx emission levels, according to the ULEV standards.

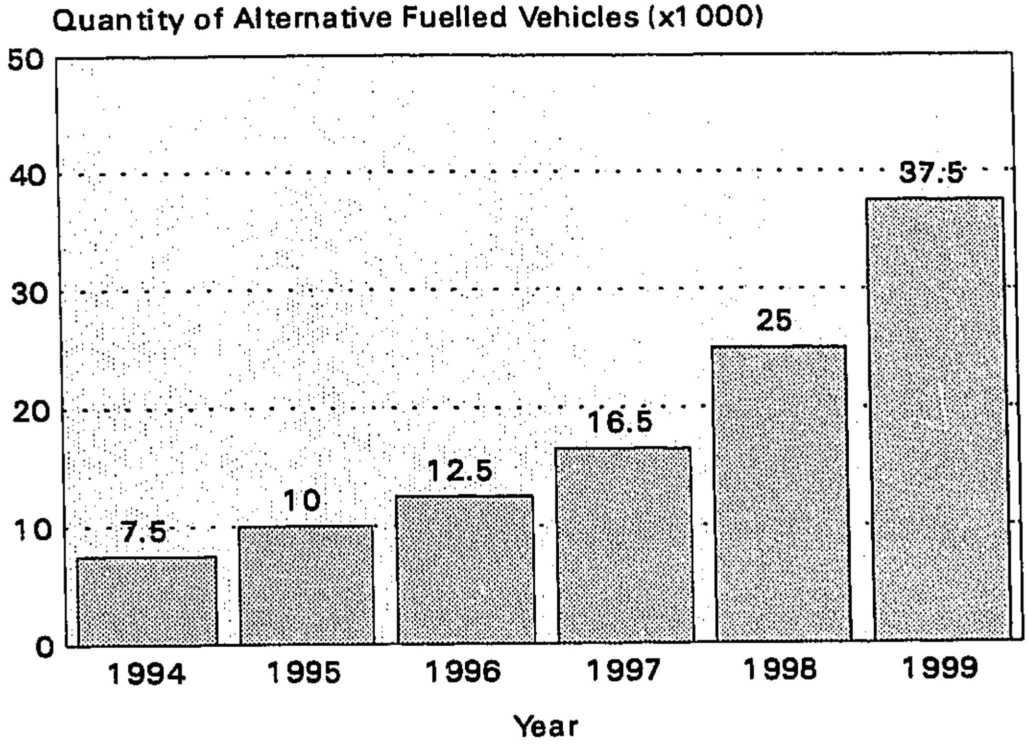

Fig. 1.1 Projected Alternatively Fuelled Federal Fleet Vehicles [1]*

The research work performed by USA automakers is therefore, stimulated by the expected zero-emission vehicle (ZEV) and ULEV regulations in the near future. Presently, pure electric vehicles (EVs) can achieve these requirements, however, their low range of operation limits their use. Hybrid electric vehicles (HEVs), on the other hand, offer a means of extending the range of electric vehicles by incorporating an auxiliary power unit.

---

[*] Numbers in brackets designate references, located at the end of the Thesis.

Hybrid electric vehicles combine two different drive systems, an internal combustion engine and electric motors. Basic HEV configurations can have parallel or series designs. The prime objective of such alternative vehicle concepts is to obtain as much advantages as possible from the various operating modes in order to compensate for the increase in expenditure, which is an inherent feature of HEVs.

In a series arrangement, electric motors provide the entire propulsion for the vehicle, while the battery system is recharged by a high performance engine-alternator unit. The alternator is most commonly coupled to an internal combustion engine (ICE), which operates on gasoline or an alternative fuel. In the parallel arrangement, the HEV utilizes simultaneously both or either one of the power plants to provide the propulsion (See Fig. 1.2).

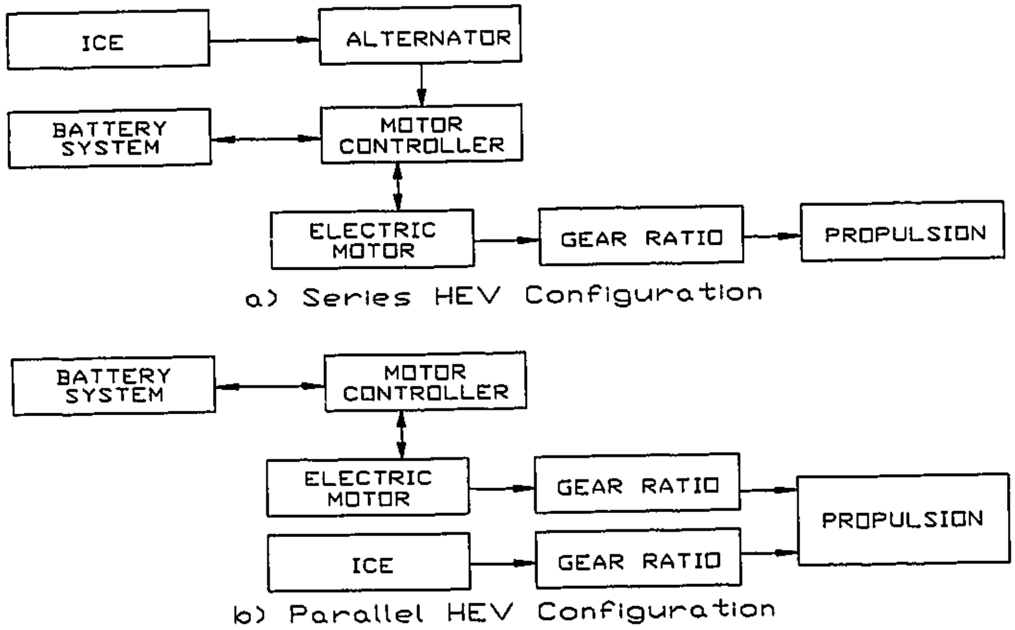

Fig. 1.2 Hybrid Electric Vehicle Configurations

In city traffic situations, where repetitive accelerating and stopping is quite common, a vehicle operating in ZEV mode, i.e., only using electric energy, is a perfect solution. The employment of such vehicles could effectively reduce the smog problems, which many industrialized nations are presently facing. The existence of the electric energy supply infrastructure would be a positive attribute in the use of such vehicles. To maximize the environmental benefits of this technology, electrical generation should be also derived from wind and hydro-electric power, and from electricity generating stations using cleaner fuels such as natural gas.

With this said, the battle to introduce HEVs is still very difficult, for they must be capable to perform at equivalent levels with the existing dedicated gasoline powered vehicles. Extensive research in this area is therefore required, if HEVs are to compete with today's gasoline fuelled vehicles, which have over one hundred years of research behind them.

The design of HEVs meets many challenges due to the volume and weight constraints of the electric power system. Other issues, such as high overall cost and slow recharging of the energy storage system must also be overcome. This research work will, therefore compromise on performance and minimization of cost, without sacrificing the vehicle's structural integrity and for this reason, an effective optimization technique must be employed.

2. HEVs: ADVANCEMENTS AND LITERATURE REVIEW

Steam, electric and gasoline as energies for propelling vehicles, were competing in the early 1900's, as the main sources of energy for transportation. Very soon, the internal combustion engine took a dramatic lead. However in 1919 there existed over 1.6 million gasoline powered vehicles, in comparison to 5000 electric vehicles. In the late 1970's, research activities for HEVs and EVs were increasing, mainly due to the upcoming energy crisis. Today, this work continues more for environmental reasons, and will be reviewed in a state of the art study which will cover the following topic areas: energy storage systems, electric motors and controllers, and hybrid electric vehicle configurations [2].

2.1 Energy Storage Systems: Review

In 1964, Shepherd [3] at the U.S. Naval Research Lab, made an effort to model the battery terminal conditions. This work was initiated by the recognition that a simple model would provide a computer-programmable means of analyzing various battery systems, at a minimal cost and time, in comparison with the in-depth experimental testing. Shepherd's equation try to analytically relate the electrochemical phenomena of lead-acid and nickel-cadmium batteries. This relationship was developed on the basis of low magnitude constant current discharges, which are impractical conditions for electric drives used in vehicles. The results of his model accurately represented lead-acid batteries, however it had a poor correlation for nickel-cadmium batteries.

Ragone [4], of Carnegie-Mellon University, presented in 1968 the relationships between battery characteristics and the automotive power source requirements, along with reviews of various traction battery systems. The importance of the specific energy of a battery was outlined as a requirement for providing the range, while the specific power was an aspect responsible for acceleration and for overcoming slopes on the road. It was for these reasons, experimental battery testing data were presented in the log-log graphs, correlating specific power and specific energy. Extensive results were presented for commercially available traction batteries such as, lead-acid, nickel-cadmium, silver-zinc and nickel-iron. Advanced battery systems were also reviewed, namely sodium-sulphur, lithium-chlorine, nickel-zinc and metal-air. Strict emphasis was placed on quoting the battery energy contents at 1 hour or shorter discharge rates. All the battery systems analyzed had one particular trend in common: as the power level consumption increases, the batteries energy level rapidly decreases in a nonlinear manner, mainly due to the internal resistance of the system and various polarizations that constitute irreversible energy losses.

Unnewehr et al. [5], in 1978 developed a Universal Battery Model, which was based on a simple equivalent circuit and applied to lead-acid, nickel-zinc, and sodium-sulphur cells. A good correlation was established with measured battery characteristics, although the results were less precise, in comparison to other more complex models. This simple technique demonstrated a rather conservative approach for comparing range and performance prediction for a wide variety of energy storage systems. Open circuit and short circuit experimental testing were required, along with the battery discharge rate, in order to complete the universal model analysis.

Hayden [6], outlined important battery management principles during his evaluation of the GTE Service Corporation electric fleet vehicles, in 1981. A detailed management regime was proposed for improving and maintaining the overall electric drive system. Although electric propulsion systems have limited range, his study found that the range EV's provide for fleet use is adequate, however, reliability and maintenance costs are the major problem. Solutions were proposed and implemented for the various problems, such as battery sulphation caused by protracted periods of disuse, insufficient electrolyte levels, and battery memory issue created by improper charging regimes.

The United States Research, Development and Demonstration Act of 1976, enabled the Department of Energy to establish test facilities and vehicle development programs that would render appropriate battery data for the optimization of new hybrid and electric vehicles. In 1982, an in-depth study and compilation of this research was published by Burke [7]. Test procedures and results from Argonne National Laboratories, Jet Propulsion Laboratory and General Electric Corporation Research and Development provided information of near term batteries, namely lead-acid, nickel-iron and nickel-zinc. Proper design and control of battery chargers were stated for near term and advanced batteries, with the objective of achieving longer cycle life. The optimum manner of charging a lead-acid system was to provide a constant current until a preset maximum voltage was established, and thereafter continue by tapering the charging current versus time.

From 1988 through 1990, a joint research and development venture between Powerplex and ASEA Brown Boveri (ABB) [8], [9], and [10], brought NaS batteries at an advanced state, as they demonstrated a vehicle range of 23 000 km without a failure. The dramatic improvement in reliability of this battery system called B11, was related to the conductive material. ABB and Powerplex, successfully replaced the glass electrolyte used in the past by Dow Chemical, with an ionic conductive ceramic called B-alumina, discovered by Ford Motor Company. The implementation of this new conductive material increased the average life cycle of the NaS batteries from 70 to 1000. The B11 consists of 100 cells connected in series, forming a sub-pack. In order to obtain higher energy levels, four sub-packs are thereafter connected in parallel. Unique, anti-fuse devices are used to bypass defective cells in the sub-packs. This enables them to continue to provide energy to the entire battery system. Over 200 tests in both laboratories and on-road vehicles, demonstrated the potential for large scale commercialisation. The BMW-E1 is one of these test vehicles using a 19 kWh NaS battery system, weighing 200 kg including the thermal management system.

In 1989, Reisner et al. [11], from Electrochemica Corporation presented a new electrochemical concept for nickel-zinc batteries. The main objective of this research was to correct the technical problems of this technology, namely low cycle life attributed to failure of the alkaline zinc electrode through modes of dendrite growth and shorting of the plates. A review of a 225 Ah Electrochemica vented Ni-Zn battery revealed a 600 life cycles at a 60% capacity retention, surpassing its predecessor which obtained only 200 cycles. In terms of cold weather performance, the Ni-Zn cells showed equivalent to Ni-Cd, which is considered by many experts the optimal all climate battery. This research work proved the feasibility of such a battery and demonstrated that Ni-Zn cells outperformed lead-acid, nickel-cadmium, and nickel-iron batteries in terms of energy density.

In 1993, Dickinson et al. [12], presented a publication outlining fundamental research on energy conversion and storage systems, obtained at the Center for Electrochemical Systems and Hydrogen Research, at Texas A&M University. An in-depth battery review in terms of energy and power density, along with physical and chemical properties were presented. An investigation on four lead-acid batteries, as well as three advanced battery systems, namely nickel-metal hydride, zinc-bromide and nickel-cadmium was performed. All performance characteristics were obtained based on industry accepted testing procedures.

Nickel-cadmium and nickel-metal hydride cells were found to have slightly higher specific energy density than lead-acid, with adequate power density, and an anticipated long cycle life. A driving cycle simulation was performed, using the test results as inputs. The Panasonic nickel-metal hydride battery outperformed all the other systems in terms of range.

2.2 Electric Motors and Controllers: Advancements

Resistance control was one of the first means of controlling a DC motor for electric vehicle applications. Several resistors were placed in parallel and series between the motor and the battery. Discrete changes in resistance were accomplished through the use of mechanical contactors, which were manually switched in order to achieve an increase or decrease in the vehicle's speed. This method of control was simple, however at the expense of efficiency and jerky motion of the drive system. The loss of vital electric energy in the resistors lead to the search of other control strategies [13].

A series control method replaced the resistance control strategy by integrating multiples of battery voltages in series with mechanical relays. If maximum acceleration was desired, the contactor linking all the voltage potential of the battery system would be used. Conversely in deceleration all the cells would be disconnected, resulting in a zero voltage potential on the motor. Although this method worked, uneven battery discharge occurred, due to the fact that the low voltages were used more often during the city driving conditions. This would render the drive system inoperable prematurely. To prevent the electric motor from overspeeding, caused by relays getting stuck, fuses were placed close to each battery in order to interrupt the electric current [13].

The undesirable features of the above control methods were solved by the introduction of high powered solid state devices, namely Silicon Controlled

Rectifiers (SCRs). Switching rates of 100 to 300 Hz from the SCR's made the DC chopper the most commonly used EV electronic controller, during the 1970's. In principle, the chopper switched the load from the battery system in an "on" "off" manner. As the DC voltage was passed across the inductor, a magnetic field would be generated. The amount of energy stored in the motor's inductor was limited, therefore the power delivered to the motor was minimal during the "off" time, explaining the need for fast switching. Three common chopper techniques were developed, pulsewidth modulation, frequency modulation and a combination of pulsewidth and frequency modulation. Pulsewidth modulation employed a constant frequency, while varying the "on" time. The next technique, frequency modulation would have a fixed "on" time while varying the chopper period. The last technique varied both, the "on" time and the chopping frequency [2], and [13].

In 1985, Slicker. et al. [14], of the Eaton Corporation Engineering and Research Center, presented a report on electric drivetrain developments from 1978 to 1984. The research was focused on an AC induction motor, an integrated inverter-charger and a real-time microprocessor based controller. The higher speed and specific power of the three phase induction motor outperformed the DC brush motors tested, however, the advantages were offset by the cost of the inverter. The pulsewidth modulation (PWM) employed parallel Darlington transistors per phase in the convention three phase bridge, instead of silicon controlled rectifiers. An 8-bit Motorola microprocessor controller was used to perform real-time closed loop control of the motor current, a digital slip control scheme and coordination of the gear shifting. The inverter was successfully transformed to work as a charger by using one of the bridge drive transistors. Charging efficiency of 80 % at full power was reported.

A dual DC chopper microcomputer controlled compact drive system was designed by Kahlen and Drumm [15], in 1989. A separately excited DC motor was developed with two groups of commuting poles, each connected to a chopper PWM bridge conducting half of the motor's load current. The dual chopper design had a higher overall efficiency than the single chopper design which was most commonly used to control DC motors.

Morris and Adams [16], from Chloride Electric Vehicle Division, illustrated in 1990 the design considerations and component selection for EV controllers. Silicon controlled rectifiers, were found to provide low voltage drops, at a relatively low cost and low current drive requirements. However, they suffered from noise intolerance, which causes them to switch at undesirable motor operating conditions. Two or three stage Darlington transistors were found to be the most appropriate compromise between cost, voltage drop and drive requirements. Insulated gate bipolar transistors IGBT, were more costly and had slightly higher saturation voltages than the latter. On the other hand, Metal Oxide Silicon Field Effect Transistors (MOSFETs) were found to be optimal for high frequency switching performance, but for high current and voltage application, such as electric drive system, the cost became an issue. Arrangements for providing regeneration, AC waveforms for motors without inverters, and three phase controllers for AC induction motors, were outlined in the publication.

Regenerative braking was realized during the early developments of shunt and compound motors. The kinetic energy during braking would be converted into electric energy and stored in the batteries. In 1992, Wyczalek [17], presented mathematical models aiding in the design of regenerative braking. He outlined three important modes in designing regenerative braking: service braking, programmable deceleration, and emergency braking. Savings of up to 20% during speeds of up to 10 m/s, and 6% for long steady speeds of 30 m/s were achieved through the use of a continuously varying transmission and effective programmable braking.

Presently, several electric drive manufacturer's are investigating rare earth magnets for the use in DC brush permanent motors, AC synchronous motors (brushless permanent magnet motors), AC induction motors and high performance alternators in the quest of achieving higher efficiency and power to weight ratio.

King et al. [18], in 1992 published developments of a 54 kW permanent magnet synchronous motor, an advanced Metal Oxide Silicon Controlled Thyristor (MCT), controller based three phase inverter and a microcomputer based inverter/motor controller. This work was made by a joint venture between General Electric, Ford Motor Company and Harris Semiconductors. This state of the art MCT inverter technology and permanent magnet motor using neodymium magnets, resulted in a 95% overall motor, inverter and controller efficiency. A

30% lower weight and higher tolerance to temperature changes, than the previous General Electric motor and controller were also demonstrated.

2.3 Hybrid Electric Configuration: Review

Ellers [19], Electronic Transportation Design reviewed hybrid electric vehicles in 1990, outlining the disadvantages of various HEV design configurations. He concluded that series configured HEVs had very low overall efficiency, while parallel configured HEVs had drivetrain synchronization problems. A dual drive shaft parallel HEV was proposed to be the most effective design configuration, which eliminated multi-shafts and expensive gear boxes. The proposed concept coupled the internal combustion engine to a rear differential, which would obtain a preset highway cruising speed. An electric motor connected to a transaxle provided the excellent city driveability. When the batteries were at a low state of charge, a fail safety alternator driven by the engine would provide charging to the energy system.

In 1992, Reuyl [20], Nevcor Inc., presented test results from a hybrid electric vehicle developed by the California Energy Commission, Electric Auto Association and faculty and students of Stanford University. The basic design objectives of the HEV were as follows: 1) to travel short city trips on battery power alone as a ZEV, and 2) on long trips to be capable of being certified as an ULEV. A series all DC electric drive hybrid vehicle was developed with the first objective being accomplished. The preliminary emission results suggested, that the constant speed and load use of the Norton Wankel rotary engine could result in the ULEV level. The development of the emission control strategy was on going at the time of publication.

In 1993, Ortech International [21], developed a simulation for analyzing hybrid electric drives. The data presented in this paper indicated that engine size optimization is pertinent in the development of a viable hybrid electric vehicle. Analytical analysis revealed 30% fuel economy improvements and significant reduction of emissions, by down sizing internal combustion engines in series hybrid vehicles. The four major conclusions in improving energy performance of HEV were, traction motor operation strategy, battery sizing, motor size and its control strategy and efficiency of mechanical components of the drivetrain, including the engine.

In 1993, the Concordia University Society of Automotive Engineers student branch converted a 1993 Ford Escort wagon to a hybrid electric vehicle. The vehicle consisted of the following components: a DC series wound electric motor, an AC synchronous electric motor, a Briggs and Stratton internal combustion engine, and a Fisher alternator. High overall electrical efficiency was obtained by only using the AC synchronous motor, during long distance trips. The DC series wound electric motor would only be activated in order to assist in the acceleration of the vehicle. In hybrid mode of operation the internal combustion engine could be operated in a parallel or a series configuration, with the aid of electronic controls. The feasibility of this vehicle was demonstrated in the 1993 Ford Hybrid

Electric Vehicle Competition, where it placed 3rd overall in the conversion class. The vehicle withstood rigorous experimental tests at the Ford Dearborn Proving Grounds, such as, stability, acceleration, gradability, range and safety to name a few [22].

3. THESIS OBJECTIVES AND METHODOLOGY

In late 1991, Concordia Society of Automotive Engineers (SAE) student branch, along with 67 other North American branches, presented Ford Motor Company with written proposals on HEVs. A total of 30 Universities, including Concordia University were granted entrance to the 1993 Ford Motor Company Hybrid Electric Vehicle Competition, which was sponsored in conjunction with the U.S. Department of Energy, and SAE. The task at hand was to successfully convert a 1992 Ford Escort station wagon into a hybrid electric vehicle. This Chapter outlines the objectives and methodology of this research work, which was performed during this course of time.

3.1 Research Objectives

The main objective of the research is to focus on the design and development of the Concordia HEV, as well as to investigate research support for the auxiliary power unit and electric drive system. After studying the subject, it was concluded that a combined parallel-series hybrid electric vehicle will be developed, instead of the conventional parallel or series HEVs. Close attention will be emphasized on the following design objectives: emissions of the auxiliary power unit, cost, overall efficiency, acceleration, and range.

The development of the proposed concept would lead to a HEV which could accomplish zero emission driving in electric mode of operation and ultra-low-emissions in hybrid mode of operation, with adequate vehicle performance.

3.2 Research Outline and Methodology

This research investigation will be presented in five main chapters which will outline the major areas in the development of a hybrid electric vehicle.

In Chapter 4, the functional requirements of the electric drivetrain will be discussed. A mathematical model in the frequency domain, will lead to the development of a system transfer function. This will be followed by simulations, which will aid in analyzing and selecting the electric drivetrain, excluding the energy storage system.

In Chapter 5, the outline of the proposed parallel-series hybrid electric configuration and the modes of operations will be presented. Sizing and selection of the engine and alternator will also be reviewed, along with the electrical control strategy.

In Chapter 6, analytical modelling for lead-acid and nickel-cadmium batteries will be presented and experimentally validated. Commercially available and advanced batteries will be represented by high order polynomial functions, and used in the multi-objective optimization work in Chapter 7.

In Chapter 7, the objectives for the optimization of the electric drive system will be established, followed by mathematical models and a simulation. Validation of the models will also be shown through experimental testing. Thereafter a design parameter analysis will be performed, followed by a multi-objective optimization using Hooke and Jeeves method.

In Chapter 8, an experimental investigation will be performed on the series mode of operation. The results of this investigation will thereafter be used to formulate a multi-objective optimization procedure. Consequently, the internal combustion engine will be tuned using the optimization results.

In Chapter 9, conclusions and recommendations for future work are discussed.

4. ELECTRIC DRIVE SYSTEM SELECTION

Prior to selecting an electric drive system, performance requirements must be established. These requirements serve as a means for analyzing various electric motors. An important dynamic requirement is acceleration, for it defines the maximum power of the electric motors. Another design criterion is overall motor and controller efficiency, which outlines how effectively the electrical energy is utilized. In the development of this vehicle, the following three objectives were used in the selection of the electric drive system:

- acceleration from 0 to 20.1 m/s within 15 seconds,
- minimum overall electric motor and controller efficiency of 90%, which would be analyzed at cruising speeds of 20.1 m/s, in terms of power consumption, and
- a maximum cost to power ratio of 450$/kW.

4.1 Scope of Analysis

Using modern control systems theory, a DC armature motor control model was derived in the frequency domain and used to perform TUTSIM [23] simulations. The response time of three different Permanent Magnet (PM) motors (also referred to as AC synchronous motors) and one series wound motor were analyzed, namely:

- 1 Unique Mobility SR180LC (DC brushless PM) peak power 45 kW,

- 1 Unique Mobility SR218L (DC brushless PM) peak power 90 kW,
- 2 Solectria BRLS16 (DC brushless PM) combined peak power 45 kW, and
- 1 Advanced DC 203-06-4001 (DC series wound) peak power 49 kW.

At this point, it should be explained that the selection of electric motors for such an application does not solely rely on matching the power needed to maintain the vehicle at a constant speed with the peak obtainable power of an electric motor. If such an approach is taken the power of the motor, required to maintain the vehicle speed at 100 km/h would be approximately 15 to 20 kW. However, the acceleration of the vehicle would be very poor and would neither meet the demands of this competition nor that of a typical driver.

The AC induction motors, were found to be the least expensive, next to series wound motors. However, when the complete AC drive system, such as the AC induction motor, controller and inverter was reviewed, it was found to be a very expensive package. Also in terms of electrical efficiency, brushless PM motors are capable of achieving higher peak efficiencies than AC induction systems. This is mainly due to the fact that AC induction systems are penalized for the DC to AC conversion performed by the on-board inverter. High powered AC induction systems developed for EVs operate at very high voltages which require a DC supply anywhere from 200 to 400 volts. In order to obtain these voltages two inherent parameters namely, weight and volume must be included into the design equation. Since, HEVs are very complex and are constrained by weight and available space, the AC induction systems become an unattractive option and were not further considered as potential candidates for the HEV project. The specification of the investigated electric motors is included in Appendix 1.

4.1.1 Modelling of a DC Armature Control Motor

A mathematical model in the frequency domain was developed for a DC armature control motor. This modelling approach was utilized to investigate the whole electric drive system. Fig. 4.1 outlines the general DC armature control schematic.

The force produced by the electric motor is controlled by the input voltage to the controller. A potentiometer on the accelerator pedal provides this control signal. The voltage at the armature of the DC motor can therefore be written as follows:

$$Va = \frac{Vi}{Vimax} \quad \textit{(open loop speed control)} \tag{4.1}$$

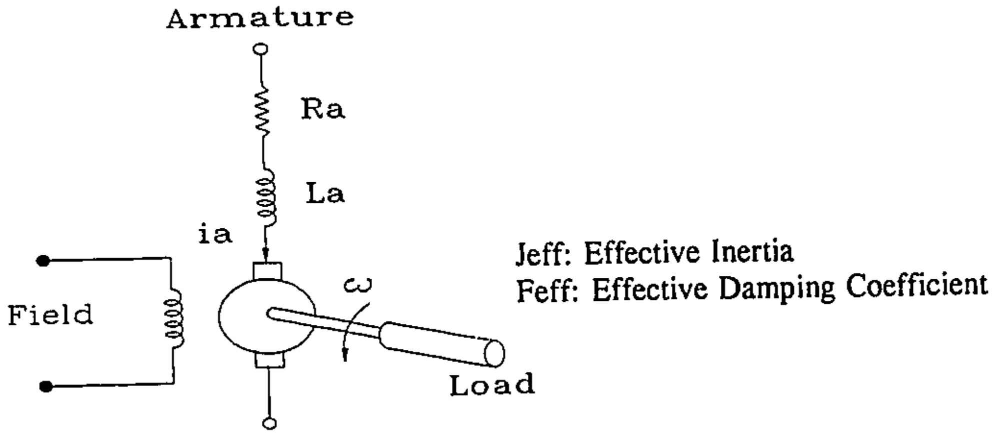

Fig. 4.1 Schematic of an Armature Controlled Motor [24]

The velocity feedback of the open loop speed control is provided by the driver of the vehicle. The torque developed by the motor is expressed as follows:

$$Tm(s) = \left(\frac{1}{1+\frac{La}{Ra}s}\right)(Kt\cdot Va-Kb\cdot\omega_m(s)) \qquad (4.2)$$

The electric motor speed is obtained by the following expression:

$$\omega_m(s) = \frac{R}{r}(sX(s)) \qquad (4.3)$$

where:

Vi - Voltage from throttle position sensor (V)

Vimax - Maximum voltage from throttle position sensor (V)

Va - Armature voltage to DC motor (V)

Kb - Slope of torque speed graph (N·m·s/rad)

Kt - Torque constant (N·m/V)

Ra - Armature resistance (Ω)

La - Armature inductance (μH)

Tm(s) - Torque developed by DC motor (N·m)

R or No - Overall gear ratio

r - Wheel radius (m)

The DC motor is represented by a first order differential equation, where La/Ra is the electrical time constant. The relationship between torque and armature voltage is assumed proportional by the torque constant Kt. The torque constant of the electric motor is defined as follows:

$$Kt = \frac{T_s}{V_{amax}} \tag{4.4}$$

where:

T_s - Stall torque condition

V_{amax} - Maximum armature voltage

The stall torque defines the magnitude of torque which the motor produces at the instant the electric motor starts to rotate. Fig. 4.2 illustrates the torque versus speed characteristic of a Solectria BRLS16 motor at two different input voltages.

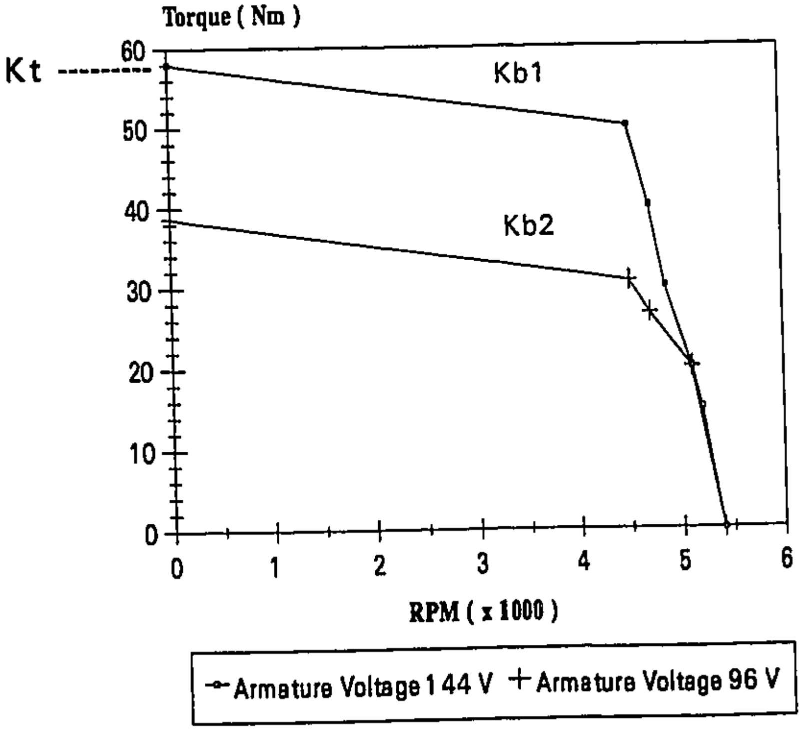

Fig. 4.2 Solectria BRLS16 - Torque Versus Speed Curve [25]

In general, the slope (Kb) of the torque versus speed curve is equal for various applied armature voltages. This is clearly shown in Fig. 4.2, where the slopes Kb1 and Kb2 are equal. However, as the armature voltage is varied, the magnitude of the stall torque changes accordingly. For example, the stall torque of the solectria motor at an armature voltage of 144 V and 96 V, is 58 N·m and 38.7 N·m, respectively. By applying this concept, an effective comparison was established among all the motors in question.

The force developed by the electric motor at the drive wheels, taking the efficiency of the drivetrain into account, can be expressed as:

$$F_{dw}(s) = \eta_m \frac{R}{r} Tm(s) \tag{4.5}$$

In order to obtain an accurate time response from the TUTSIM Simulations the disturbances of the system were defined. The general disturbances were represented by resistive forces which are made up of rolling resistance, aerodynamic drag, friction forces on the drivetrain and the climbing force due to the road grade. The expressions for these forces are represented in the frequency domain:

$$F_{ro}(s) = (\mu_{ro} + K_r \cdot sX(s))mg\,COS\theta \tag{4.6}$$

$$F_a(s) = \frac{1}{2}(sX(s) + V_w)^2 \rho C_d A \tag{4.7}$$

$$F_f(s) = \frac{Feff}{r^2}(sX(s)) \tag{4.8}$$

$$F_{inc}(s) = mg\,SIN\theta \tag{4.9}$$

The calculation of the effective damping coefficient (Feff) is outlined in equations (4.21) and (4.22). In Chapter 7, these equations will be represented in the traditional fashion, in the time domain.

The resultant force left to accelerate the vehicle, was found by subtracting the resistive forces from the force developed by the electric motor, as shown in the following expression:

$$F_R(s) = \sum F = F_{dw}(s) - F_a(s) - F_{ro}(s) - F_f(s) - F_{inc}(s) \tag{4.10}$$

A general relationship for road adhesion was used to limit the tractive effort of the electric motors. This expression was implemented in the simulation program as a limiting condition:

$$F_R(s) = \frac{mg}{2}\mu_s COS\theta \tag{4.11}$$

The acceleration of the vehicle was represented by:

$$s^2X(s) = \frac{F_R(s)}{m+\frac{Jeff}{r^2}} \tag{4.12}$$

The calculation of the effective inertia (Jeff) is outlined in equations (4.13) and (4.14).

The velocity was then determined by integrating the acceleration once and the displacement was thereafter established by integrating the velocity once. The generalized Control System Block Diagram is shown in Fig. 4.3, which outlines the forward path of the control system along with the disturbances.

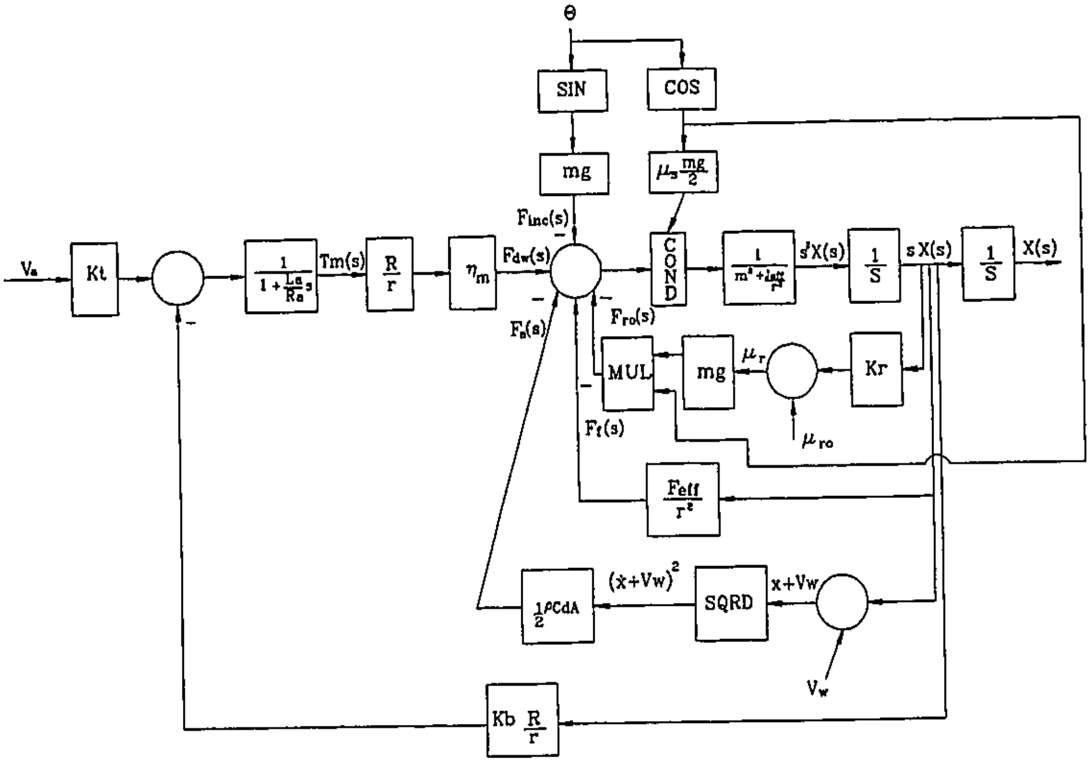

Fig. 4.3 Generalized Control System Block Diagram

4.1.2 Drivetrain Design Configuration

A fixed gear ratio drivetrain design configuration was compared to a multi-speed drivetrain configuration, with the aid of the established model and TUTSIM simulations. The preliminary design which was analyzed, incorporated a fixed gear reduction using a chain drive concept coupling the electric motor to a typical rear differential which had a fixed ratio of 3.54:1 (See Fig. 4.4).

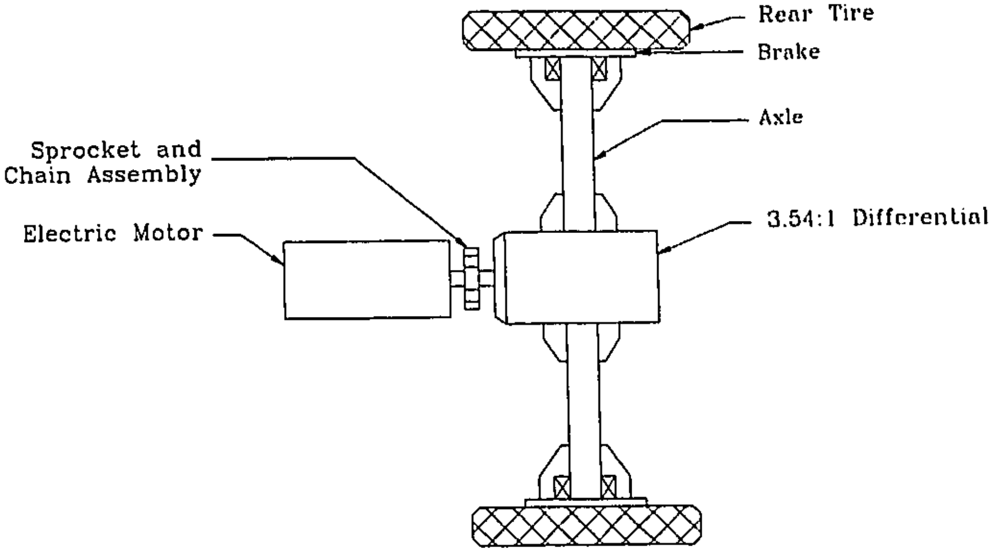

Fig. 4.4 Electric Motor Configuration - Single Speed

The next design configuration which was analyzed incorporated a five speed manual transmission that already exists in the 1992 Ford Escort. A simple lay-out of this configuration can be seen in Fig. 4.5.

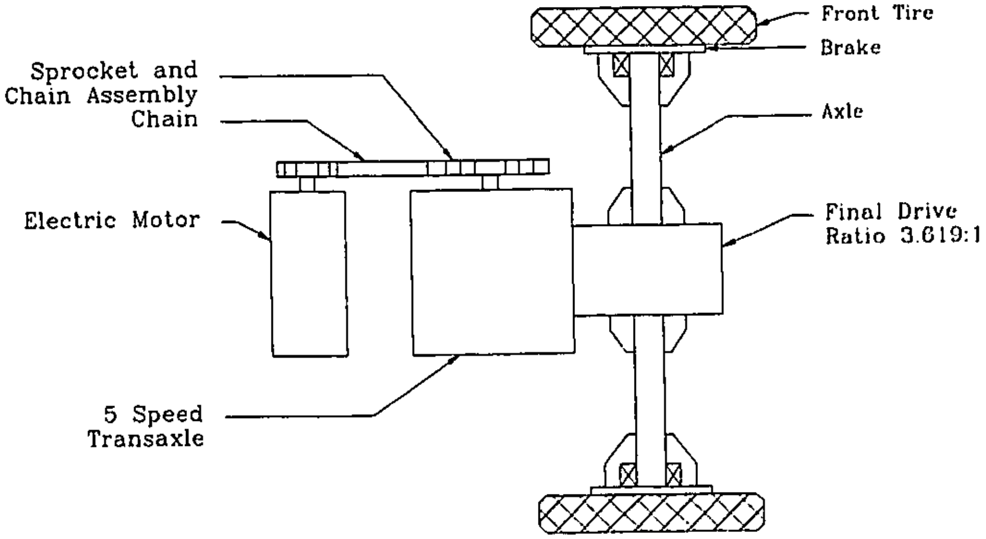

Fig. 4.5 Electric Motor Configuration - Five Speed Transaxle

4.1.3 Calculation of the Effective Inertia and Effective Damping Coefficient

The following equations were used to calculate the effective inertia and damping of each of the different electric drive systems. Case 1 represents the effective inertia of a fixed gear ratio design configuration, while case 2 represents the five speed design configuration.

Calculation of the effective inertia:

Case 1: (Fixed Gear Ratio)

$$Jeff = (J_m + J_g)(N_o)^2 + J_d(N_f)^2 + J_w \tag{4.13}$$

Case 2: (Varying Gear Ratio)

$$Jeff = (J_m + J_g)(N_o)^2 + (J_{fw} + J_{gi})(N_{gi} \cdot N_f)^2 + J_d(N_f)^2 + J_w \tag{4.14}$$

where:

Jeff: effective inertia
J_m: inertia of electric motor (obtained by manufacturer)
J_g: inertia of sprocket ratio
J_{fw}: inertia of flywheel
J_{gi}: inertia of gear ratio in transaxle (i=1-5 gear)
J_d: inertia of gear ratio in differential
J_w: inertia of the wheels
N_g: sprocket ratio
N_f: gear ratio in the differential
N_{gi}: gear ratio of the selected gear in the transaxle (i=1-5 gear)
N_o: overall gear ratio ($N_o = N_g * N_f$) (case 1)
N_o: overall gear ratio ($N_o = N_g * N_{gi} * N_f$) (case 2)

The inertia produced by the sprockets in the electric drive reduction was calculated as follows:

$$J_g = \frac{1}{2}(m_e \cdot r_e^2 + m_m \cdot r_m^2) \tag{4.15}$$

where:

m_e: electric motor sprocket mass
r_e: electric motor sprocket radius
m_m: main shaft sprocket mass
r_m: main shaft sprocket radius

Calculation of the inertia produced by the flywheel:

$$J_{fw} = \frac{1}{2}(m_f \cdot r_f^2) \tag{4.16}$$

where:

m_f: flywheel mass
r_f: flywheel radius

Calculation of the inertia produced by the selected gears in the transaxle:

$$J_{gi} = \frac{1}{2}(m_{pi} \cdot r_{pi}^2 + m_{di} \cdot r_{di}^2) \tag{4.17}$$

where:

m_{pi}: transaxle driven gear mass
r_{pi}: transaxle driven gear radius
m_{di}: transaxle driver gear mass
r_{di}: transaxle driver gear radius

Calculation of the inertia produced by the differential:

$$J_d = \frac{1}{2}(m_{pd}(r_{pd})^2 + m_{dd}(r_{dd})^2) \tag{4.18}$$

where:

m_{pd}: differential driven gear mass
r_{pd}: differential driven gear radius
m_{dd}: differential driver gear mass
r_{dd}: differential driver gear radius

Calculation of the inertia produced at the wheels:

$$Jw = \frac{1}{2} N_{wheels} \cdot M_w \cdot r^2 \tag{4.19}$$

where:

N_{wheels}: number of wheels
m_w: mass of the wheel

The effective inertia is thereafter used for calculation of the effective mass (Meff):

$$Meff = m + \frac{Jeff}{r^2} \tag{4.20}$$

Calculation of the effective damping coefficient:

Case 1: (Fixed Gear Ratio)

$$Feff = (F_m + F_g) \cdot N_o^2 + F_d \cdot N_f^2 \tag{4.21}$$

Case 2: (Varying Gear Ratio)

$$Feff = (F_m + F_g)N_o^2 + (F_f + F_{gi})(N_{gi} \cdot N_f)^2 + F_d \cdot N_f^2 \tag{4.22}$$

where:

F_m: damping coefficient of the electric motor (obtained by the manufacturer)

F_g: damping coefficient of the sprocket ratio

F_d: damping coefficient of the differential

F_f: damping coefficient of the flywheel

F_{gi}: damping coefficient of the gear ratio in the transaxle

The magnitude of the damping coefficient for both, the sprocket and differential, as well as the final drive ratio and the differential ratio is relatively small in comparison to the tractive effort, therefore it will be neglected without significant loss of accuracy. However, a drive-train efficiency will be incorporated in the TUTSIM simulation. The effective inertia and effective damping for each simulation will be calculated, since the inertia and damping of the different electric motors vary as well as the final drive ratio. The time constants of the four different electric motors were obtained from the manufacturer's specification data. The time constant of each of the investigated electric motors effectively outlined the sampling intervals of the respective system which was simulated. Table 4.1 provides a summary of the effective inertia and damping values, along with the electric motor time constant, which were used in the simulation.

Table 4.1 Summary of Effective Inertia and Effective Damping

Electric Motor	SR180LC	SR218L	2-BRLS16	203-06-4001
J_m (kg·m^2)	0.02260	0.04745	0.02000	0.03500
J_g (kg·m^2)	0.01185	0.01185	0.09130	0.00445
J_d (kg·m^2)	0.042	0.042	0.042	0.042
J_w (kg·m^2)	3.33	3.33	3.33	3.33
Jeff (kg·m^2)	6.457	7.630	6.686	4.648
Meff (kg)	1778	1792	1781	1756
F_m (N·m·s)	0.00437	0.00525	0.03339	0.03620
Feff (N·m·s)	0.206	0.248	0.849	1.778
Kt (N·m/V)	0.4000	0.7457	0.8055	1.129
Kb (N·m·s/rad)	0.00437	0.00525	0.03339	0.7275
τ (ms)	1.571	1.126	3.000	2.000
N_f	3.540	3.540	3.540	3.540
N_g	1.941	1.941	1.424	1.266
N_o	6.871	6.871	5.042	4.481

Since in case 2, each electric motor under consideration had five different gear ratios, the effective inertia calculations had to be repeated for each gear ratio, in order to obtain meaningful results. As in case 1, the damping of the electric motor was the only coefficient used in calculating the effective damping. The drive-train efficiency is taken into account for the remaining inherent damping. The parameters used in the modelling of the electric drive system using a five speed transaxle, are represented in Table 4.2 through Table 4.5.

Table 4.2 UNIQ SR180LC Drive System Incorporating a 5 Speed Transaxle

	1st Gear	2nd Gear	3rd Gear	4th Gear	5th Gear
Jeff (kg·m^2)	39.31	13.90	8.60	6.39	5.13
Jeff/r^2 (kg)	475	168	104	77	62
Meff (kg)	2175	1868	1804	1777	1762
Feff (N·m·s)	2.834	0.824	0.404	0.229	0.130
Gear Ratio R	25.467	13.732	9.617	7.240	5.450

Table 4.3 UNIQ SR218L Electric Drive Incorporating a 5 Speed Transaxle

	1st Gear	2nd Gear	3rd Gear	4th Gear	5th Gear
Jeff (kg·m^2)	55.43	18.59	10.90	7.69	5.87
Jeff/r^2 (kg)	670	225	132	93	71
Meff (kg)	2370	1925	1832	1793	1771
Feff (N·m·s)	3.405	0.990	0.486	0.275	0.156
Gear Ratio R	25.467	13.732	9.617	7.240	5.450

Table 4.4 BRLS16 Electric Drive Incorporating a 5 Speed Transaxle

	1st Gear	2nd Gear	3rd Gear	4th Gear	5th Gear
Jeff (kg·m^2)	42.92	14.96	9.12	6.69	5.30
Jeff/r^2 (kg)	519	181	110	81	64
Meff (kg)	2219	1881	1810	1781	1764
Feff (N·m·s)	19.494	5.668	2.781	1.579	0.893
Gear Ratio R	23.98	12.93	9.057	6.824	5.132

Table 4.5 Advanced DC 203-06-4001 and a 5 Speed Transaxle

	1st Gear	2nd Gear	3rd Gear	4th Gear	5th Gear
Jeff ($kg \cdot m^2$)	42.96	14.97	9.12	6.69	5.30
Jeff/r^2 (kg)	519	181	110	81	64
Meff (kg)	2219	1881	1810	1781	1764
Feff ($N \cdot m \cdot s$) if rpm > 3200	15.601	4.540	2.227	1.264	0.715
Gear Ratio R	20.76	11.199	7.843	5.909	4.444

4.2 TUTSIM Simulations

TUTSIM block diagrams were developed with the aid of the mathematical model and the generalized block diagram discussed previously. These diagrams served two general functions, namely:

- as a guide for programming in TUTSIM, and
- outlining the electric drive control system.

In this section two TUTSIM block diagrams, representing case 1 and case 2 of the design configurations, are illustrated in Fig. 4.6 and Fig. 4.7. Using these two block diagrams, TUTSIM simulations were developed for the fixed gear ratio and five speed transaxle design configurations.

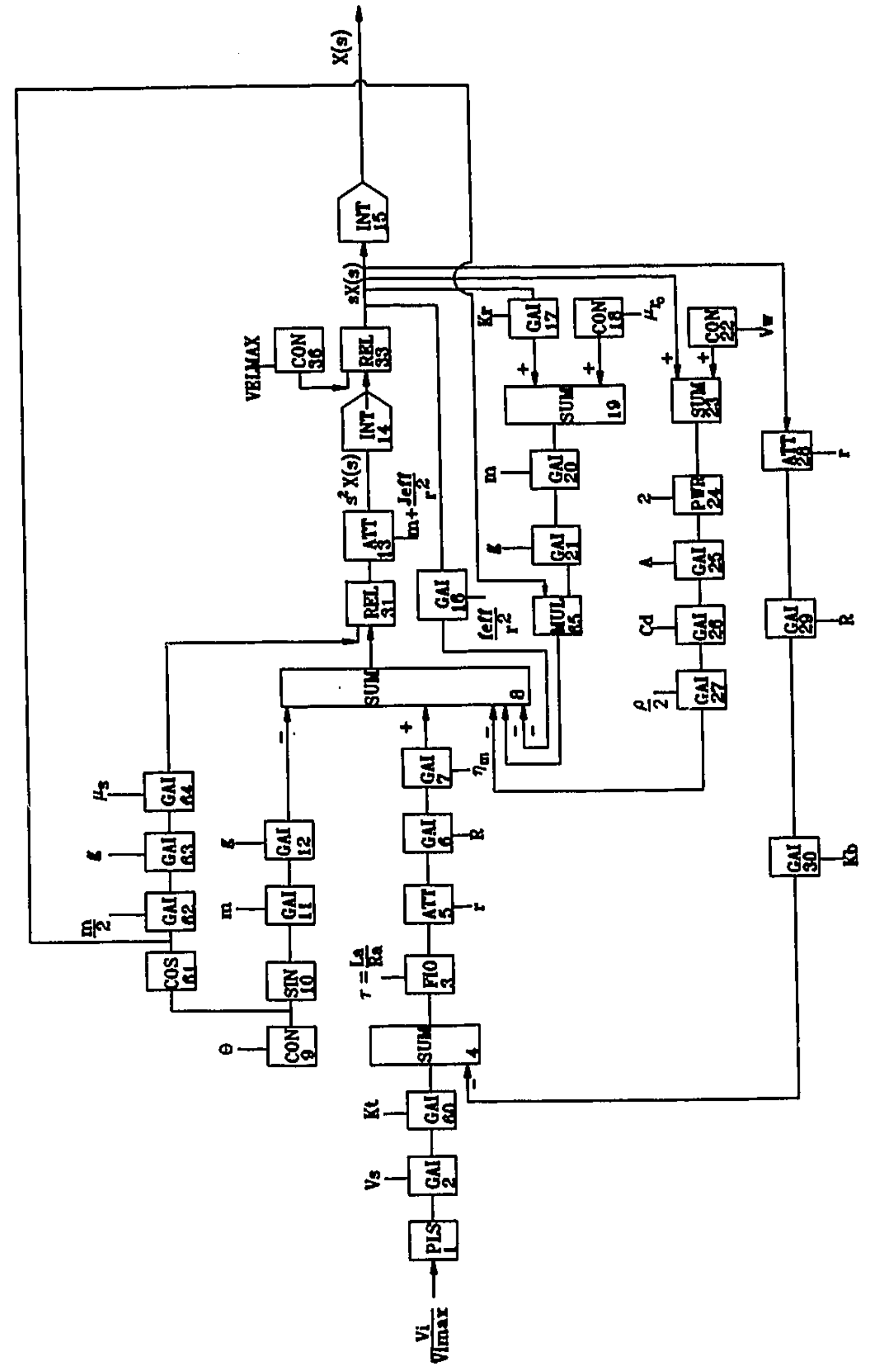

Fig. 4.6 TUTSIM Block Diagram Fixed Gear Ratio Design Configuration

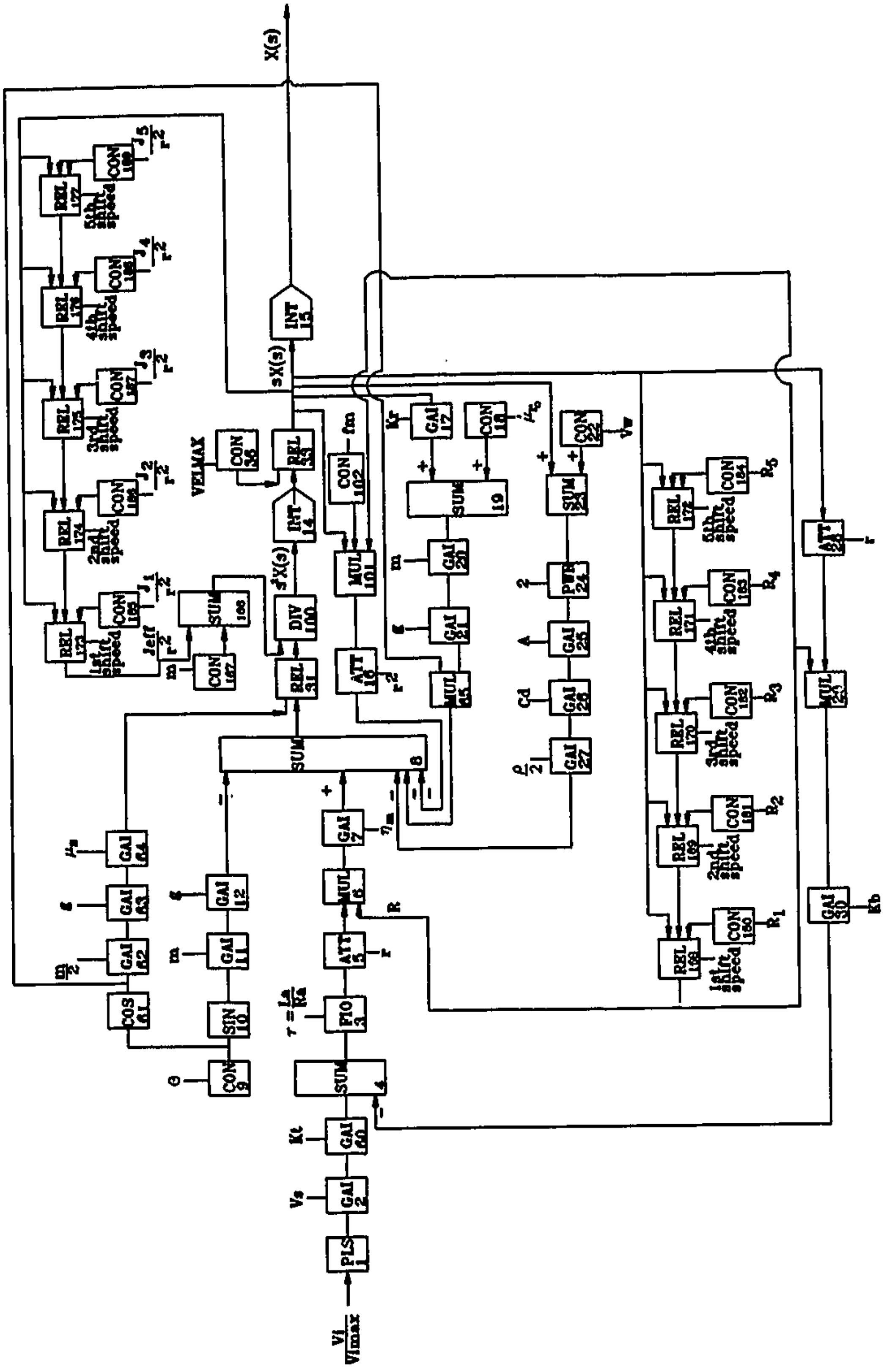

Fig. 4.7 TUTSIM Block Diagram Five Speed Design Configuration

Table 4.6 tabulates the nominal parameters which were used as input to the simulations, for both design configurations.

Table 4.6 Tabulation of Nominal Parameters used in the Simulations

r	- Wheel radius (m)	0.2876
m	- Mass of vehicle (kg)	1700
μ_{ro}	- Coefficient of rolling resistance	0.014
g	- Acceleration of gravity (m/s^2)	9.81
Kr	- Increase in rolling resistance coefficient vs. vehicle speed (m/s)	54.015E-06
Vw	- Face wind (m/s)	2.235
ρ	- Air density (kg/m^3)	1.202
C_d	- Drag coefficient	0.36
A	- Frontal Area of Vehicle (m^2)	1.979
μ_s	- Coefficient of friction (tire to ground)	0.80
η_m	- Mechanical efficiency	0.93

4.2.1 Fixed Gear Ratio Simulation Analysis

The open loop response of each of the single speed drive systems was analyzed based on a step input at the accelerator pedal and at a flat grade driving condition. Fig. 4.8 through 4.11. graphically display the TUTSIM simulation results, such as vehicle speed, rolling resistance, aerodynamic drag force and tractive effort versus time.

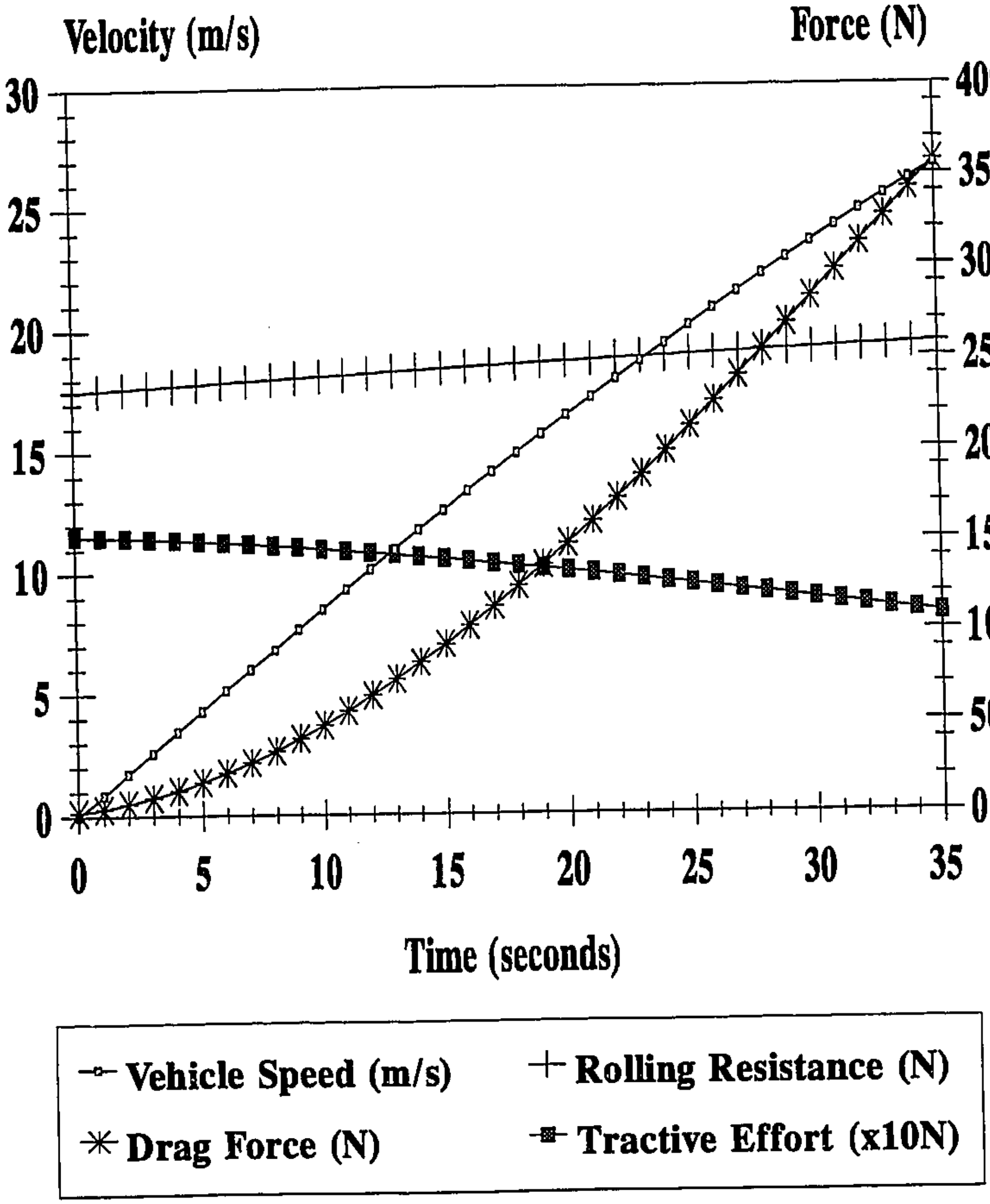

Fig. 4.8 System Response Using a UNIQ SR180LC Electric Motor

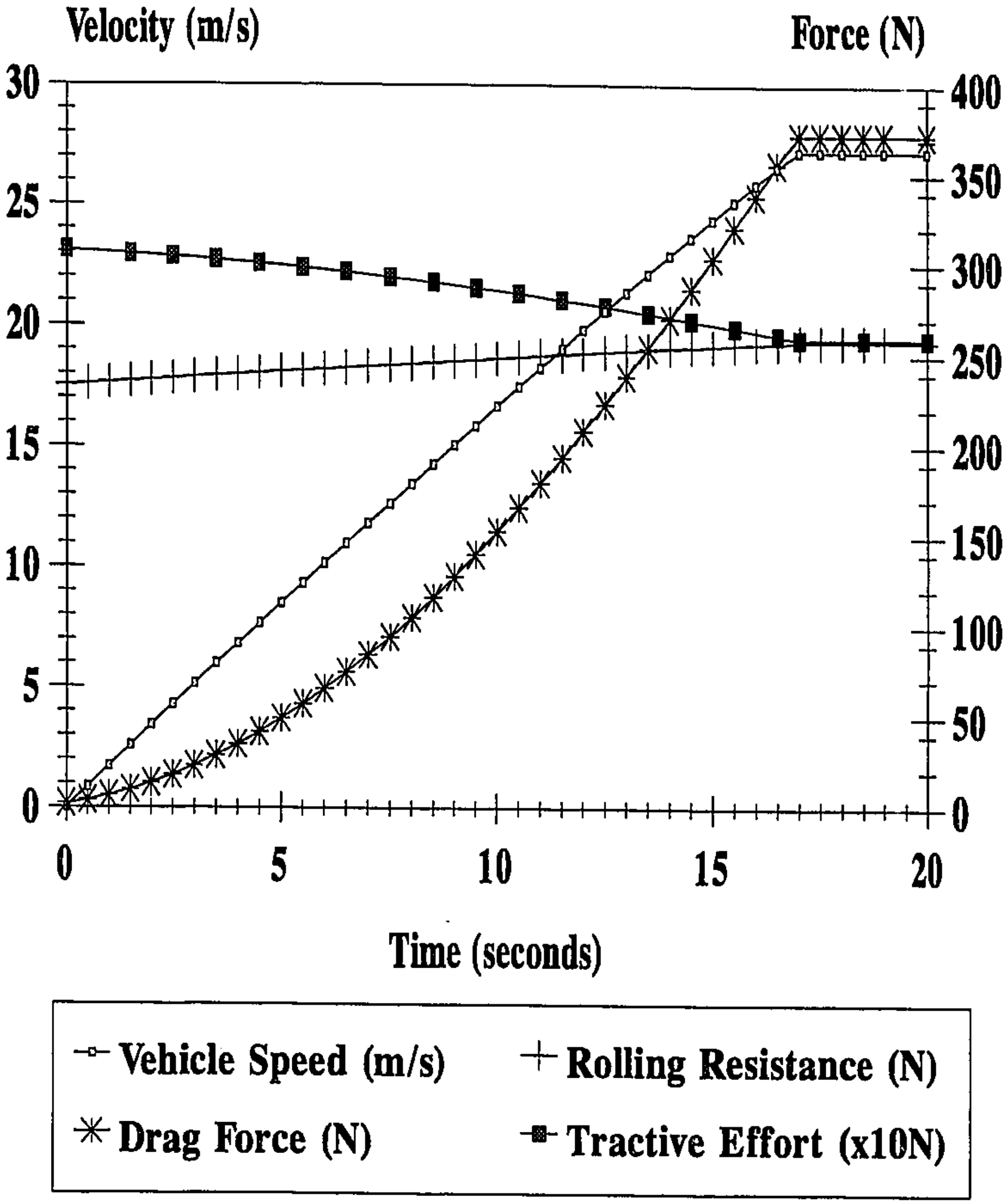

Fig. 4.9 System Response Using a UNIQ SR218L Electric Motor

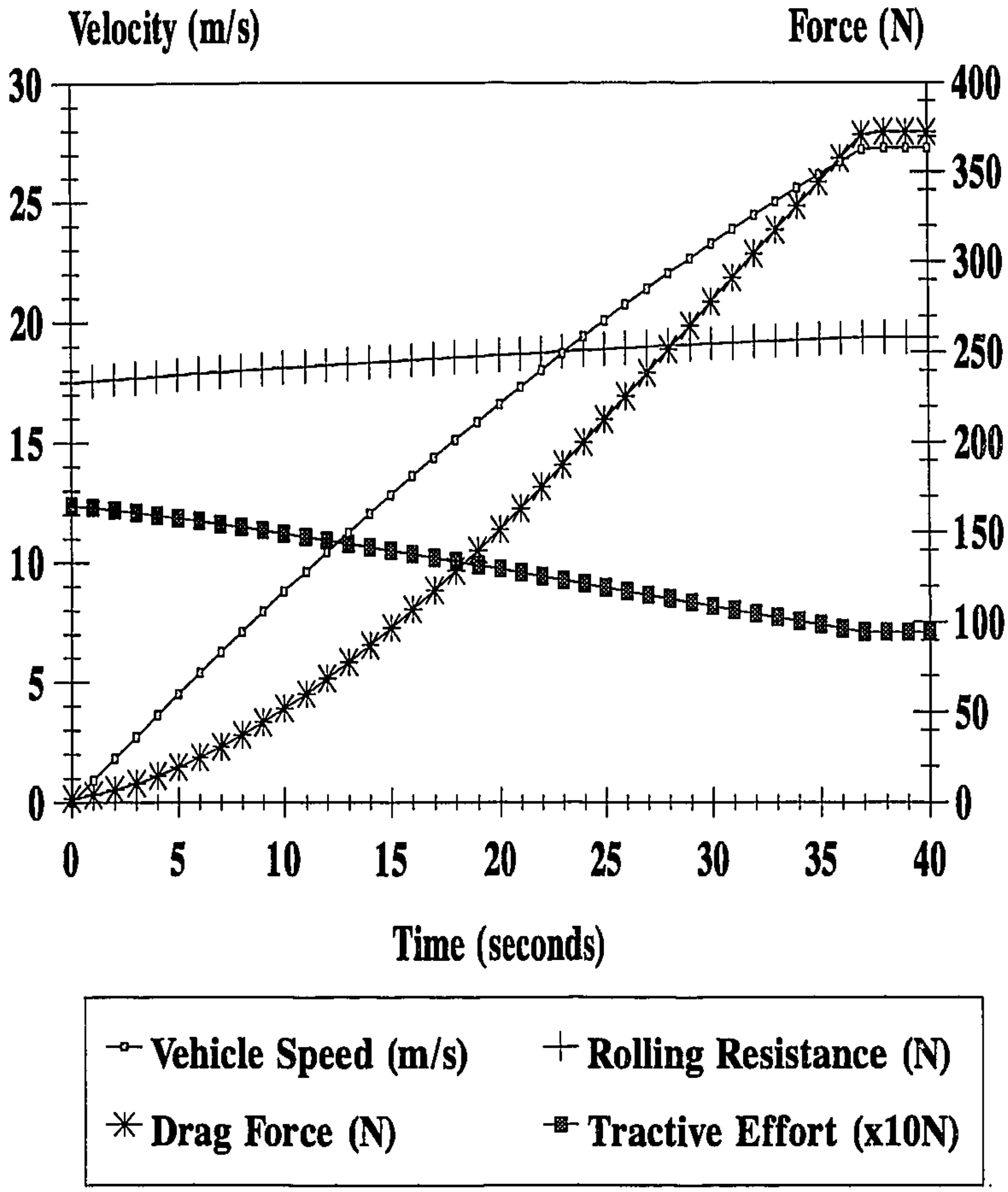

Fig. 4.10 System Response Using 2 Solectria BRLS16 Electric Motors

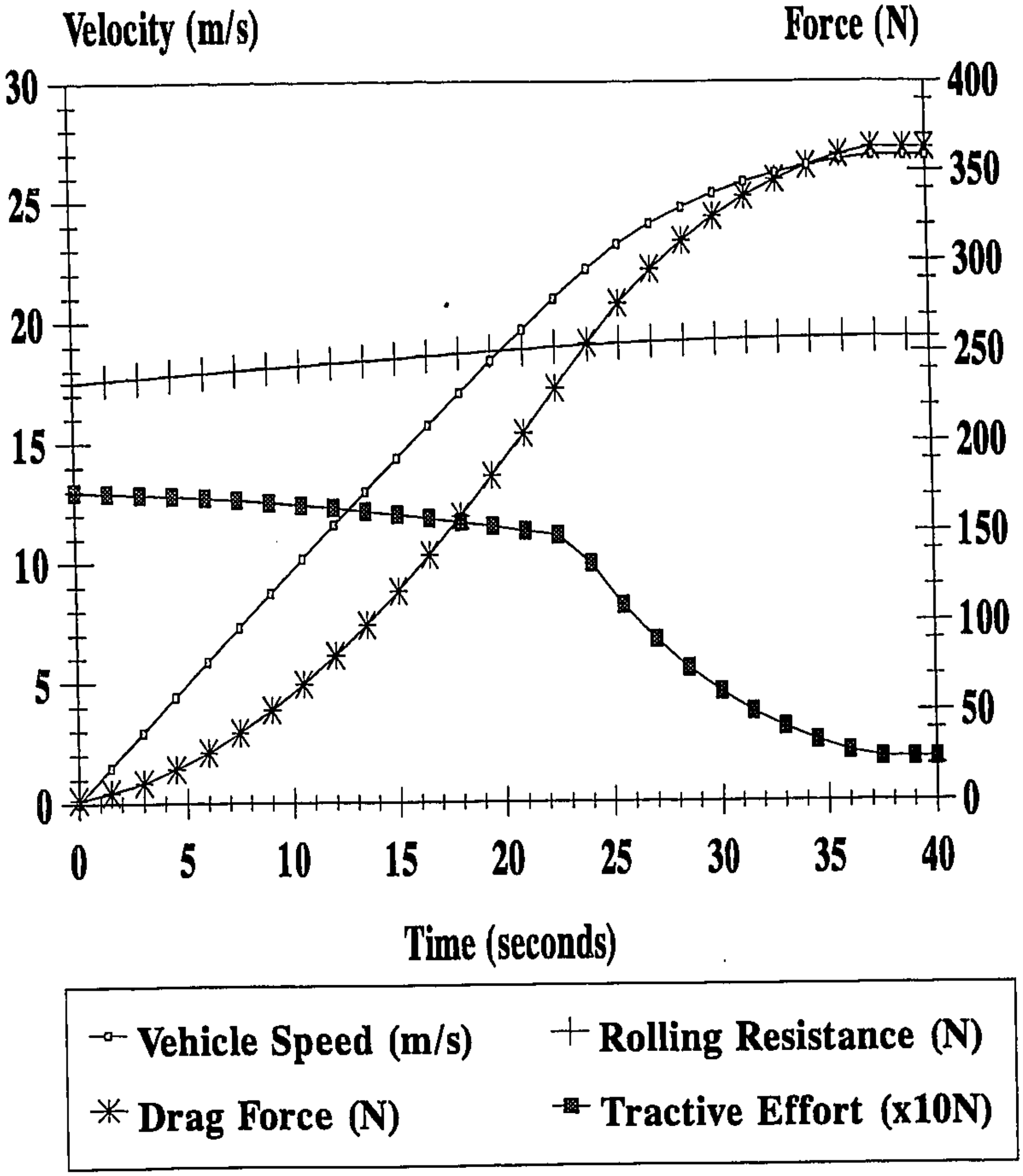

Fig. 4.11 System Response Using an Advanced DC 203-06-4001 Electric Motor

In order to analyze the steady state power consumption, at 20.1 m/s for each of the electric drive systems, the torque developed by the motor is considered, along with the corresponding electric drive efficiency. In this context, the electric drive efficiency includes both, the electric motor and controller efficiency, which is obtained from the electrical efficiency map provided by the manufacturers (See Appendix 1). With the aid of the TUTSIM simulation, the steady state torque required for maintaining the 1700 kg HEV at 20.1 m/s, is calculated by taking the values of aerodynamic drag and rolling resistance, and using them in the following expression:

$$Tm(s) = \frac{r(F_a(s)+F_{ro}(s))}{R\cdot\eta_m} \tag{4.23}$$

Each system has a different electric efficiency for the torque and speed at which it is operating and therefore, the power consumption for each case is calculated, using:

$$P_c = \frac{Tm\cdot\omega_m(s)}{\eta_e} \tag{4.24}$$

A summary of the simulation results outlined in Fig. 4.8 through Fig. 4.11, is presented in Table 4.7 in terms of acceleration time and steady state power consumption at 20.1 m/s for each drive system. From these results, we see that the only electric drive system that met the acceleration requirements is the UNIQ SR218L, while having a 10.9 kW power consumption.

Table 4.7 Summary of the Fixed Gear Ratio Drive System Simulation Results

Electric Motor	(0-20.1 m/s) Acceleration Time (s)	Tm Motor Torque (N·m)	ω_m (rad/s)	η_e	Power Consumption (kW)
UNIQ SR180LC	25.1	20.9	480.4	0.93	10.80
UNIQ SR218L	12.2	20.9	480.4	0.92	10.9
2-Solectria BRLS16	25.0	28.5	352.5	0.91	11.04
Advanced DC 203-06-4001	21.6	32.1	313.3	0.86	11.78

4.2.2 Simulation Analysis of the Five Speed Transaxle Design Configuration

The gear ratio's of the five speed transaxle were introduced to each electric motor under consideration. A similar step input was used to simulate the potentiometer signal, from the acceleration pedal. The open loop response for each system, under 0% grade is outlined in Figs. 4.12 to 4.15.

An improvement in tractive effort is clearly demonstrated by incorporating five speed transaxle. The series of steps caused by the gear changes result in a larger magnitude of tractive effort in comparison to the fixed gear ratio simulations. This large magnitude is translated into an improvement in acceleration time. A similar methodology as in Section 4.2.1 was used in calculating the steady state power consumption of each of the electric drive systems. A summary of the acceleration results, motor torque and speed, electrical efficiency, and power consumption for the various electric drive units is presented in Table 4.8.

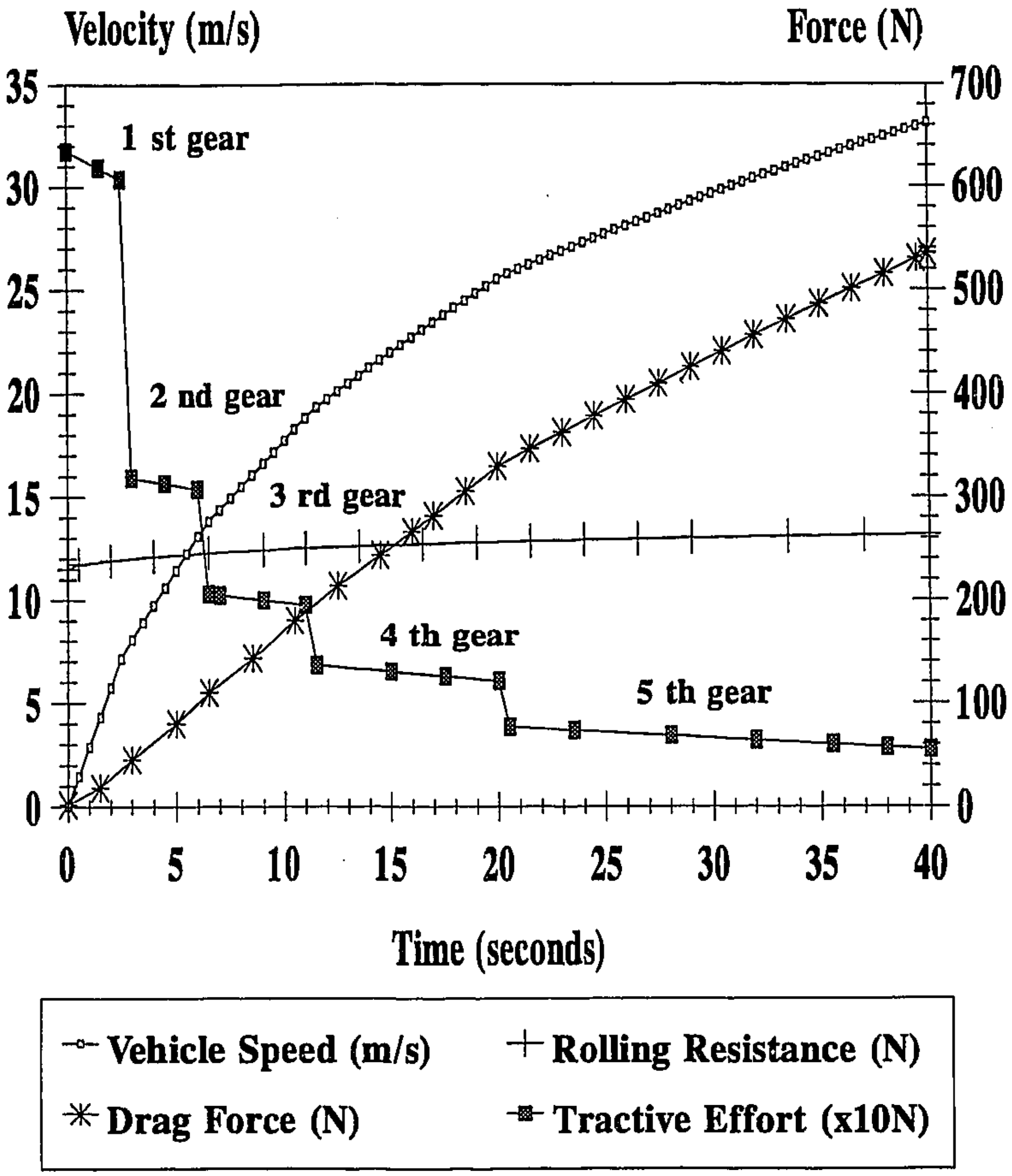

Fig. 4.12 System Response - 5 Speed Transaxle UNIQ SR180LC Electric Drive System

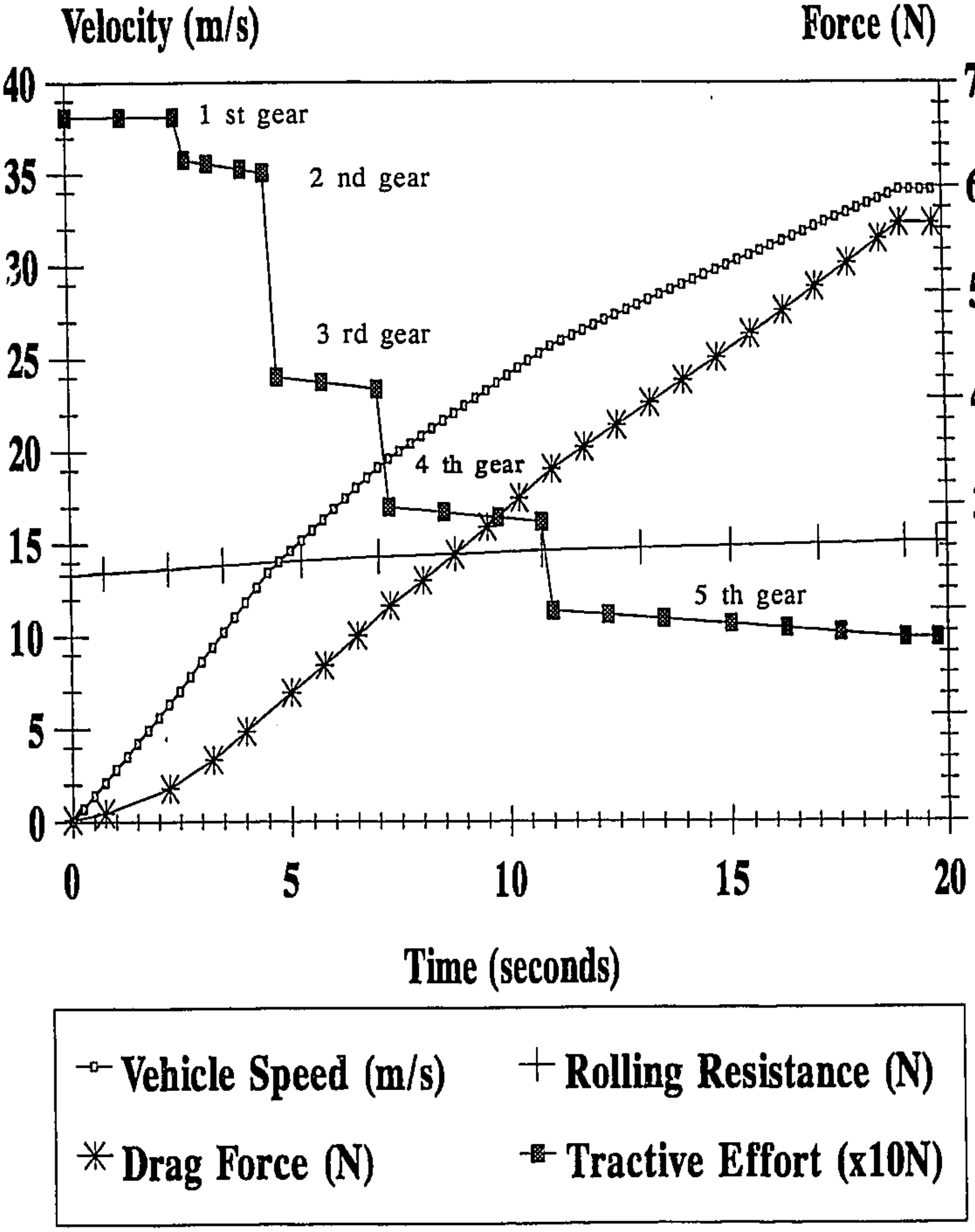

Fig. 4.13 System Response - 5 Speed Transaxle UNIQ SR218L Electric Drive System

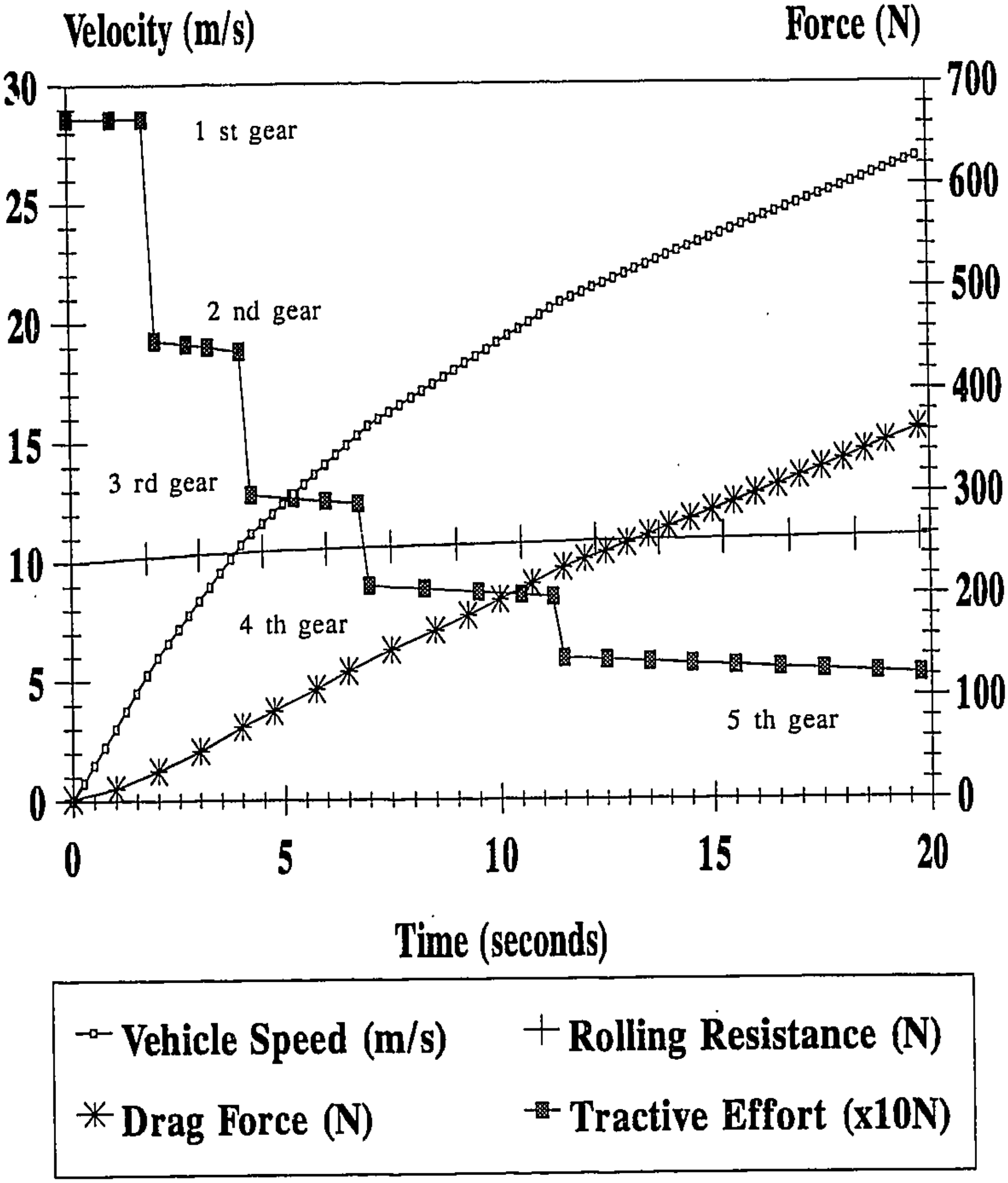

Fig. 4.14 System Response - 5 Speed Transaxle Solectria BRLS16 Electric Drive System

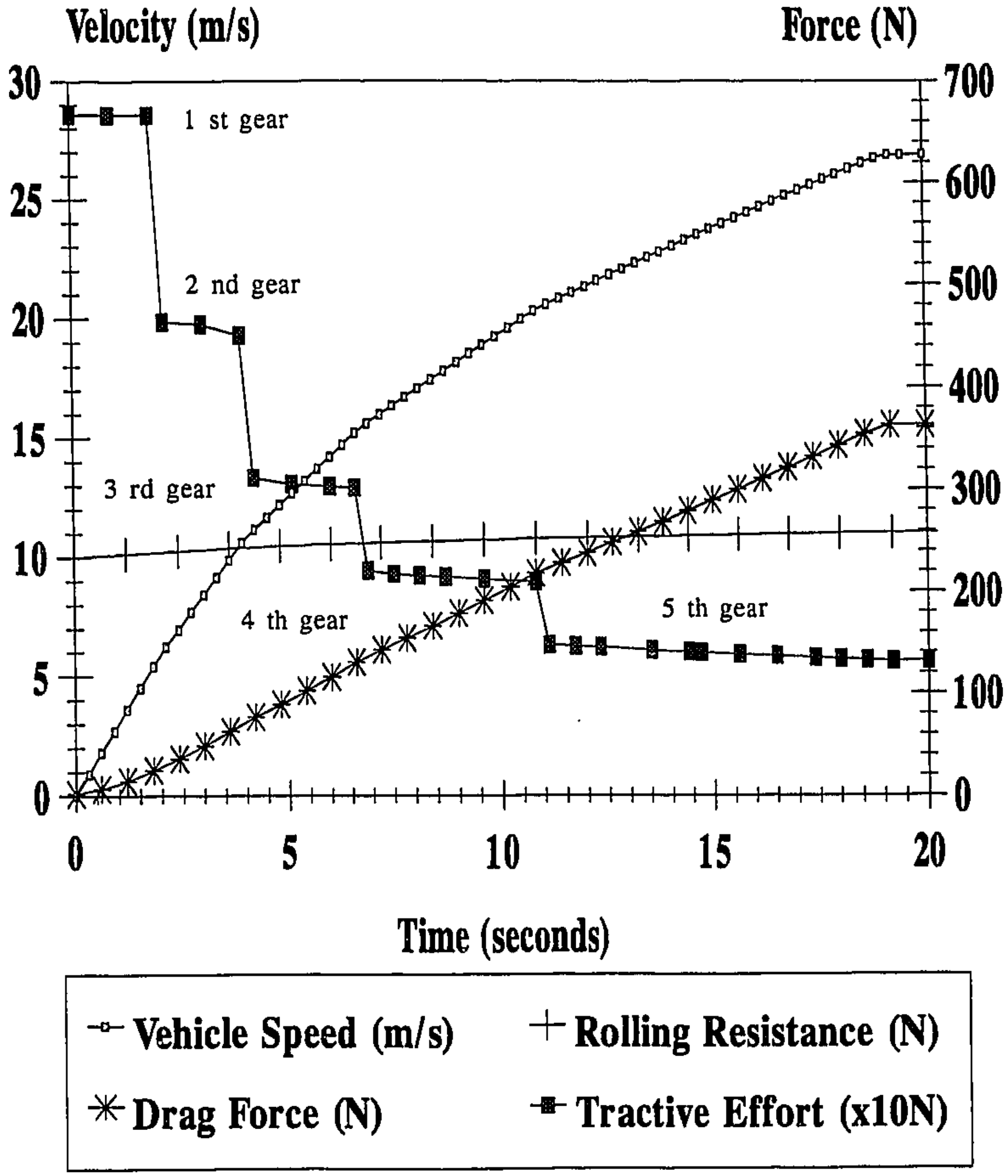

Fig. 4.15 System Response - 5 Speed Transaxle Advanced DC 203-06-4001 Electric Drive System

Table 4.8 Summary of the 5 speed Drive System Simulation Results

Electric Motor	(0-20.1 m/s) Acceleration Time (s)	Tm Motor Torque (N·m)	ω_m (rad/s)	η_c	Power Consumption (kW)
UNIQ SR180LC	12.65	20	503.4	0.92	10.94
UNIQ SR218L	7.54	20	503.4	0.93	10.83
2-Solectria BRLS16	10.89	21.1	477.2	0.92	10.94
Advanced DC 203-06-4001	10.65	24.3	413.2	0.84	11.97

The acceleration performance requirement was met by all the drive systems, when the five speed transaxle design configuration was used. In order to make the most cost effective decision, cost to power ratios were calculated for all the electric drive systems. The electric motor and controller cost, and peak obtainable motor power, were used to obtain the following cost to power ratios:

- UNIQ SR180LC - 333 $/kW,
- UNIQ SR218L - 444 $/kW,
- 2-Solectria BRLS16 - 326 $/kW, and
- Advanced DC 203-06-4001 - 53 $/kW.

In terms of power consumption and response time, the most effective system was the UNIQ SR218L, with a five speed transaxle. However, it had a high cost to power ratio. The next most effective system was the Solectria BRLS16 five speed design configuration. Although the Advanced DC drive system had the most attractive power to cost ratio, it failed to meet the overall efficiency requirements outlined in Section 4. This investigation demonstrated that in order to develop a HEV which has comparable driving performance with today's vehicles, a high expenditure would be required.

In order to minimize this expenditure, an alternative design configuration was analyzed. This included the use of the five speed transaxle, a Solectria motor, and an Advanced DC motor. The Advanced DC motor would be used only as an acceleration helper, while the Solectria would be used at all times in the electric mode of operation. The cost to power ratio of this system was 216 $/kW, capable of providing a combined total peak power of 56 kW. The TUTSIM block diagram for the five speed design configuration was modified in order to represent both electric motors. Each electric motor would receive independent potentiometer control signals, as is outlined in Fig. 4.16. Similar input parameters were used to perform this simulation.

The time response to accelerate a HEV which incorporated a Solectria and an Advanced DC electric motor with a five speed transaxle, was 10.4 seconds (See Fig. 4.17). Since, under steady-state conditions the Solectria electric motor would only be active, it would provide the entire torque to maintain the vehicle at a constant speed of 20.1 m/s. By providing the entire load, the Solectria motor achieved an electrical efficiency of 93.5 %. The corresponding power consumption of this system was calculated to be 10.76 kW. This design configuration provided a very effective compromise between performance and cost, therefore, it was selected as the drive system for the developed HEV in question.

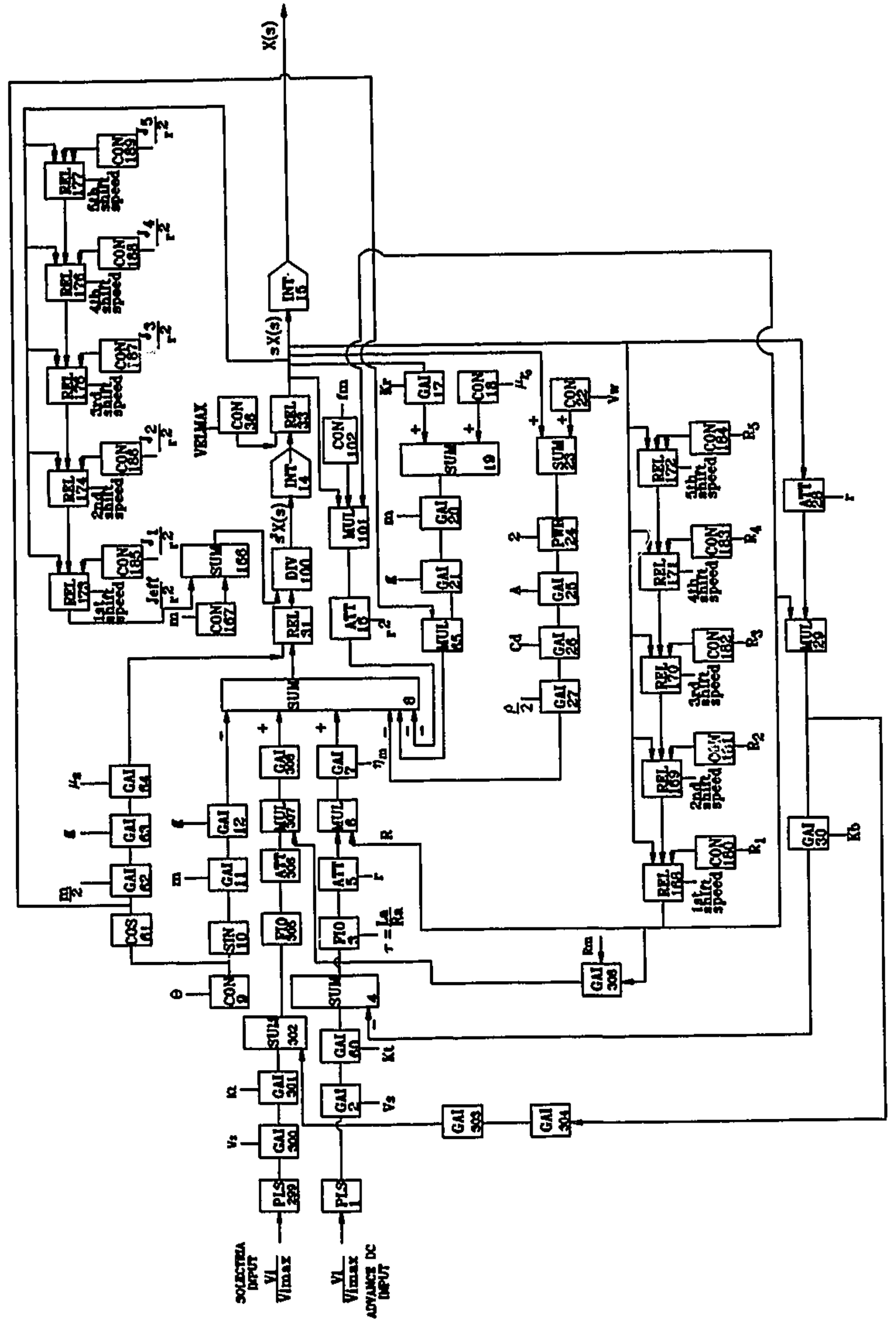

Fig. 4.16 TUTSIM Block Diagram Advanced DC and Solectria Five Speed System

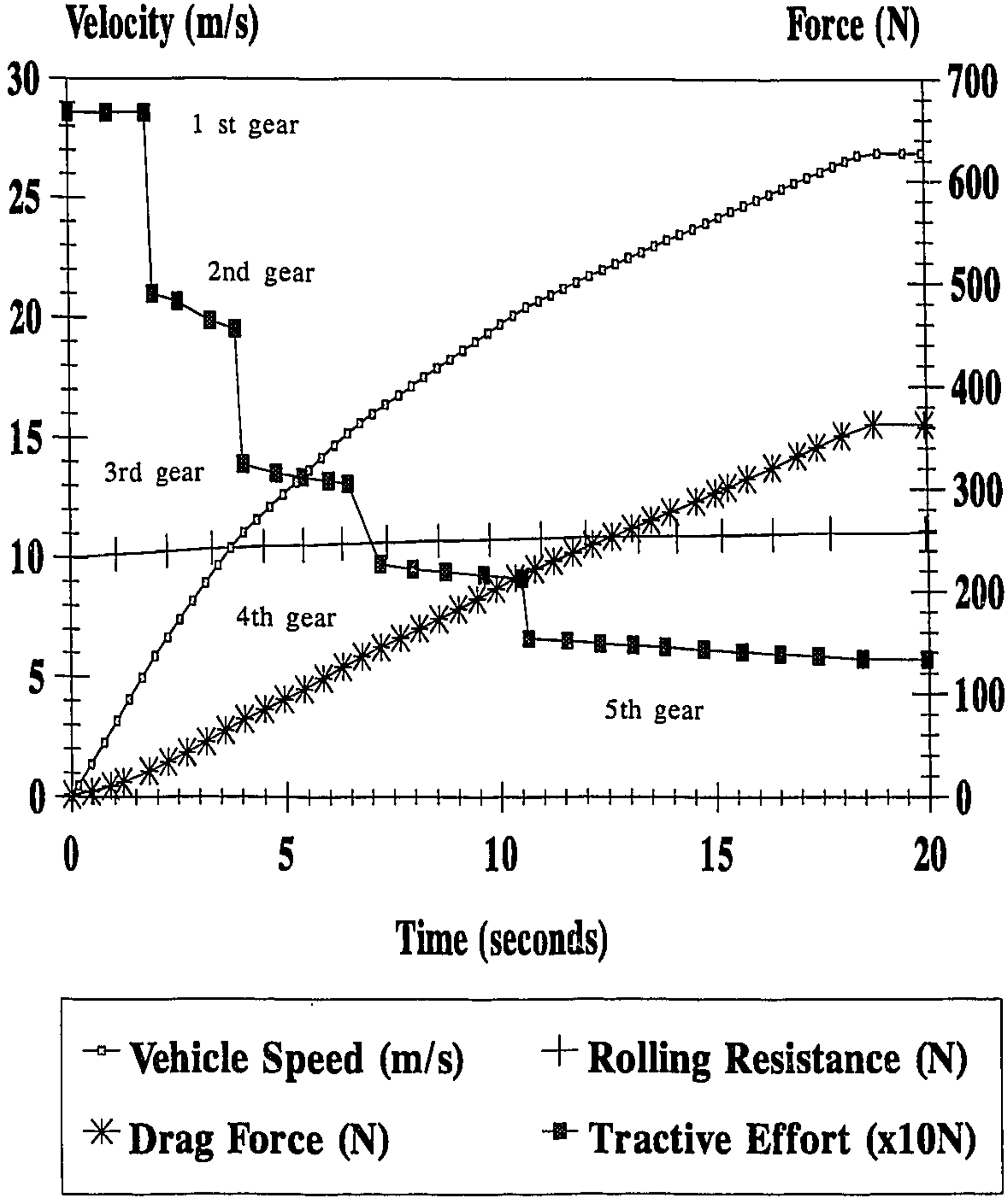

Fig. 4.17 System Response - 5 Speed Transaxle Solectria and Advanced DC Drive System

A strong attribute of the selected electric drive system is that the Solectria will always be activated in EV mode of operation and will therefore provide regenerative braking to the HEV. This feature is not available for the Advanced DC electric motor.

In chapter 7, an alternative simulation will be developed using a high level computer programming language which will be used in conjunction with multi-objective optimization technique in order to optimize the selected electric drive system. The alternative simulation is required, since the multi-run features of the TUTSIM simulation package are not very effective when one desires to perform a multi-objective optimization with various design constraints.

4.3 Summary

As demonstrated, the design of an electric drive system for a hybrid electric vehicle involves a compromise between cost, acceleration and overall electric drive efficiency. Using the outlined mathematical model in the Laplace domain and the developed TUTSIM simulations, these performance characteristics were estimated for four different drive systems with a fixed gear ratio and a 5 speed transaxle configuration. It was found that by incorporating a five speed transaxle to the electric drive system the acceleration and overall efficiency improved in comparison to a fixed gear configuration. Consequently, taking advantage of the fact that vehicles require excess power for acceleration conditions, a low cost high powered Advanced DC series wound motor combined with a Solectria brushless

PM motor was found, through the simulations, to be the most effective compromise for the proposed performance criteria.

5. HEV DESIGN AND CONTROL STRATEGY OVERVIEW

An overview of the mechanical design and control strategy developed for the Concordia HEV will be discussed under three main topics, namely HEV Design Configuration, Auxiliary Power Unit (APU) and Control Strategy. The latter Chapters of this research will complement this outlined design configuration with the aid of multi-objective optimization techniques.

5.1 HEV Design Configuration

As outlined in the literature review, HEVs are designed in either parallel or series configurations. The main advantage of a series configuration is that the auxiliary power unit is operating under a fixed speed and load environment, making it very easy to control from an exhaust gas emissions' point of view. This is mainly due to the absence of the transient environment, which is inherent by the series configuration. However, such a configuration has a low overall efficiency due to the additional mechanical to electrical conversion. The typical overall efficiency of a series HEV is outlined below:

$$\eta_{so} = \eta_a \eta_e \eta_m = 0.82 \tag{5.1}$$

where:

η_{so} - series configuration overall efficiency
η_a - alternator efficiency (0.96)
η_e - electric motor and controller efficiency (0.93)
η_m - drivetrain efficiency (0.92)

On the other hand, a parallel configured HEV is capable of obtaining up to 92 %

overall efficiency, since the available drive of the APU is coupled directly to the transaxle. The main disadvantage of such a configuration is that the auxiliary power unit operates in transient conditions.

The design configuration developed for the Concordia HEV was very unique, for it incorporated both a parallel and a series design configuration. During city driving, the HEV can operate in series mode achieving very low exhaust gas emissions. Whereas, during highway driving the vehicle can operate in parallel mode enabling it to obtain a very high overall efficiency. This control scheme was realized through the use of an analog controller. The general block diagram of this design configuration is illustrated in Fig. 5.1.

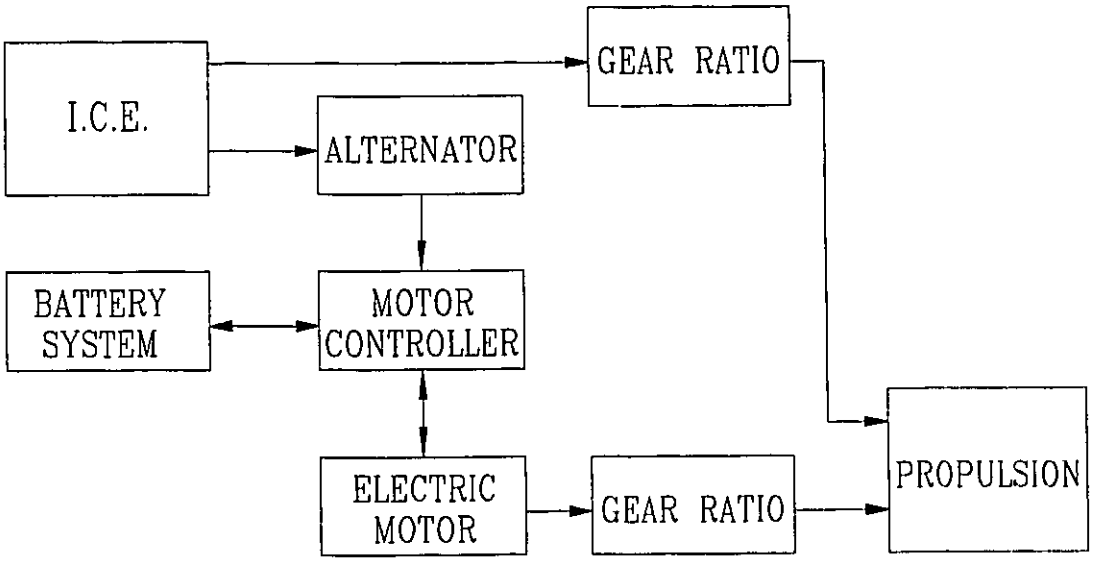

Fig. 5.1 Concordia HEV Parallel-Series Design Configuration

5.1.1 Hybrid Electric Vehicle Design Lay-Out

A 1992 Ford Escort Wagon was converted to a HEV with commercially available off the shelf components that were modified for the application at hand. The main design objectives for this vehicle were safety, low conversion cost, and performance.

Safety was essential, for this vehicle would have to be designed to withstand rigorous qualifying tests, in order to be granted an official entrance in the 1993 Ford Hybrid Electric Vehicle Challenge. A Low conversion cost was also a very crucial design criterion, for the competition emphasized high performance at a minimal conversion cost. It was for this reason that the electric drive system required an extensive scientific investigation prior to making a selection. The final main design objective was performance which was established for all modes of operation in terms of overall efficiency, vehicle acceleration and range. With such high design standards extensive research had to be performed in order to develop a state-of-the-art hybrid electric vehicle.

The general component location was outlined during the early stages of the development work. This established design constraint such as weight and volume, which served as a basis for selecting and integrating the components into the vehicle. The energy storage system was located in the rear of the vehicle, while the two electric motors, were coupled to the existing transaxle through a chain drive concept. Fig. 5.2 provides an overview of the design configuration developed for the HEV, outlining all the major components.

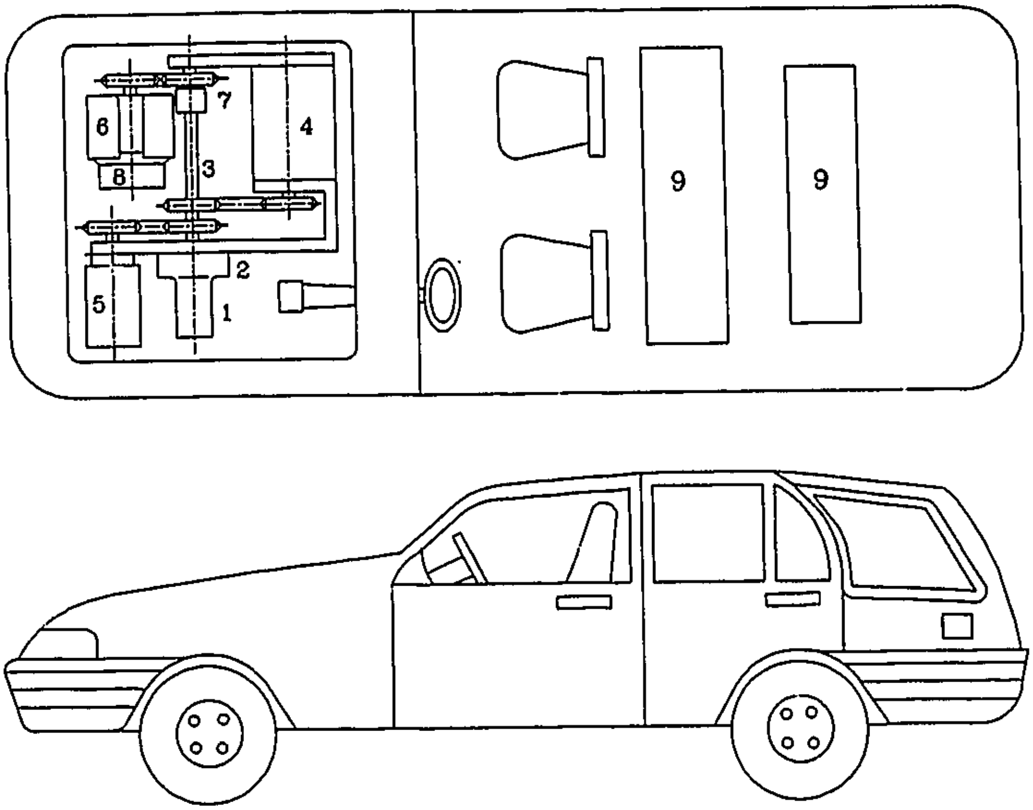

1. Five Speed Transaxle
2. Clutch and Flywheel Assembly
3. Drive Shaft
4. Advanced DC Electric Motor
5. Solectria Electric Motor
6. Internal Combustion Engine ICE
7. Electro-Magnetic Clutch
8. Alternator Unit
9. Battery Enclosures

Fig. 5.2 Concordia HEV Design Lay-out

To ensure the HEV's stability, a weight distribution analysis was performed using basic moment equations and a computer program. Using anticipated component weights and location, an effective method for analyzing the weight distribution was established in the early development stages of the vehicle. The general equations used to obtain the weight distribution on each of the four tires are as follows:

$$WLFT = \frac{W\cdot(l-z)(w-y)}{l\cdot w} \tag{5.2}$$

$$WRFT = \frac{W\cdot(l-z)\cdot y}{l\cdot w} \tag{5.3}$$

$$WLRT = \frac{W\cdot(w-y)\cdot z}{l\cdot w} \tag{5.4}$$

$$WRRT = \frac{W\cdot(y\cdot z)}{l\cdot w} \tag{5.5}$$

where:

WLFT - Weight Left Front Tire
WRFT - Weight Right Front Tire
WLRT - Weight Left Rear Tire
WRRT - Weight Right Rear Tire
l - Wheelbase
w - Tract width

The y and z variables represent the distance between the component's center of gravity and the left front tire, which was used as a reference. Fig. 5.3 outlines the general model used to perform the weight distribution analysis.

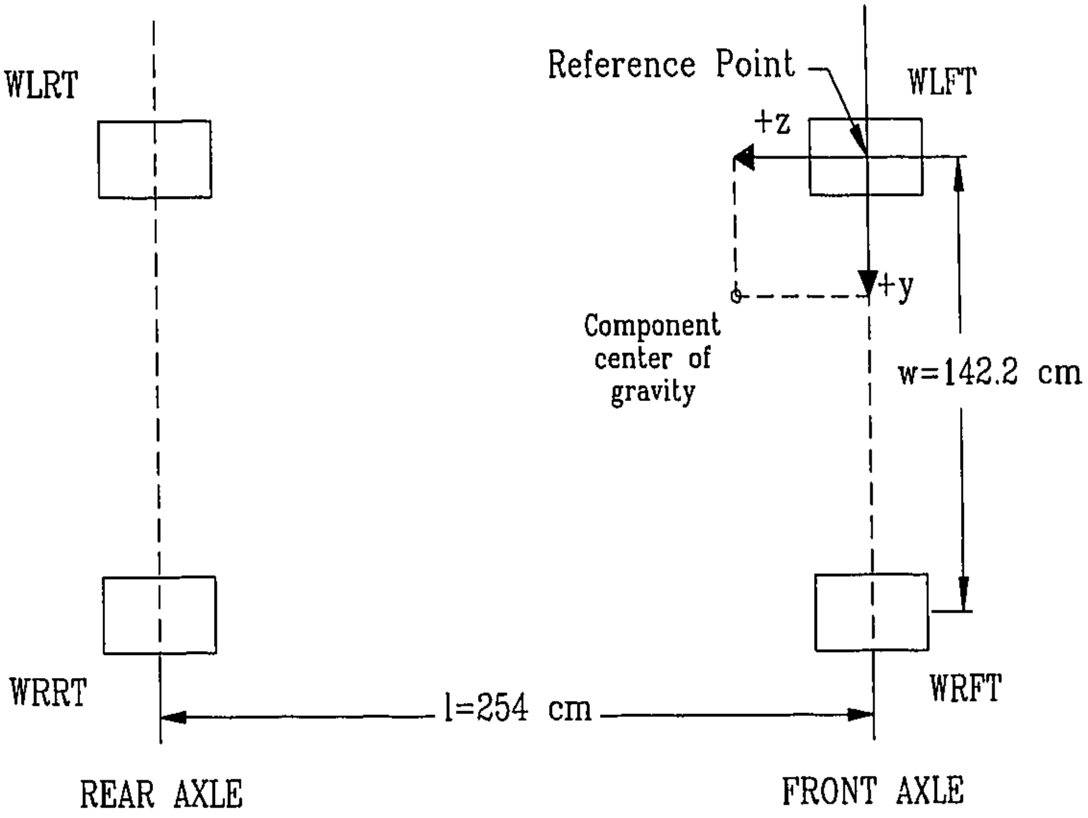

Fig. 5.3 Schematic of Weight Distribution Model

In order to get a breakdown of the HEV weight, the initial unladen vehicle weight of the Ford Escort Station Wagon (1050 kg), 59/41 % front-to-rear bias, and 52/48 % left-to-right bias were used as a starting point. Table 5.1 outlines the maximum weight allocated for each component and the distance from the reference point.

Table 5.1 Weight Distribution - Projected Component Location and Weight

Components Added to the HEV			
Item	Weight (kg)	Distance z (cm)	Distance y (cm)
1. Front battery	248	185.4	76.2
2. Rear battery tray	177	274.3	76.2
3. Cargo ballast	20	276.9	76.2
4. Roll bar	20	185.4	76.2
5. Passenger	80	96.5	104.1
6. Driver	80	96.5	48.3
7. Solectria motor	29	-20.3	33
8. Solectria controller	7	-43.2	33
9. Advanced DC motor	49	-5.1	96.5
10. Curtis controller	5	20.32	99.1
11. APU and support structure	50	-45.7	96.5
12. Alternator	10	-45.7	78.7
13. 5 US gallons gasoline	13.8	193	76.2
Components Removed			
14. Ford Escort engine & cooling system	-143	0	96.5
15. 14 US gallons gasoline	-38.74	193	76.2
Weight increase of vehicle	607.1		
Base Escort weight	1050		
Total anticipated HEV weight	1657.1		

The anticipated vehicle weight of the Concordia HEV was slightly below 1737 kg which represents the gross vehicle weight (GVW). This GVW was deemed by the competition organizers to be the maximum allowable weight that the vehicle could handle. Since, it was not surpassed, the vehicle's structural integrity and handling were not compromised from the point of view of overall loading. From these projected values, the front/rear weight bias of the HEV was calculated to be 47.3/52.7 %, while the left/right distribution was 50.9/49.1%. This approach was used throughout the development stages of the vehicle. It served as a useful tool in designing a well distributed hybrid electric vehicle.

5.1.2 Power Plant Design Integration

All the three power plants (Solectria electric motor, Advanced DC electric motor, and the auxiliary power unit) had to be capable of transferring propulsion to the front wheels through the transaxle. An extension shaft was designed and coupled to the existing (Ford Escort) flywheel and dry clutch assembly. Two spherical roller bearings were used to support this shaft. A cover plate fastened on to the transaxle housing supported one of these bearings, while a support plate retained the other bearing. Four high strength studs were used to retain the support plate and the cover plate. A metal collar was designed to retain the driven sprockets of the electric drive system. This collar was, thereafter, supported by the extension shaft which was designed to transmit the torque from the electric motors through the transaxle and on to the wheels. Fig. 5.4 illustrates the general transaxle modifications performed in order to implement the electric drive system.

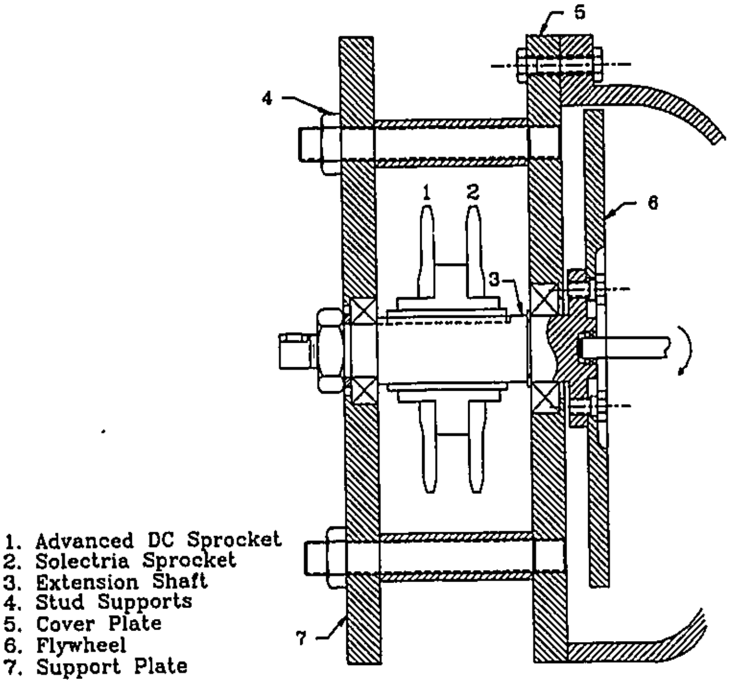

Fig. 5.4 Shaft Extension for the Electric Drive System [22]

In order to design a reliable shaft capable of obtaining infinite life, stress analysis was used to complement the design process. The general model used to perform this analysis is outlined in Fig. 5.5. In this analysis, a 3 to 1 sprocket ratio was assumed for both electric motors. This 3 to 1 ratio represented the upper design constraint which was used in the multi-objective optimization in Chapter 7; therefore it ensured a reliable design since in represented the worst loading condition. A safety factor of 3.5 was incorporated in the design equation to take into account any external loads, such as vibrations which were not included in the stress analysis model. The analysis was performed using the Distortion Energy Theorem to obtain the mean stress, along with a calculated alternating stress component. Thereafter, the Soderberg equation was used to calculate the shaft diameter that would obtain infinite life. Based on the result of the analysis, a 40 mm shaft diameter was manufactured from SAE 1006 steel. The complete stress analysis is included in Appendix 3.

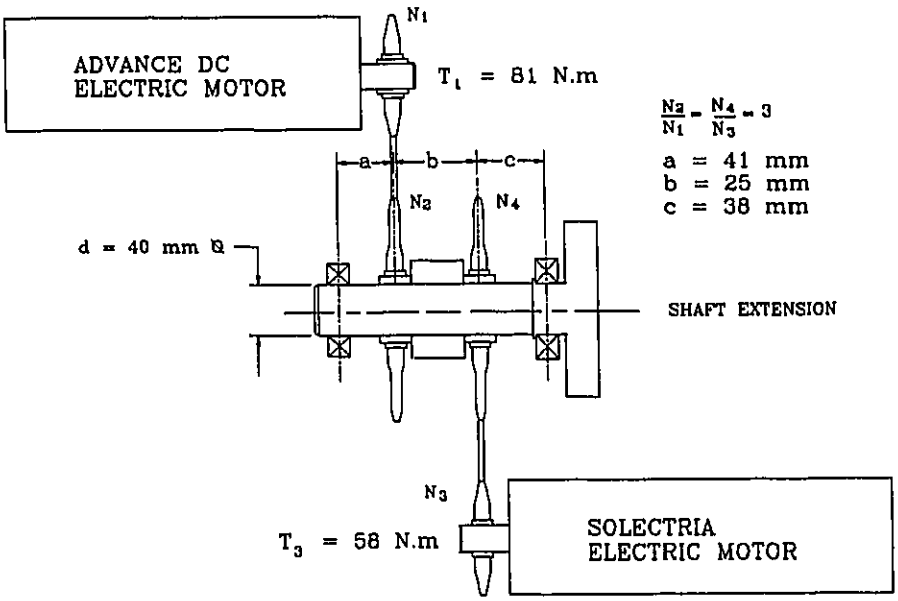

Fig. 5.5 Schematic of Stress Analysis Model

Another important factor in this design was to assure that the three power plants would have a common motion with respect to the chassis. This was accomplished by modifying and incorporating standard engine mounts to the frame fastening all three power plants. A structural platform was designed to support the rear of the Advanced DC electric motor and the entire auxiliary power unit. Two engine mounts were thereafter used to support this structural platform on to the chassis. The cover plate supported the front of the Solectria and Advanced DC electric motors, while the rear of the Solectria motor was supported by a modified engine mount. These aspects of the design are illustrated in Fig. 5.6.

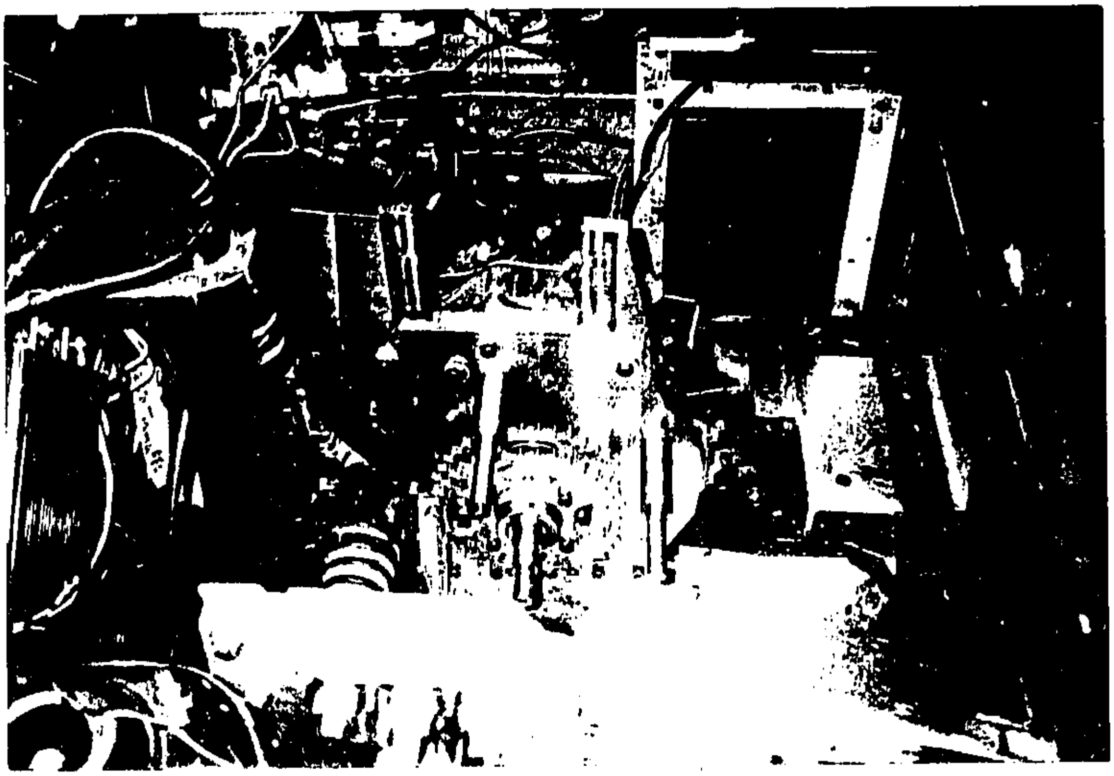

a) Illustration of Support Structure Cover Plate and Shaft Extension

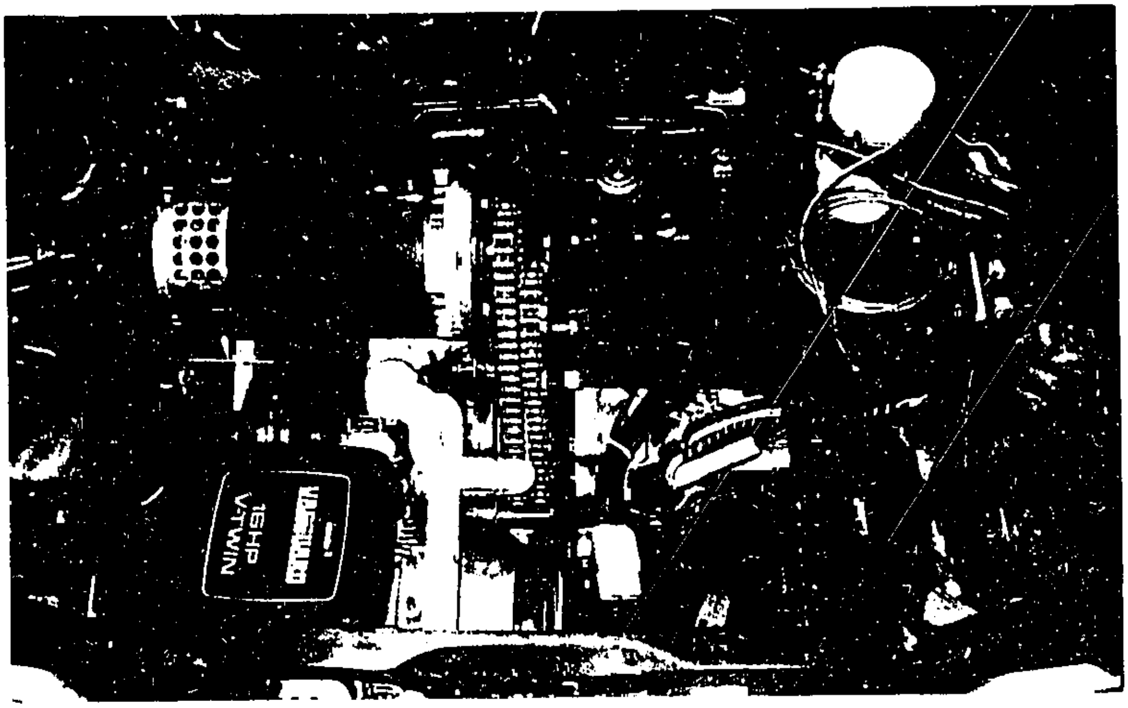

b) Illustration of the Three Power Plants

Fig. 5.6 Support Structure of the Power Plants

5.2 Auxiliary Power Unit

The auxiliary power unit (APU) was selected based on the following criteria: specific fuel consumption, peak power, and physical dimensions. Since, the APU would be modified to run in either a series or a parallel configuration, the largest power requirements of the two configurations was used to size the unit. The engine had to maintain the vehicle at a maximum speed of 64 km/h in series mode of operation, while in parallel mode of operation the target speed was 72 km/h. By using the overall efficiency outlined in equation 5.1 and the resistive forces (equations 4.6 and 4.7), the power required to maintain the vehicle at a constant speed of 64 km/h (on a flat surface) during series mode of operation was calculated as follows:

$$P_{APUS} = \frac{V_{HEV} \cdot (F_a + F_{ro})}{\eta_{so}} = 8.2\ kW \qquad (5.6)$$

The overall efficiency for the parallel configuration ($\eta_{po} = 0.92$) and similar resistive force equations were used to calculate the power required to maintain the vehicle at a constant speed of 72 km/h (on a flat surface):

$$P_{APUP} = \frac{V_{HEV} \cdot (F_a + F_{ro})}{\eta_{po}} = 10.2\ kW \qquad (5.7)$$

The resistive forces were calculated based on the vehicle model outlined in Chapter 4. The power requirements of the parallel mode of operation took precedence in the sizing of the auxiliary power unit. A gasoline powered Briggs and Stratton (B&S) 12 kW Vanguard engine was selected as the APU for the Concordia HEV, based on its peak power capabilities, specific fuel consumption, and overall physical dimensions (40 cm x 44 cm x 31 cm). The specific fuel consumption of the Vanguard engine at 10.2 kW was calculated to be 0.246 g/kWh. Fig. 5.7 outlines the performance characteristics of the B&S engine.

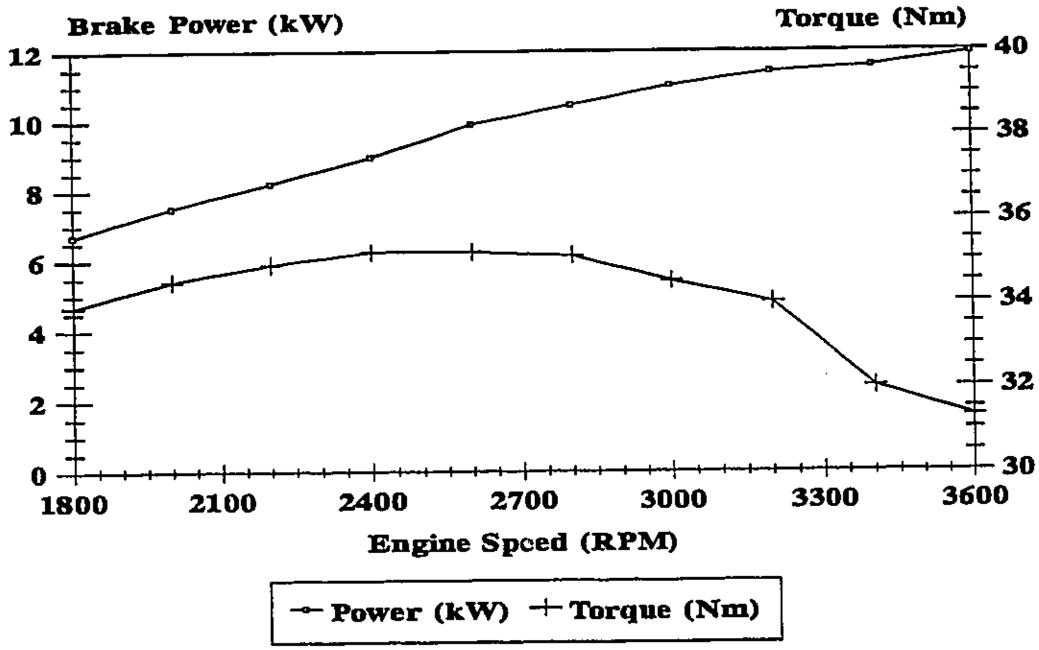

Fig. 5.7 B&S Vanguard 12 kW Engine Performance Characteristic [26]

5.2.1 Series Design Configuration

A high powered alternator was custom designed by Fisher Electric Motor Technology Incorporated (FEMTI) for the Concordia HEV. The alternator was installed directly on the shaft of the B&S engine. Since the alternator was a custom design, important specifications had to be outlined to FEMTI, namely: 9 kW net power output, 25.4 cm maximum outer diameter, 11 cm maximum thickness, operating speed of 2700 rpm, and operating voltage of 170 V.

An important aspect in specifying the alternator's design, is to properly match the engine performance with the alternator's requirements. This may sound as a trial task, however it is often overlooked. During the 1993 HEV Challenge many competitors had undersized their internal combustion engine and were not capable of obtaining their alternators designed performance.

At the specified operating speed (2700 rpm) the B&S engine is capable of providing 10 kW of peak power, which is adequate to achieve 9 kW of net power from the alternator (See Fig. 5.7). This is mainly possible, due to the fact that the alternator operates at 96 % efficiency. The alternator's high efficiency and low power to weight ratio of 0.9 kW/kg was obtained by using a neodymium permanent magnet rotor. Fig. 5.8 illustrates the overall dimensions of the alternator as well as the rotor and stator assembly.

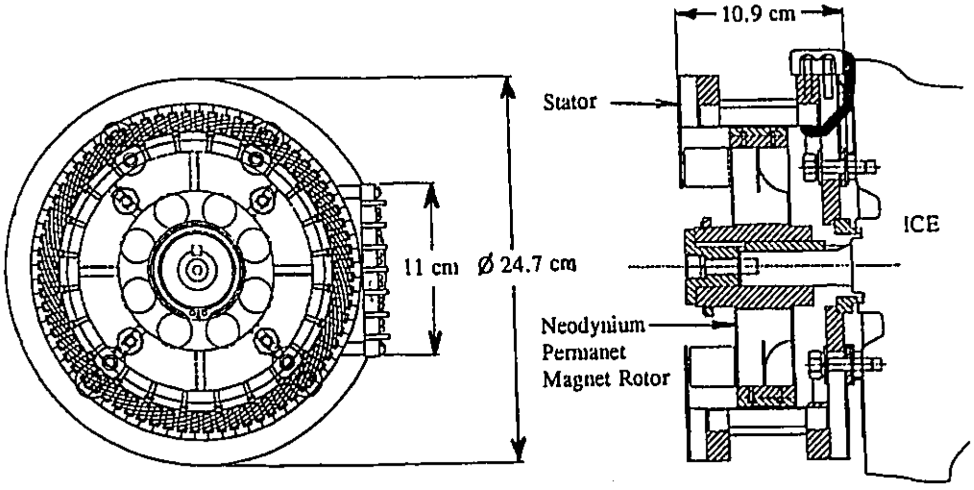

Fig. 5.8 Schematic of the Fisher 9 kW Alternator [27]

When the alternator was tested, it produced a maximum power and voltage of 8.5 kW and 180 Volts, respectively. A further discussion on these test results will be presented in Chapter 8, and used to perform a multi-objective optimization.

The three phase power output of the alternator had to be converted to DC current in order to be stored by the battery system or used by the electric motors. Using high powered diodes, a three phase rectifier bridge was developed. In-line fuses on each of the phases were implemented into the circuit and served as a means of protection for the alternator. Thereafter, three in-line 25 A, 240 V mechanical relays were used to effectively load or unload the alternator, depending on whether or not the series mode of operation was active. A schematic of this configuration is shown in Fig. 5.9.

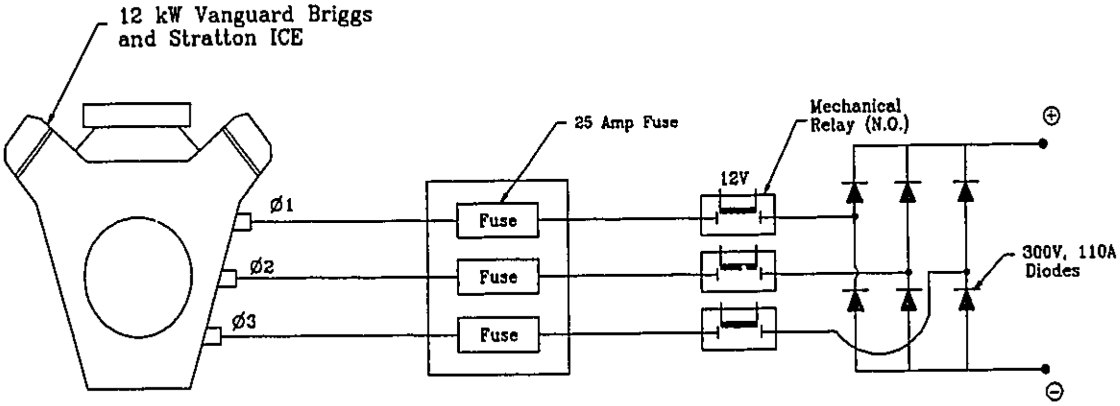

Fig. 5.9 Schematic of the Three Phase Rectifier Bridge [22]

5.2.2 Parallel Design Configuration

The parallel design configuration consisted of an electro-magnetic clutch and an additional shaft, which was connected to the electric drive shaft extension. Fig.

5.10 represents this configuration.

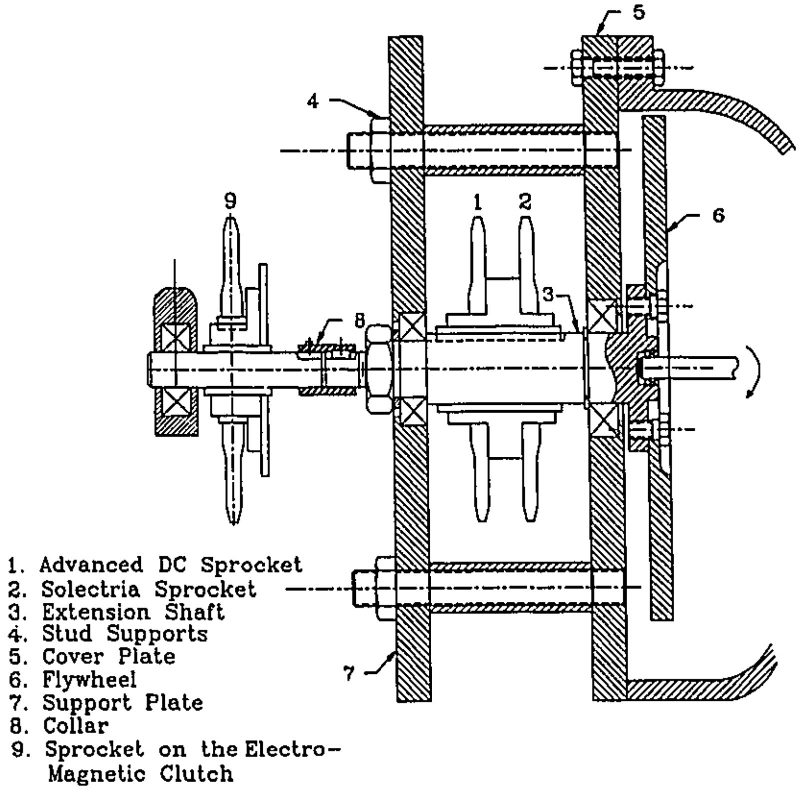

Fig. 5.10 Parallel Design Configuration Overview [22]

In parallel mode, the APU transmits torque directly to the stock transmission through a chain and sprocket linkage. The engine is effectively loaded by activating the electro-magnetic clutch, which permits propulsion to the front wheels of the HEV. The driver can select this mode of operation when the desired speed is reached, by a simple switch located in the driver's compartment. This functions similar to a cruise control unit found in many of today's vehicles. When this mode is not selected, the clutch is disengaged and the engine can run independently of the transmission in series mode, or can be turned off.

In order to integrate the sprocket on to the engine, a collar was designed to fasten on the crankshaft of the engine. This assembly can be seen on the left side of Fig. 5.11, along with the high powered alternator visible on the right side. By establishing this assembly, the chain drive design required to transmit the engines torque on to the transaxle, for the parallel mode of operation was completed.

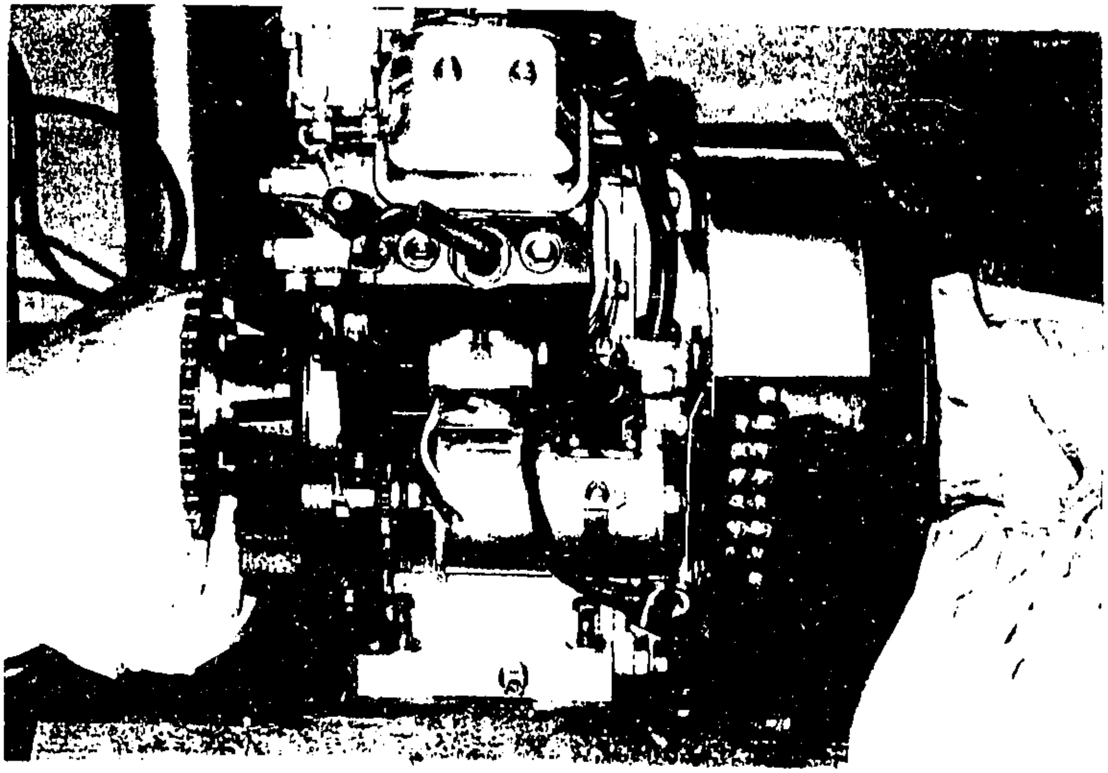

Fig. 5.11 Illustration of the Collar Assembly and Alternator on the B&S Engine

5.2.3 Fuel Delivery System and Emission Control Strategy

A simple, low cost and practical fuel delivery and emission control strategy was implemented in the Concordia HEV. The B&S Vanguard ICE was united with the following fuel delivery systems:

- a stock Ford Escort Wagon fuel tank,
- an in line fuel pump, and
- a downdraught carburettor unit.

The high pressure stock fuel pump (hpf-pump) was replaced with an in-line solenoid activated fuel pump for the following reasons. This hpf-pump required a manifold which would enable fuel to enter the carburettor as well as return back into the fuel tank. In terms of the current being drawn, the hpf-pump has a continuous 3 A demand, whereas the solenoid activated pump requires a nominal current of 0.1 A. The substantial current demand difference between these two pumps, precluded the use of the hpf-pump.

The emission control strategy relies on a single bed three-way catalyst and on the optimal tuning of the carburettor unit. The catalyst volume of 347.4 cm^3 was sized for the 480 cm^3 ICE, having the following composition: 1243.1 g/m^3 Pt, 0.0 g/m^3 Pd, and 261.4 g/m^3 Rh.

To ensure that the catalyst reaches its optimal operating temperature of 400 °C, the exhaust system was wrapped with fibreglass insulation starting from the tuned exhaust headers to the catalytic converter. The catalyst was placed at 56.5 cm from the ICE exhaust ports. This effectively limits the power lost due to back pressure and also minimizes any catalyst deterioration. Fig. 5.12 illustrates the fuel delivery and exhaust system implemented on the Concordia HEV.

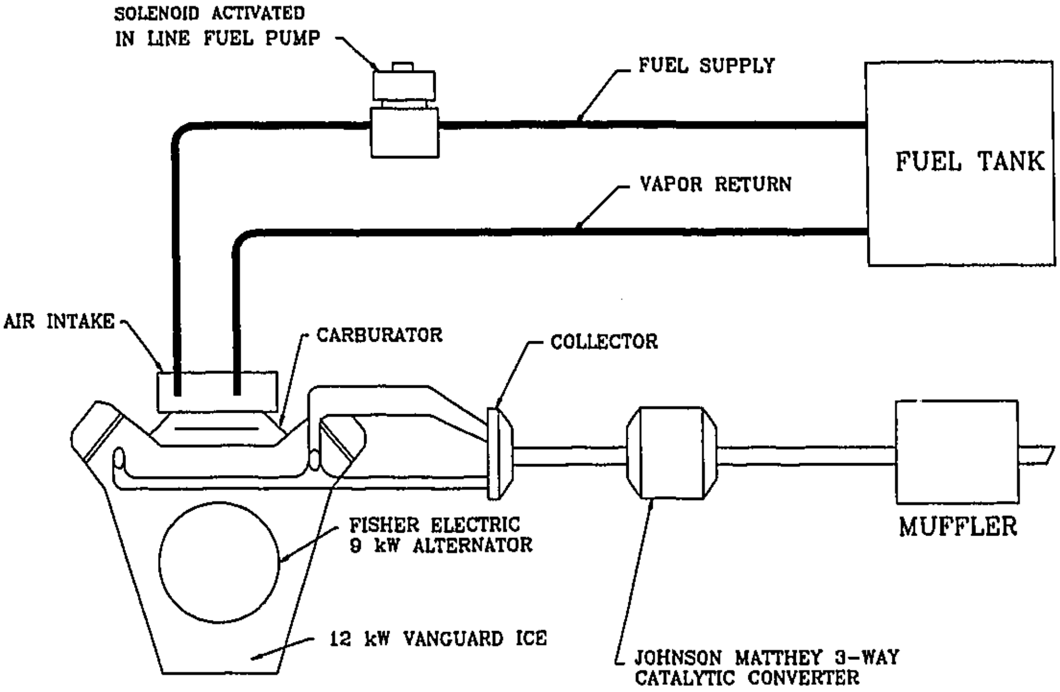

Fig. 5.12 Schematic Concordia HEV Fuel Delivery System [22]

Even the most efficient carburettor fuel delivery system is not capable of maintaining the stoichiometric air-fuel ratio when exposed to varying speed and load conditions. To lessen this detrimental parameter and to obtain an effective emission control scheme, the speed of the ICE was set at a fixed point via the mechanical governor for both the series and parallel modes of operation. The actual speed and tuning of the engine was determined by incorporating multi-objective optimization with experimental test results such as, emission, power and fuel consumption testing. This will be discussed in more detail in Chapter 8.

5.3 HEV Control Strategy

The HEV control strategy was developed by incorporating two motor controller units and an analog circuit board which enabled the driver to select the various HEV modes of operations.

5.3.1 Overview of the Motor Controller Units

Speed control for the Advanced DC and the Solectria BRLS16 motors was provided by the 1221B-74 Curtis Controller and BRLS240H Solectria Controller, respectively. The switching pulses required to control the motors in a pulse width modulation (PWM) control strategy was accomplished through the use of Metal Oxide Semiconductors Field Effect Transistors (MOSFETs). The two electric motor controllers will be briefly described below.

Curtis Controller

The Curtis controller was selected as the control unit for the Advanced DC motor, for it used an efficient PWM control strategy, operating at 15 kHz frequency. The supply voltage capabilities of the control were 72-120 Volts, matching the Advanced DC motor requirements. In terms of continuous constant current loading, the controller had the following time limitations:

- 2 minutes at a constant load of 400 amps,
- 5 minutes at a constant load of 250 amps,

- 60 minutes at a constant load of 150 amps, and
- continuous operation at constant load of 50 amp.

These limitations are graphically represented in Fig. 5.13.

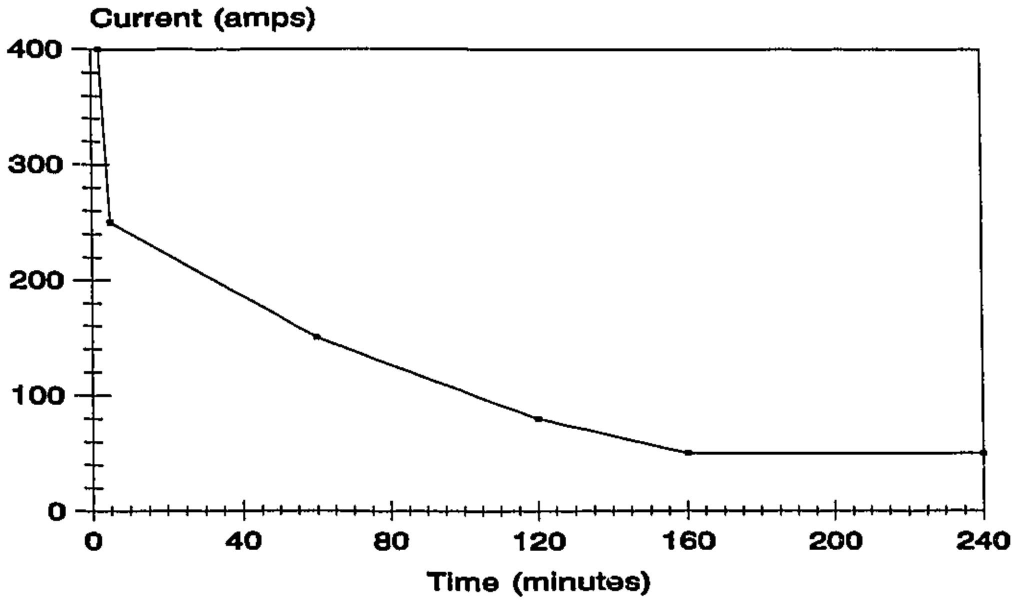

Fig. 5.13 Curtis Controller - Current Rating Versus Time

The MOSFETs, which are responsible for switching the current from the battery system to the Advanced DC motor, are the main components of the power section. When they are in the "off" mode, a parallel bank of fast recovery rectifiers (termed freewheel diodes in the block diagram) provide current to the motor. Suppression of voltage spikes and battery ripples is obtained by connecting an array of capacitors across the positive and negative battery terminals, B+ and B-, respectively. The logic and power block diagram of the Curtis controller is outlined in Fig. 5.14 [28].

The logic and auxiliary circuitry operates at a regulated voltage of 14 volts. Since, the Advanced DC motor is only used under acceleration, the key switch and interlock input (KSI) was placed on the stick shift of the 5-speed manual transmission. This enables the driver to effectively power up or power down the control circuitry, which is in direct communication with the Advanced DC motor. A quarter turn, 0 to 5 kΩ rotary potentiometer is used to provide the speed control input to the acceleration circuit. A trim potentiometer provides a means of adjusting the ramp signal, which controls the acceleration rate. As a safety measure, a limit integrator reduces the controller output in response to undervoltage, overvoltage or overcurrent.

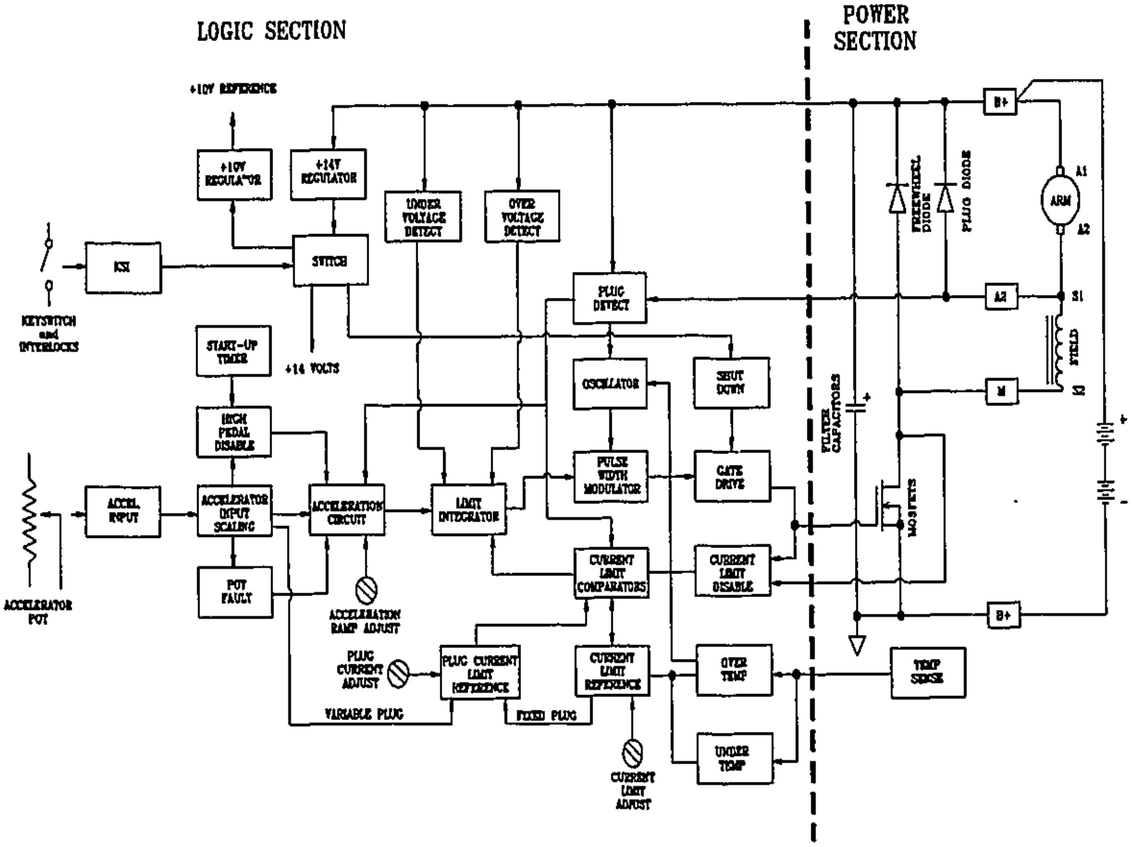

Fig. 5.14 Biock Diagram of the Curtis 1221B-74 Controller [28]

The undervoltage detector provides an output to the limit integrator, which in turn reduces the output voltage of the controller and enables the batteries to recover and establish an equilibrium. An overvoltage detector produces an output when the battery voltage is too high, providing a protection to the controller from excessive voltage transients [28].

Current sensing is obtained by monitoring the voltage drop across the main power MOSFET switch. A current limit comparator compares the current across the MOSFET and the reference current limit of 400 amps. If the reference current is exceeded an overcurrent signal act on the limit integrator, which in return reduces the controller output to the reference current.

The main component of the logic circuitry is the pulse width modulator, which is used to compare the input signal with a 15 kHz sawtooth wave produced by the oscillator. The resulting pulsed output, which is sent to the MOSFET drive circuit, is varied between full "off" and full "on". This provides the high pulse current required to power the MOSFETs "on" and "off". The duty cycle is varied in accordance to the accelerator input signal.

Solectria Controller

The task of selecting the controller for the Solectria BRLS16 electric motor was less difficult than that of the Advanced DC electric motor, for Solectria produces custom made controllers for their electric motors. Therefore, only a brief controller review was performed for the Solectria BRLS240H controller, which was specifically manufactured to control the speed and torque of the permanent magnet BRLS16 electric motor. The variable frequency current control of the motor was limited at 240 A. In terms of continuous constant current loading, the controller had the following current limitations:

- 4 minutes at a constant current of 200 amps,
- 60 minutes at a constant current of 150 amps, and
- continuous operation at a constant load of 100 amps.

The sequential switching of the permanent magnet motor's three phases is performed by low resistance MOSFETs, capable of switching at up to 20 kHz. The controller also has a built in regenerative braking circuit, which is activated by a 0 to 5 kΩ potentiometer that is placed on the brake pedal. Through testing, this feature of the controller was found to be very beneficial, in terms of energy recuperation during city driving conditions. These tests were performed by outlining a 2.1 km city route and thereafter driving the vehicle through this route, with and without regenerative braking.

In order to obtain valid data, several tests were performed at both of these modes of operation. A Cruising Equipment Corporation data acquisition system, kilowatt-hour meter and a lap-top computer were used to perform these tests. The specifications of the data acquisition unit are presented in Appendix 2.

After analyzing the obtained data, an average energy recuperation of 12.5 % was obtained by using regenerative braking, thus proving the importance of this feature. Fig. 5.15 illustrates the cumulative energy dissipated versus time obtained during one of the tests without regenerative braking. The total energy dissipated during this test was 0.57 kWh.

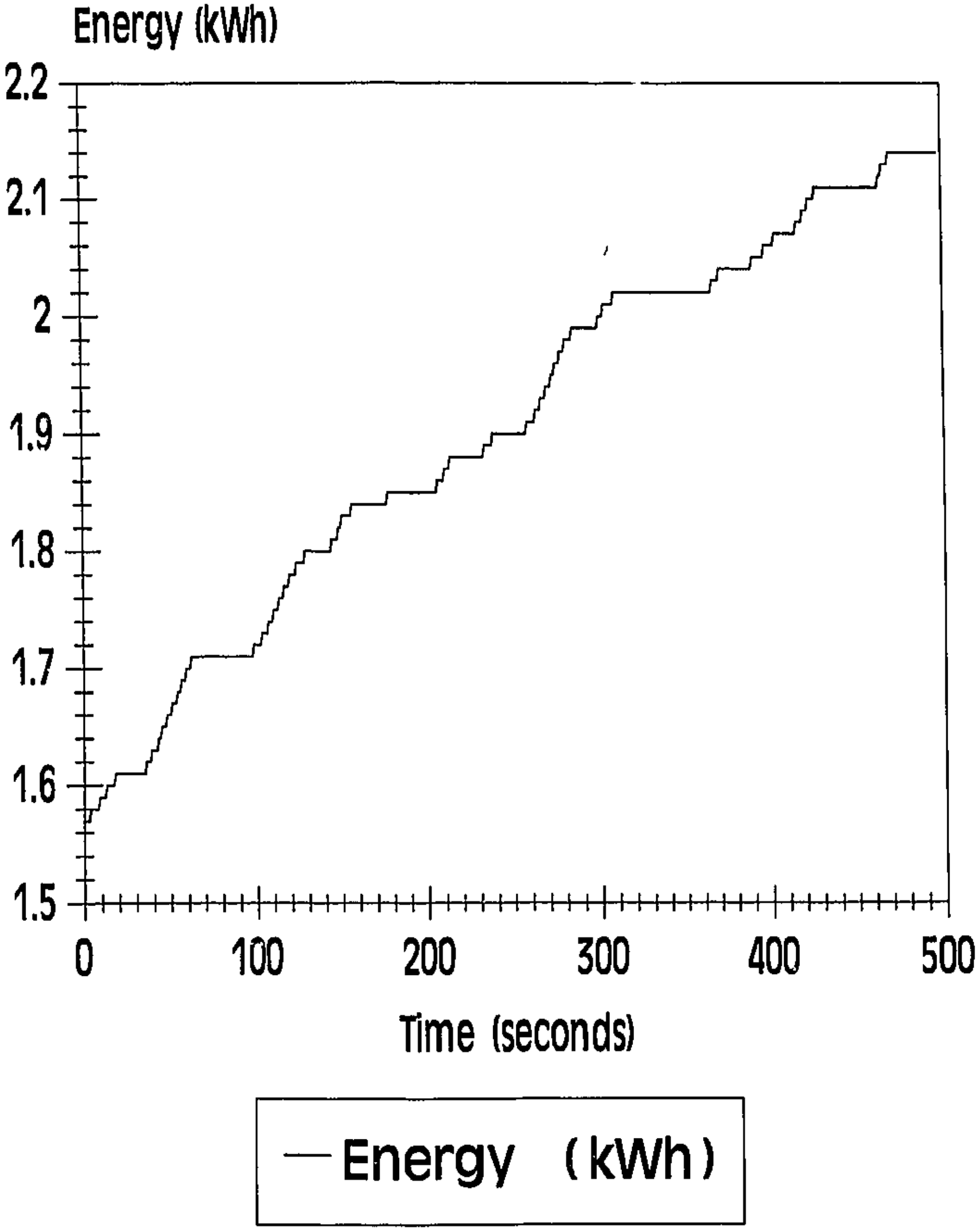

Fig. 5.15 Cumulative Energy Dissipated Versus Time - No Regenerative Braking

Fig. 5.16 represents the current and voltage effects versus time for the same test as outlined in Fig. 5.15. It can be clearly seen that no negative current was measured, therefore no energy recuperation occurred during this drive cycle.

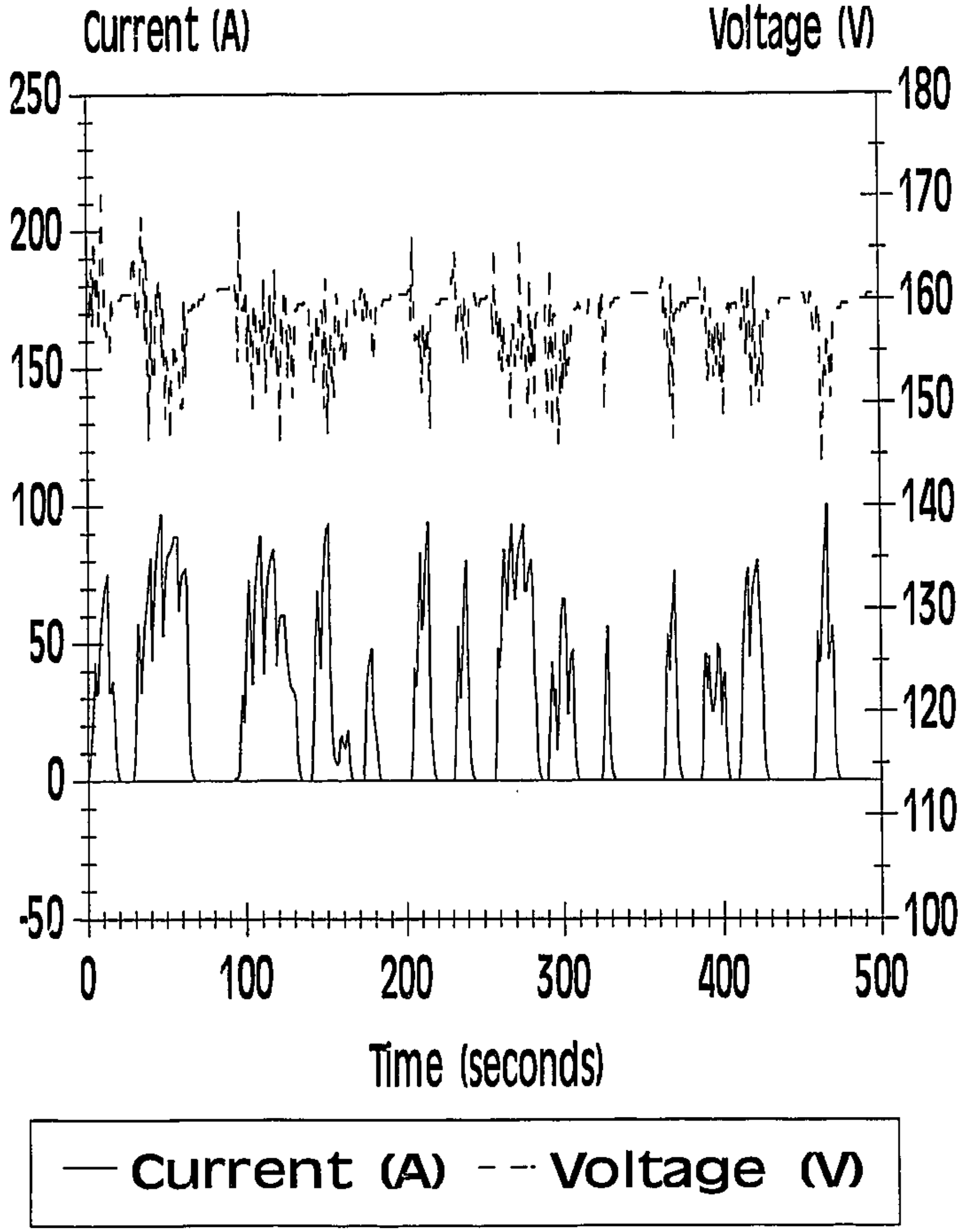

Fig. 5.16 Current & Voltage Versus Time - No Regenerative Braking

Fig. 5.17 illustrates the cumulative energy dissipated versus time obtained during one of the tests with regenerative braking. The total energy dissipated during this test was 0.46 kWh.

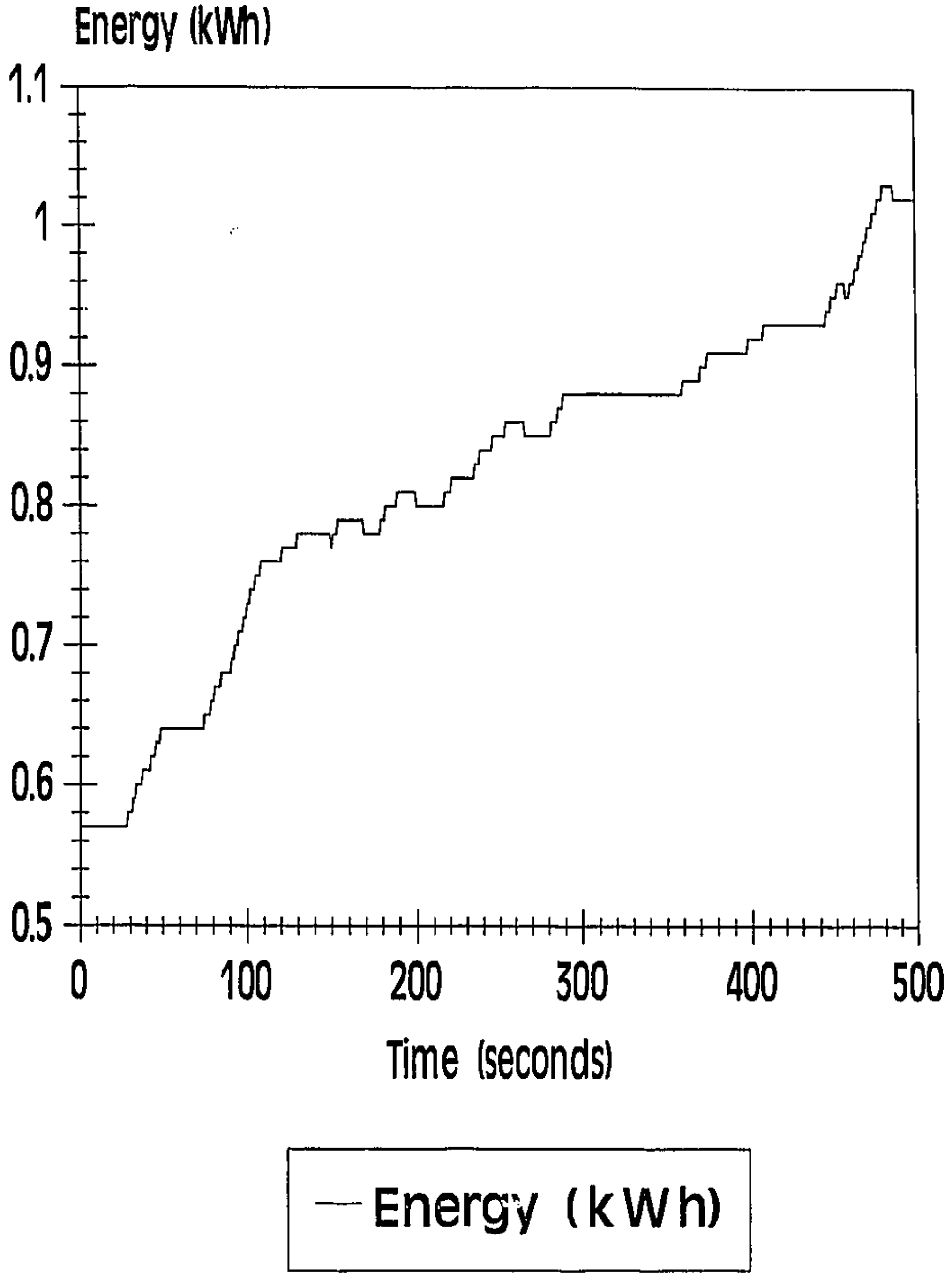

Fig. 5.17 Cumulative Energy Dissipated Versus Time - Regenerative Braking

The current and voltage versus time data acquisition results for this test are shown in Fig. 5.18. The negative current pulses represent the current being recuperated by the energy storage system. In terms of magnitude, negative pulses of up to 34 A were measured for this particular drive cycle.

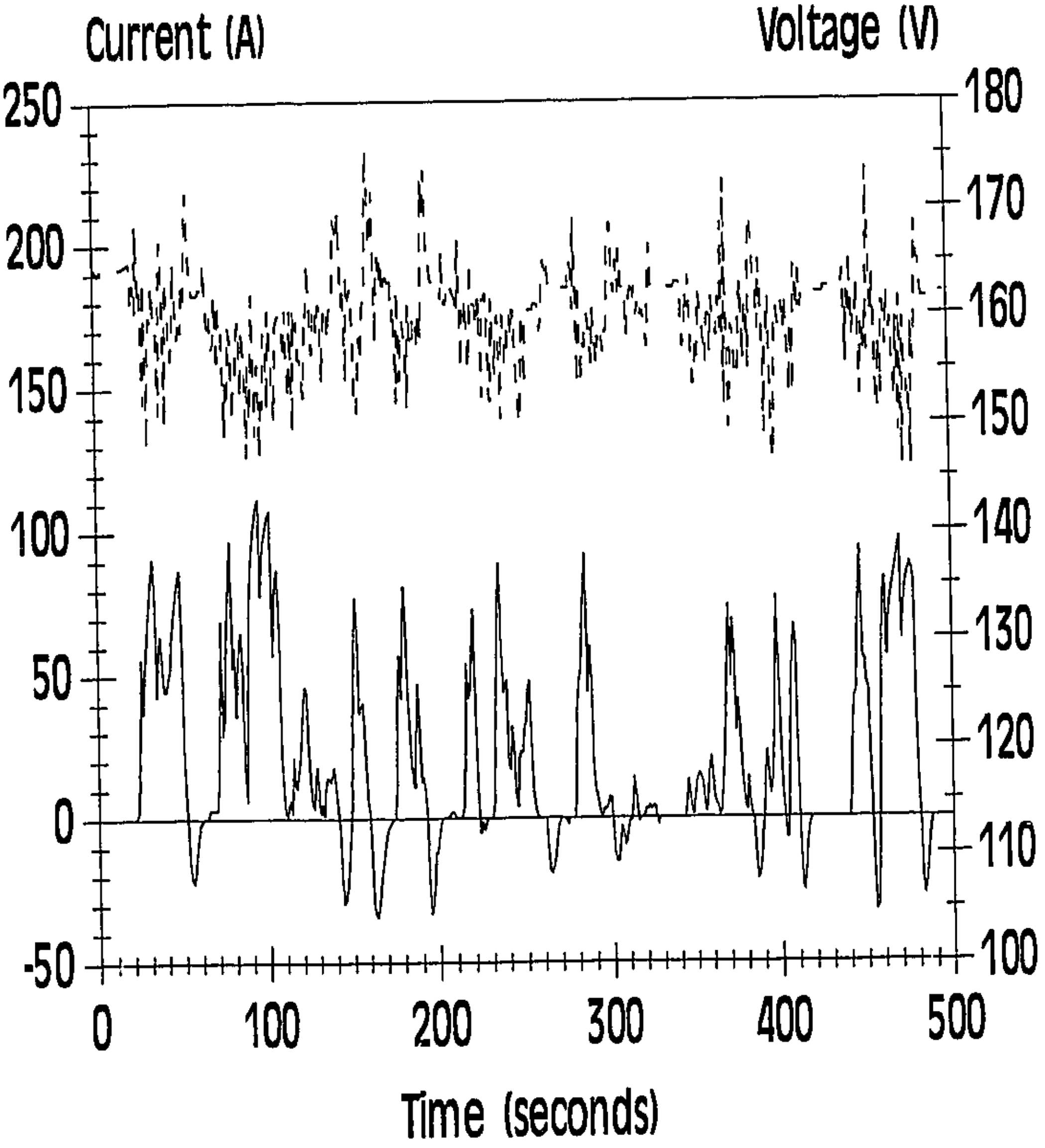

Fig. 5.18 Current & Voltage Versus Time - Regenerative Braking

5.3.2 Selection of the Power Conductors

The power conductors of the HEV were sized in accordance to the National Electrical Code. All Conductors of the electric drive system were completely isolated from the vehicle chassis, and the 12 volt system was used for the vehicle instrumentation. High voltage conductors were selected with a 600 volt insulating rating, which corresponds to three and half times the peak ground reference voltage of 173 volts. The power conductors were sized by the following equation and Table 5.2:

$$CMA = \frac{I_{max} \cdot LF \cdot K \cdot n}{AVD} \tag{5.8}$$

where:

I_{max}: Maximum current in the conductor
LF: Conductor loop length (m)
K: Copper constant
AVD: Allowable voltage drop for ultimate drain (amps)
CMA: Cir Mils Area
n: Safety factor

Table 5.2 American Wire Gauge Conductor Selection [29]

AWG SIZE	CIR MILS AREA	AWG SIZE	CIR MILS AREA
18	1 820	4	41 740
16	2 680	3	52 820
14	4 110	2	66 360
12	6 630	1	83 690
10	10 380	I/0	106 600
8	16 610	I/00	133 100
6	26 240	I/000	187 800

Since, the Solectria and Advanced DC controllers operate at different voltages, the conductors for these two systems were individually sized. However, a common high power ground was utilized and sized by summing the maximum operating current of both controllers. Table 5.3 summarizes the coefficient used to calculate the CMA value of the conductors along with the American Wire Gauge (AWG) size selection.

Table 5.3 Power Conductor Selection

Conductor	I_{max} (A)	LF (m)	K	n	AVD	CMA	AWG Size
Hi-Voltage Ground	640	8.7	36.1	1.25	3	83 752	I/0
Solectria Motor & Controller	240	8.1	36.1	1.25	3	29 241	4
Advanced DC Motor & Controller	400	8.7	36.1	1.25	3	52 345	3
Fisher Alternator	70	8.5	36.1	1.25	3	8 950	10

The location of the power conductors, high voltage areas, and fuses are outlined in Figure 5.19. Single element non-time delay fuses are required for this type of application. In the advent of a short circuit, the fuses used as a protective measure, were capable of melting within a time of two to three milliseconds, in order to prevent any damage to the MOSFETs of the controllers. The fuses used on the HEV were sized 1.25 times higher than the maximum current limit of the controllers. In-line fuses of 300 amps and 500 amps were incorporated with the

Solectria and Curtis conductors, respectively. This over sizing enabled the electric system to function in transient surge current environment, acquired under hard acceleration, while still providing fast response to overcurrents.

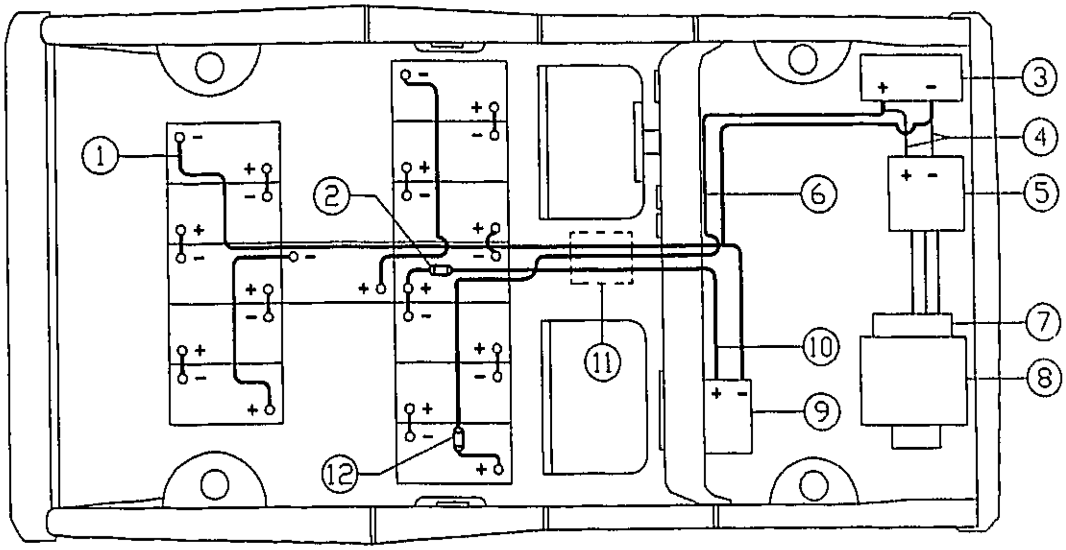

1. High Voltage Ground AWG I/0
2. 500 A Non-Time Delay Fuse
3. Solectria BRLS240H Controller
4. Rectifier Bridge Output AWG 10
5. Rectifier Bridge
6. Solectria Controller Conductor AWG 4
7. Fisher Alternator
8. Briggs and Stratton Engine
9. Curtis 1221B-74 Controller
10. Curtis Controller Conductor AWG 4
11. Manual Battery - System Disconnect
12. 300 A Non-Time Delay Fuse

Fig. 5.19 Schematic Concordia HEV - Location of the Power Conductors

5.3.3 Modes of Operation

An analog circuit board was developed and used to control the three modes of operation which are identified as Electric, Series and Parallel. At any given time, only one of these modes can be activated, by simply selecting the appropriate toggle switches located on the dash board of the Concordia HEV. Fig. 5.20 outlines the toggle switches used to control the different modes of operation.

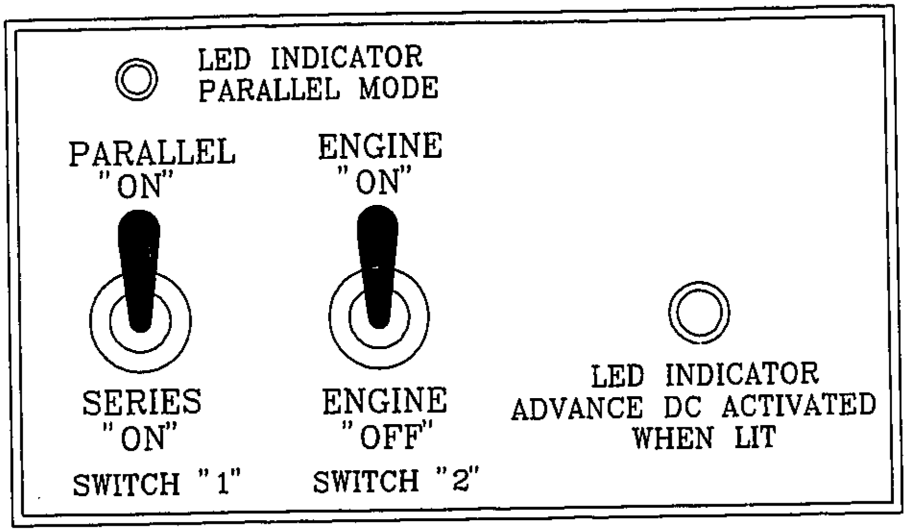

Fig. 5.20 Modes of Operation Control Panel [22]

The electric mode of operation is always active when the ignition key is turned "on", whether or not the HEV is in the Series or Parallel mode. Therefore, the electric motors can be used to complement the propulsion of the internal combustion engine in parallel mode of operation, or in series mode of operation, they provide the entire vehicular propulsion.

To start the electric mode of operation switch "1" must be placed in the downwards position and the ignition switch must be turn to the "on" position. If the driver turns the ignition switch completely (as in an ordinary vehicle) the ICE will start only if switch "2" is in the upper position marked as engine "on" and switch "1" is in the series position. If this is set, the vehicle is in the series mode of operation, for the mechanical relays are activated and the engine provides its power to the alternator, which is thereafter converted to electrical energy. This energy is either stored in the battery system or is utilized by the electric motors to drive the vehicle.

When the vehicle is in the 4th or 5th gear the driver has the option of activating the parallel mode of operation by simply changing switch "1" to the upper position. By effectively executing this sequence, the internal combustion engine drives the vehicle through the transaxle. The parallel mode of operation can only be activated in 4th or 5th gear because the engine is sized only to maintain the vehicle at constant speeds up to 96 km/h, and is not designed to be used for accelerating the vehicle. When the vehicle is in the parallel mode of operation and encounters a steep slope, the electric motors can assist in overcoming this condition. This operation occurs similar to a cruise control system with the only exception that the driver provides the feedback required to maintain the speed when excessive external vehicle loads are encountered, which the ICE in unable to overcome. As a safety feature, every time the brake pedal is pressed, the electro-magnetic clutch is deactivated therefore disabling the parallel mode of operation.

In all three modes of operation, the driver has the ability of activating the Advanced DC motor by simply pressing a push-button located on the manual shifter. The control panel will indicate that the acceleration helper motor is activated by the use of a LED.

5.4 Summary

The parallel-series design configuration, design lay-out and power plant integration of the Concordia HEV have been discussed. Furthermore the Briggs and Stratton Vanguard Engine was selected as the auxiliary power unit due to its small physical dimensions, adequate peak power, low fuel consumption, and low emissions level. The design of the series mode of operation included a high powered Fisher alternator, which was installed directly on the shaft of the B&S engine, mechanical relays and a rectifier bridge. An electro-magnetic clutch was used to transmit propulsion to the front wheels of the HEV, during parallel mode of operation. Thereafter, a description of the HEV control strategy was presented. Through an experimental investigation, an average energy recuperation of 12.5 % was obtained by using regenerative braking during city driving.

6. ENERGY STORAGE SYSTEM

In this thesis, the energy storage system will be analyzed from a performance point of view for an electric and hybrid electric vehicle environment. This chapter will, therefore, exclude any in depth electro-chemical battery analysis, since it is deemed to be beyond the scope of this study

6.1 Battery Performance Ratings

Battery manufacturers use several methods to rate the performance of batteries. The most commonly used methods are as follows:

- a capacity rating in terms of A·h (Amp-hour), based on a 20, 10, 5, or 3 hour time intervals, and
- reserve minutes capacity measured in minutes.

The capacity rating of batteries is a measure of the total current that a battery can provide over a prespecified time interval. For example, if a battery has a rating of 100 A·h, based on a 20 hour period (C/20), it can provide 5 A for a period of 20 hours. The capital letter "C" followed by a slash and a numerical value, representing time, is used to refer to the hour basis of the capacity rating.

The other method specifies the reserve minutes, which is the amount of time a battery can withstand a constant current of 25 A. For example, if a battery manufacturer specifies 180 reserve minutes for a particular battery, it can provide a 25 A discharge for a period of three hours.

Since there are several methods of rating batteries, it becomes very difficult to correlate and compare different batteries based on the manufacturer's specifications. To achieve a proper comparison of several different battery systems, one must conduct constant current battery tests.

Furthermore, in order to properly assess an EV's or HEV's range and acceleration performance, the energy and power density of a battery system is required. Energy density of a battery system defines the amount of range a vehicle can obtain, while power density dictates the amount of power the battery can provide to the electric drive system during acceleration. In order to establish these two quantitative measurements, extensive constant power battery testing is required.

6.1.1 Constant Current Battery Test Results

In depth constant current tests were performed on several lead-acid batteries, during the course of this research. The batteries selected for testing were first analyzed based on the manufacturer's specifications, namely cycle life, capacity rating and weight. Furthermore, it was important that the battery systems could:

- withstand continuous charging and discharging on a daily basis,
- function under extreme working conditions such as high and low ambient temperatures, and
- withstand vehicle vibrations.

Based on the weight distribution analysis outlined in Chapter 5, the maximum allocated weight for the Concordia HEV energy storage system was established as 425 kg, and the operating voltage of the electric drive system could effectively be set as high as 168 V. Using the maximum allocated voltage and weight of the battery pack, a weight restriction of 30 kg for a 12 V lead-acid module was determined.

A total of five different commercially available lead-acid batteries were selected for constant testing. The weight of each 12 V module was within the maximum battery restriction. This is more precisely outlined in Table 6.1, along with their respective internal grid configuration.

Table 6.1 Specifications - Batteries Selected for Constant Current Testing

Battery Tested	Weight per 12 V Module (kg)	Battery Internal Grid Configuration
Optima 800	18	Spiral-Wound Plate
Chloride 6EF78	26	Tubular Plate
Delco Voyageur 27FMF	24	Flat Plate
Eastern-Penn RV27	24.6	Flat Plate
Eastern-Penn RV31	28.5	Flat Plate

A preliminary calculation revealed that a continuous current draw of 45 A, at a nominal bus voltage of 168 V would be required to supply the electric drive with adequate power to maintain the Concordia HEV at a constant velocity of 64 km/h (on a flat road surface). It was therefore decided to perform 45 A constant current battery tests, in order to obtain a proper comparison among the five batteries.

A simple, yet effective battery test set-up was developed by using a DC to AC inverter, high power rated conductors, an inductive ammeter, and two multimeters. The test batteries were connected in parallel with the DC to AC inverter, and thereafter loaded to 45 A. Since the DC to AC inverter output was 120 Volts 60 Hz, light bulbs were used as resistors, which provided the 45 A load. Throughout each test the current was maintained constant by switching "on" additional resistors, in order to compensate for the increase in resistance brought forth by the heat built up of the initial resistors. Fans provided forced air cooling for the entire set-up. A schematic of the set-up is illustrated in Fig. 6.1.

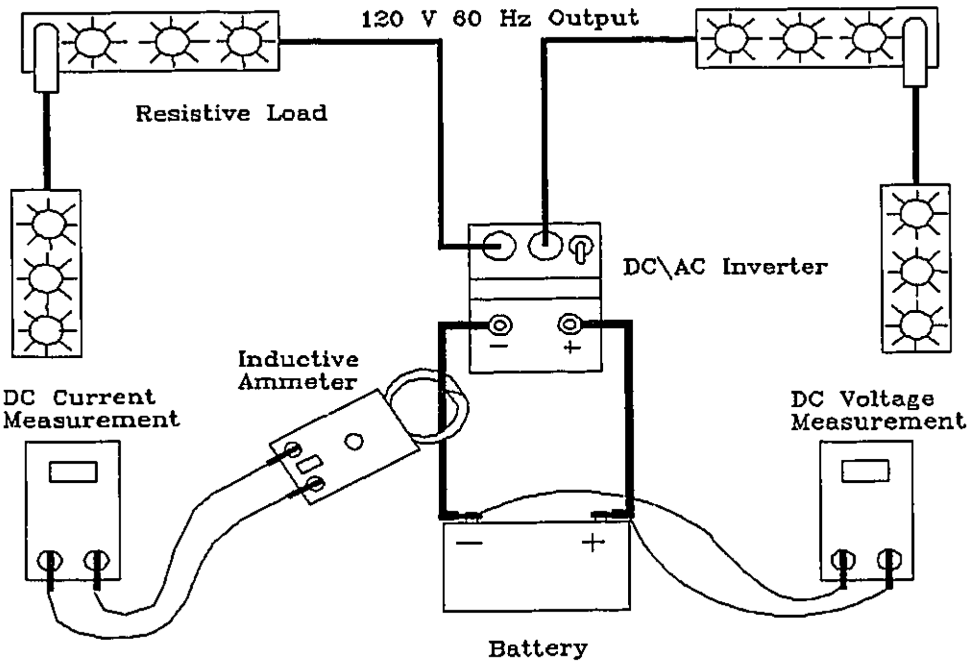

Fig. 6.1 Constant Current Battery Test Set-Up

Although a constant draw of 45 A is not a true representation of an actual vehicle drive cycle, it offers a good indication of the batteries performance when subjected to a high discharge rate. The amount of time each battery withstood at a constant discharge of 45 A, is outlined in Fig. 6.2.

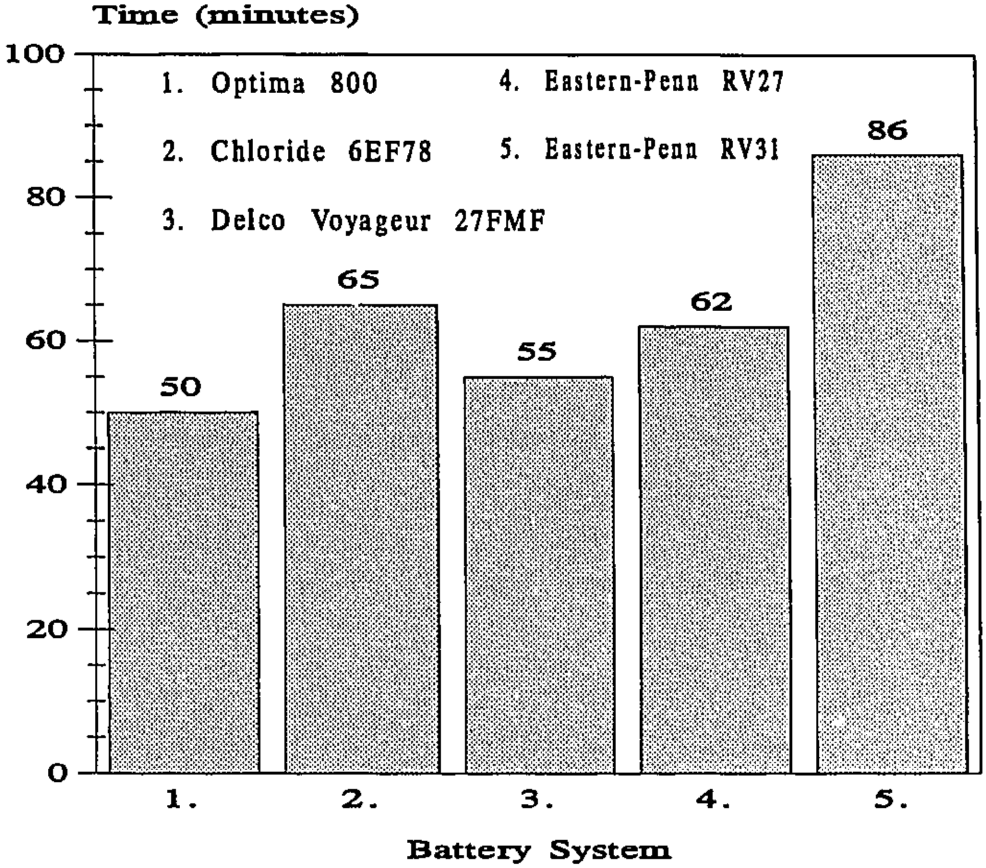

Fig. 6.2 Lead-Acid Batteries - 45A Constant Current Test Results

Although the current was maintained constant during these tests, the voltage of each battery varied substantially. In terms of total energy discharge, the Eastern-Penn RV31 clearly outperformed all the other tested batteries. The total energy dissipated by each battery, during these tests was obtained by integrating the power versus time functions outlined in Fig. 6.3. The total energy provided by each system, along with their respective energy density is tabulated in Table 6.2.

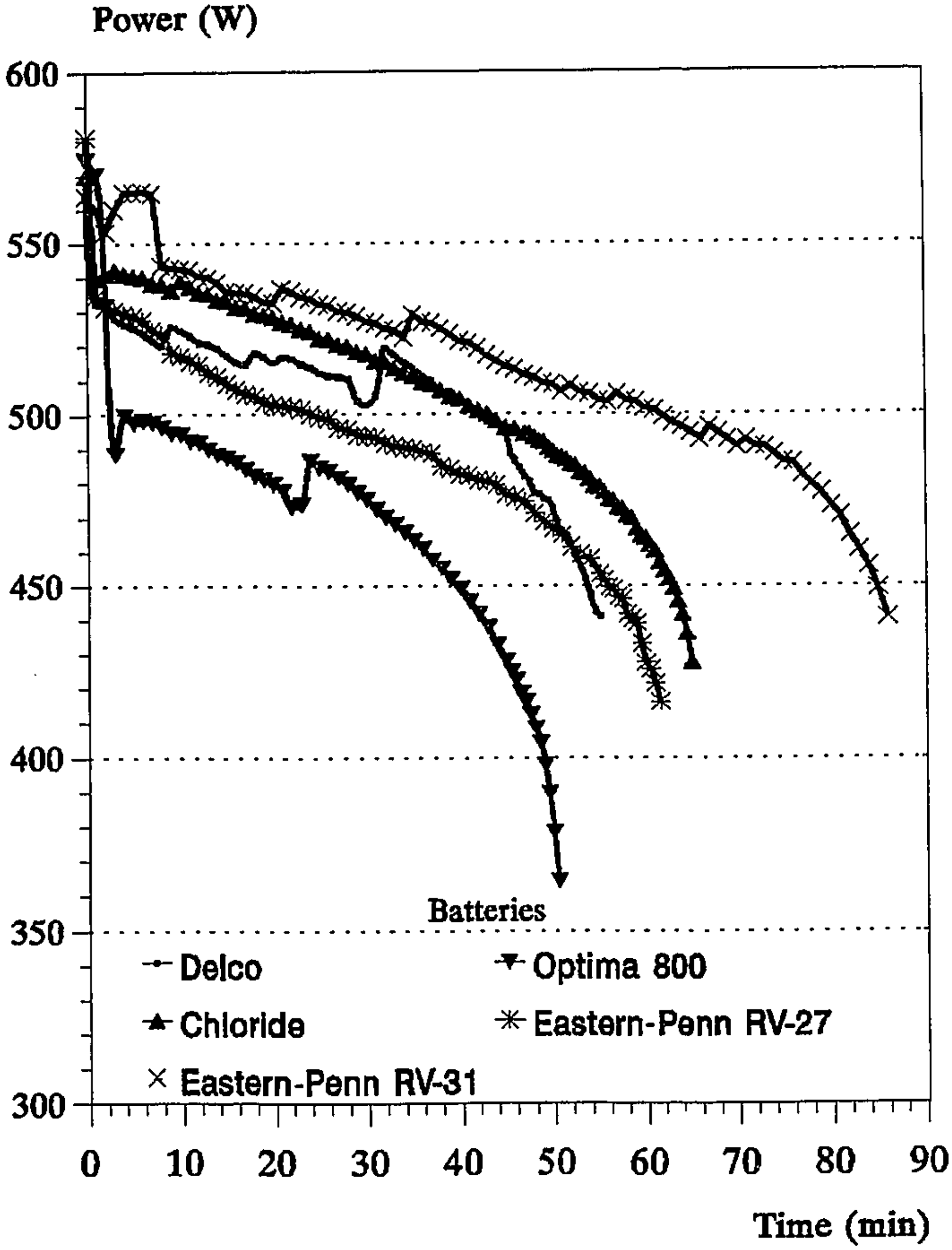

Fig. 6.3 Energy Dissipated at a 45A Continuous Draw [22]

Table 6.2 Summary of the Energy Dissipated - Constant Current Testing

Battery Tested	Total Energy Dissipated (W·h)	Energy Density (W·h/kg)
Optima 800	396.3	22.0
Chloride 6EF7	507.9	19.5
Delco Voyageur 27FMF	464.3	19.3
Eastern-Penn RV27	549.3	22.3
Eastern-Penn RV31	734.7	25.8

The energy density outlined above, determines the obtainable energy of each battery system only at one specific condition, that being at a constant current discharge of 45 A. It is important to note that the energy of a battery system is hardly a constant, since it involves an electro-chemical process, which is strongly dependent on the applied load. For example, a typical lead-acid battery can provide an energy density of 15 W·h/kg or 30 W·h/kg, when subjected to 750 W or 400 W power consumptions, respectively. To properly obtain the energy characteristics which a battery can provide throughout its entire operating spectrum, constant power tests are essential.

6.1.2 Constant Power Battery Testing

Using the previously outlined battery set-up, constant power tests were performed for the Eastern-Penn RV31 lead-acid battery. A slightly different set-up was used to test two nickel-cadmium batteries, namely a Saft Nife STM 1.130 and a Marathon 44SP100. The nickel-cadmium cells had a nominal open circuit voltage of 1.3 V. This low voltage was insufficient to operate the DC to AC inverter, therefore a different battery test set-up was developed in order to perform constant power testing on the two nickel-cadmium cells. This test set-up consisted of a data acquisition system, high power rated resistors, and a bank of potentiometers, which were adjusted accordingly in order to maintain a constant power discharge during the battery tests (See Fig. 6.4).

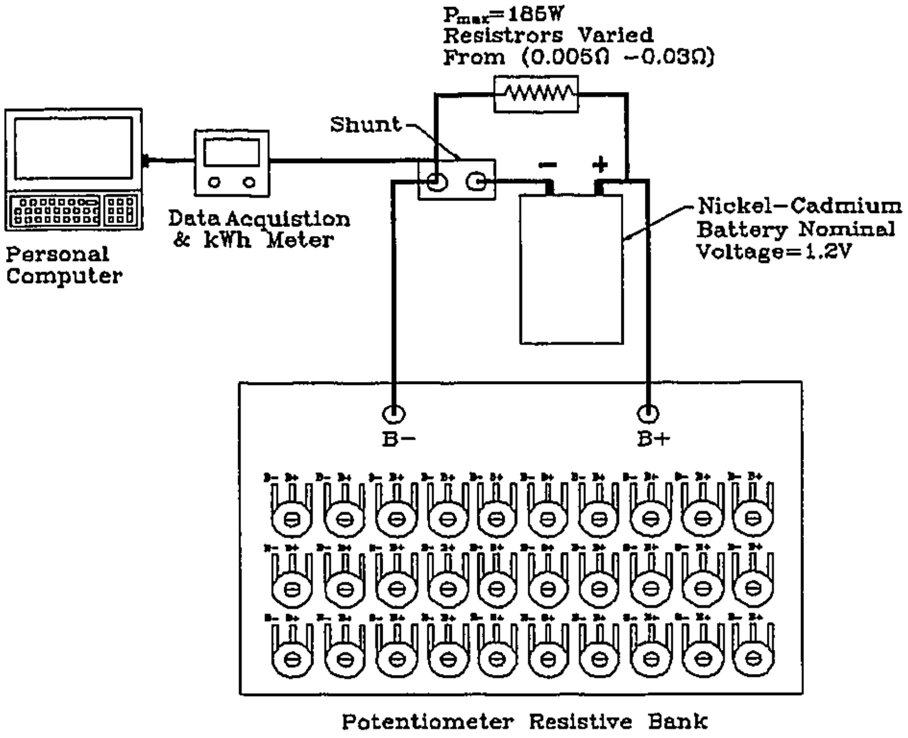

Fig. 6.4 Constant Power Test Set-Up for Nickel-Cadmium Batteries

To obtain adequate information on the batteries performance, various different constant power discharge tests were performed for all the three batteries (See Table 6.3).

Table 6.3 Overview of the Constant Power Tests

Eastern-Penn RV31		Saft Nife STM 1.130		Marathon 44SP100	
Constant Power (W)	Time (min)	Constant Power (W)	Time (min)	Constant Power (W)	Time (min)
300	209	28	300	8	433
400	140	37	216	12.7	270
550	88	70	94	33	104
650	71	118	79.5	47.7	68
700	61	148	33.8	76	39.5
850	36	185	24	110	23

This type of testing is essential for obtaining the energy and power density of a battery throughout its entire operating spectrum. However, it is very time consuming, for each test varies from 23 to 433 minutes, excluding the 8 to 10 hour battery recharging time. Using the Universal Battery Model outlined in the literature review, an attempt to obtain analytically the power and energy characteristics of a battery at a minimal amount of time, was investigated (See Section 6.2).

Ragone Curves were established from the information outlined in Table 6.3, as well as, the weight of each tested battery system:

- Saft Nife STM 1.130 - 3.70 kg,
- Marathon 44SP100 - 1.59 kg, and
- Eastern-Penn RV31 - 28.50 kg.

The graphical representation of the power density versus energy density of these batteries is illustrated in Fig. 6.5.

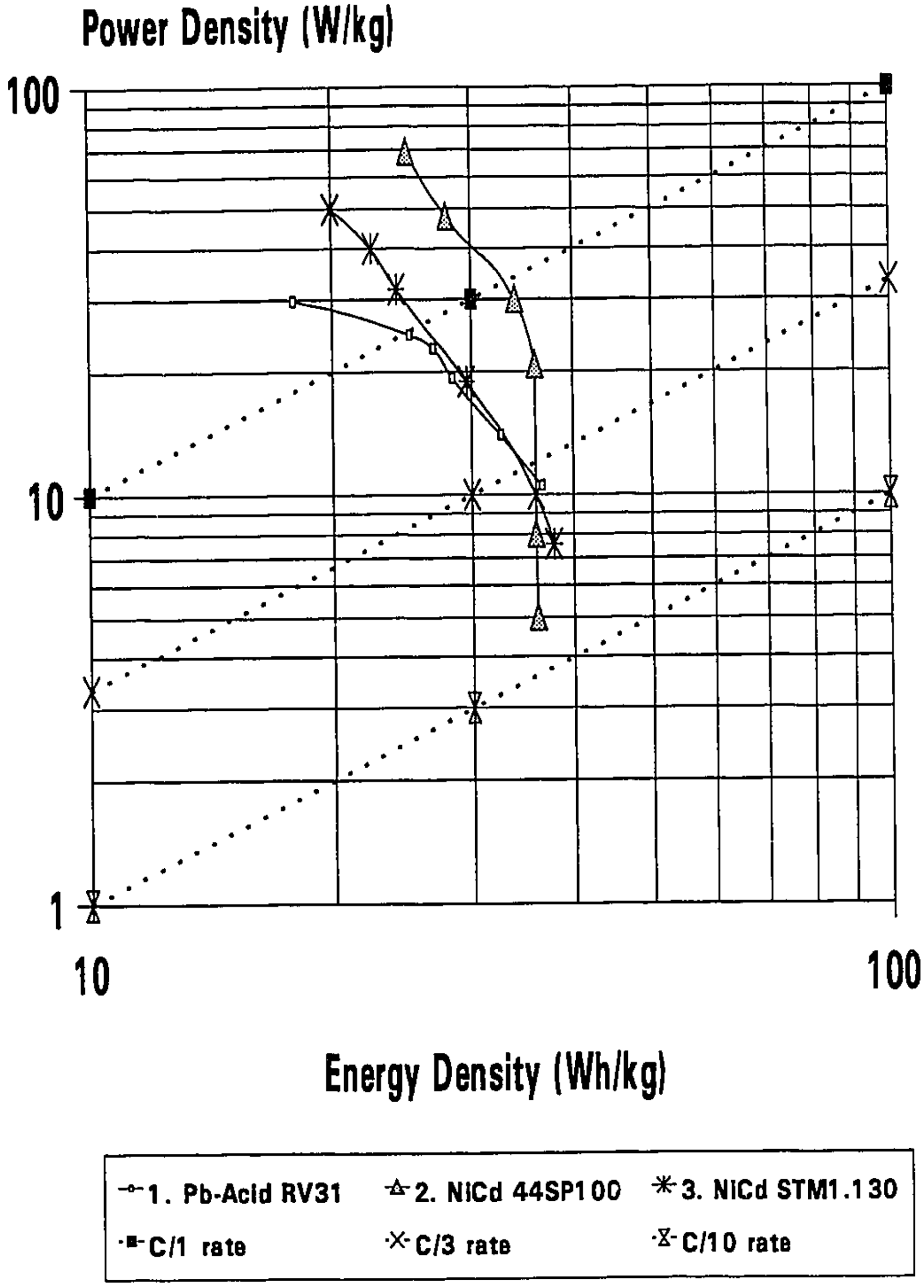

Fig. 6.5 Ragone Curve - Power Density Versus Energy Density

Using the energy and power density, based on a C/1 rating in Fig. 6.5, an analysis was established which outlined the maximum energy, operating voltage and battery pack weight for each of the three tested batteries. The results of this analysis are shown in Table 6.4. It becomes very clear that in selecting a battery system for HEVs or EVs compromises must be made between, battery pack weight, operating voltage and energy. As shown in the Table 6.4, the operating voltage of the STM 1.130 battery system is limited to 150 V, due to the 425 kg weight restriction imposed during the weight distribution analysis, however it provides 11.7 kWh of energy. On the other hand, if 130 Marathon 44SP100 cells are connected in series, a nominal voltage of 169 V is obtained, having a total weight of 209 kg. If two such battery systems are connected in parallel a total energy of 14.2 kWh is obtained at a combined weight of 418 kg. Finally, the Eastern-Penn RV31 is capable of providing 9.3 kWh of energy at an operating voltage of 168 V.

Table 6.4 Analysis of the Three Storage Systems

Battery System	Eastern-Penn RV31	Marathon 44SP100	Saft Nife STM1.130
Cells - Voltage per Cell	13 - 12 V	130 - 1.3 V	114 - 1.3 V
Battery Pack Weight (kg)	371	209	425
Nominal Voltage (Volts)	168	169	150
Energy Density (C/1) Rate (Wh/kg)	25	34	27.5
Energy of the Battery System (C/1) Basis (kWh)	9.3	7.1	11.7

It becomes very difficult to establish what is the best design trade off between, energy, weight and operating voltage, since the effects which these design parameters have on the HEV's performance, namely acceleration, range and cost per performance of the energy storage system are unknown. It is for this reason that a scientific approach was developed in the form of a multi-objective optimization which analyzes all these key design parameters (See Chapter 7).

6.2 Universal Battery Model Investigation

An analytical investigation on the Universal Battery Model was performed for the RV31, STM1.130, and the 44SP100 battery systems. Thereafter, the analytical results of the energy and power density of each battery were compared with the experimental constant power tests results outlined in Section 6.1.3. The main objective was to see if the Universal Model could conservatively predict the energy and power density of a battery. If so, the benefits would be as follows:

- reduced battery testing time, and
- fewer batteries would be purchased for testing, for the model would predict the performance characteristics.

6.2.1 Overview of the Universal Battery Model

The basis of the Universal Model is to analyze a battery system by a simple electrical circuit, consisting of the batteries internal resistance, and the applied load resistance. A valid assumption, is to assume that the load resistance is equal to the batteries internal resistance (See Fig. 6.6).

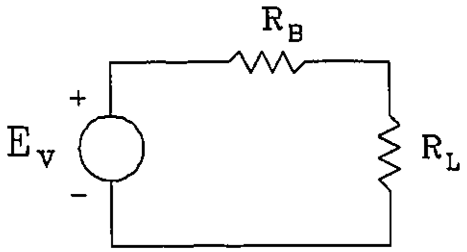

where:
R_B= Battery Internal Resistance
R_L= Load Resistance
R_B= R_L

Fig. 6.6 Simplified Battery Electrical Circuit

Since, the power is the most meaningful method of rating a battery for HEV or EV applications, half the voltage will be used to define the maximum power. Adapting such a concept and the batteries equivalent electric circuit, the maximum peak power is defined as follows [30]:

$$P_{\max} = \frac{E_v^2}{4R_{eq}} \tag{6.1}$$

where:

P_{max} - Maximum Battery Peak Power

E_v - Terminal Load Voltage

R_{eq} - Equivalent Resistance

The terminal load voltage as a function of depth of discharge (DOD) can be obtained from the battery manufacturer or by a high discharge rate load test. In this study, the actual terminal voltage as a function of DOD was obtained experimentally for all the three batteries and is graphically represented in Fig. 6.7.

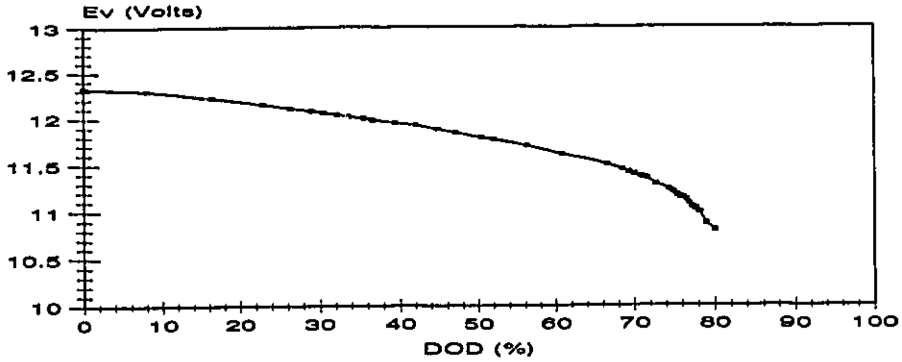

a) E_v versus DOD - RV31 Lead-Acid Battery

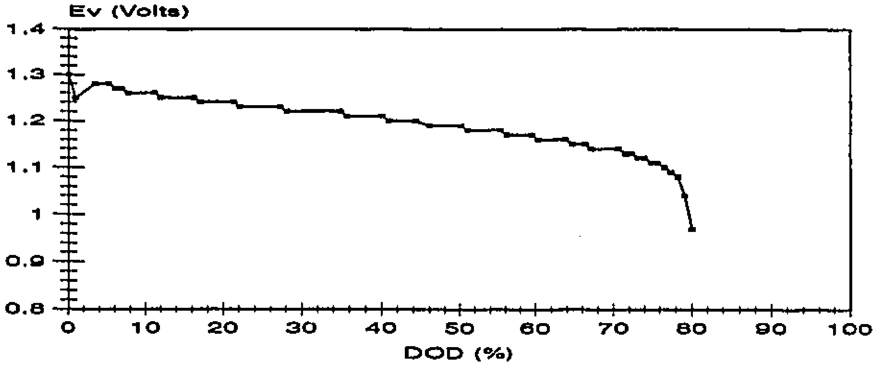

b) E_v versus DOD - STM1.130 Nickel-Cadmium Battery

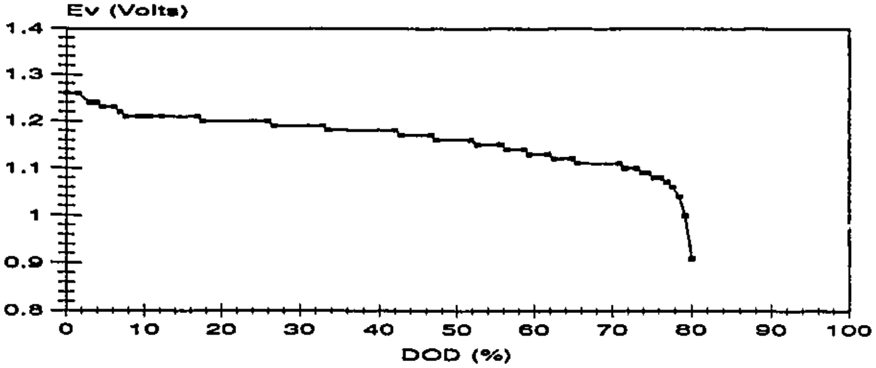

c) E_v versus DOD - 44SP100 Nickel-Cadmium Battery

Fig. 6.7 Load Voltage Versus Depth of Discharge

The peak power of each battery was obtained, based on the maximum current the respective battery could provide. A summary of the results is shown in Table 6.5.

Table 6.5 Maximum Peak Power Summary

Battery	Average Current (A) (30 sec basis at 80% DOD)	Average Voltage (V) (30 sec basis at 80% DOD)	P_{max} (W)
Eastern-Penn RV31	650	11.8	7 670
Saft Nife STM 1.130	828	0.99	819.7
Marathon 44SP100	687.5	1.1	756.3

The load voltage of interest is at 80% DOD of discharge for all three batteries due to the fact that the voltage basically starts to collapse beyond this point. With reference to Fig. 6.7, the load voltage of each system, at 80% DOD is obtained and used in equation (6.1) along with the P_{max}. Thereafter, equivalent resistance is obtained by solving for R_{eq} in equation (6.1). The equivalent resistance of each battery and the load voltage at 80% DOD is summarized in Table 6.6.

Table 6.6 Load Voltage at 80% DOD and Equivalent Battery Resistance

Battery	E_v 80% DOD (V)	R_{eq} (Ω)
Eastern-Penn RV31	10.80	4.54×10^{-3}
Saft Nife STM1.130	0.97	2.87×10^{-4}
Marathon 44SP100	0.91	4.0×10^{-4}

The discharge current that a battery can achieve, based on a specified constant power, is calculated by the following quadratic equation [30]:

$$I_d = \frac{E_v \pm \sqrt{E_v^2 - 4R_{eq}P_{\max}}}{2R_{eq}} \tag{6.2}$$

The calculation of a battery efficiency is also incorporated in the model, which takes into account the heat loses of the battery system. The battery efficiency is a function of the maximum peak power and desired discharge power and is given as:

$$\eta^2 - \eta + \frac{P}{P_{\max}} = 0 \tag{6.3}$$

where: P - Desired Battery Discharge Power (W)

η - Battery Efficiency

A graphical representation of P/P_{max} versus η is illustrated in Fig. 6.8.

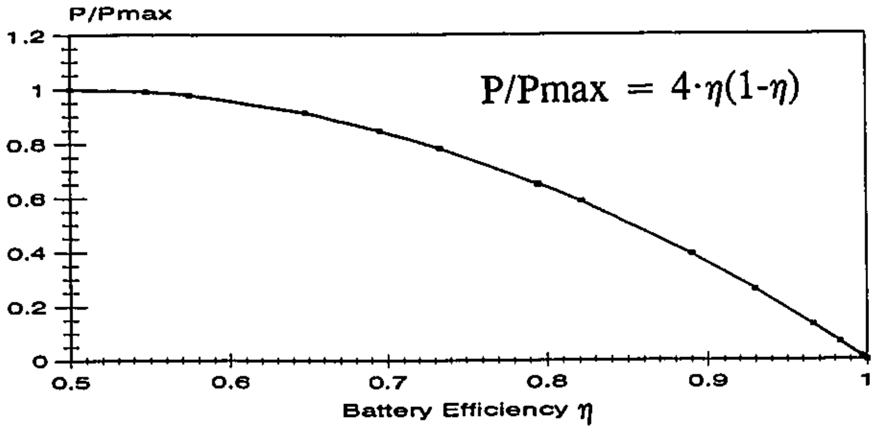

Fig. 6.8 P/P_{max} Versus Battery Efficiency η [30]

Prior to presenting the calculated discharge current results for each system, the A·h energy capacity must be defined. The Universal Model utilizes a constant energy rating in terms of A·h, for all discharge current at a C/1 rate, in order to obtain very conservative results. However, the energy of a battery, as mentioned previously, has a strong dependence on discharge current, therefore an alternative method for projecting energy will be developed. During this research an in depth empirical analysis was performed, which enables the calculations for different A·h ratings. By obtaining an A·h rate from a battery manufacturer or through testing, say for example on a C/1 basis, the other rates can be estimated by using the following multiplication factors outlined in Table 6.7.

Table 6.7 Energy Capacity Rating Empirical Correlation

Capacity Rating	C/0.25	C/0.5	C/1	C/2	C/3	C/3.5	C/4	C/5	C/6	C/7	C/8	C/10
A·h Correlation Factor	0.66	0.83	1.00	1.14	1.23	1.27	1.31	1.36	1.40	1.43	1.45	1.50

The reference A·h ratings obtained from the battery manufacturer's are as follows:

- RV31 - 80.5 A·h C/3.5 basis,
- STM1.130 - 125 A·h C/5 basis, and
- 44SP100 - 44 A·h C/1 basis.

Having established the complete battery model, the discharge current is calculated from equation (6.2), while the battery efficiency is calculated from equation (6.3). Using the empirical factors in Table 6.7, along with a reference energy capacity obtained by the battery manufacturer, the energy capacity for any basis can be obtained. Also, a projected discharge current and time duration is established by obtaining the energy capacity of a battery at different basis. The projected energy capacity, and discharge rates for all the three batteries are illustrated in Table 6.8.

Table 6.8 Projected Energy Capacity and Discharge Current

Eastern- Penn RV31

Capacity Rating	C/0.25	C/0.5	C/1	C/2	C/3	C/3.5	C/4	C/5	C/6	C/7	C/8	C/10
A·h	41.8	52.6	63.4	72.2	77.9	80.5	83.1	86.2	88.8	90.7	91.9	95.1
Current (A)	105.2	63.4	63.4	36.2	26.0	23.0	20.8	17.2	14.8	13.0	11.5	9.5

Saft Nife STM 1.130

Capacity Rating	C/0.25	C/0.5	C/1	C/2	C/3	C/4	C/5	C/6	C/7	C/8	C/10
A·h	60.6	76.1	91.9	104.8	112.9	120.4	125	128.7	131.4	133.3	137.9
Current (A)	241.2	152.2	91.9	52.4	37.6	30.1	25	21.5	18.8	16.7	13.8

Marathon 44SP100

Capacity Rating	C/0.25	C/0.5	C/1	C/2	C/3	C/4	C/5	C/6	C/7	C/8	C/10
A·h	32.3	40.7	49.0	55.9	60.3	64.2	66.6	68.6	70.1	71.1	73.5
Current (A)	129.0	81.3	49.0	28.0	20.1	16.1	13.3	11.4	10.0	8.9	7.4

The calculated current for each battery system is outlined in Table 6.9, along with their respective energy capacity projection. If the calculated current fell in between two of the projected discharge current rates, linear extrapolation was used to obtain the energy capacity of the battery system. The time at which each system could maintain the respective power, is calculated as follows:

$$Time = \frac{Q}{I_d \eta} \tag{6.4}$$

where: Q - Battery energy capacity as a function of calculated discharge current

Table 6.9 Calculated Discharge Current and Anticipated Time Duration

Eastern - Penn RV31

P (W)	η (%)	I_d (A)	$(I_d \cdot \eta)/100$ (A)	Q (A·h)	Time (h)
300	99.00	28.1	27.8	74.7	2.69
400	98.70	37.6	37.1	72.2	1.94
550	98.20	52.1	51.1	67.4	1.32
650	97.80	61.8	60.4	64.4	1.07
700	97.70	66.7	65.2	62.9	0.96
850	97.10	81.5	79.1	59.3	0.75

Saft Nife STM 1.130

P (W)	η (%)	I_d (A)	$(I_d \cdot \eta)/100$ (A)	Q (A·h)	Time (h)
28	99.76	29.1	29.0	121.4	4.18
37	98.85	38.6	38.2	112	2.94
70	97.82	73.8	72.2	98.3	1.36
118	96.26	126.4	121.7	84.1	0.96
148	95.26	160.2	152.6	76.1	0.50
185	94.00	202.9	190.7	69.4	0.36

Marathon 44SP100

P (W)	η (%)	I_d (A)	$(I_d \cdot \eta)/100$ (A)	Q (A·h)	Time (h)
8.0	99.76	8.82	8.80	71.0	8.07
12.7	99.61	14.04	13.98	66.0	4.72
33.0	98.98	36.86	36.48	53.1	1.45
47.7	98.52	53.68	52.89	48.0	0.91
76.0	97.63	86.83	84.77	40.1	0.47
110.0	96.52	128.10	123.60	33.3	0.27

Using the results summarized in Table 6.9, the theoretical energy and power density was calculated for all the three battery systems, and was compared with their respective experimental energy and power density results. This comparison is outlined in the form of Ragone Curves in Figs. 6.9, 6.10, and 6.11.

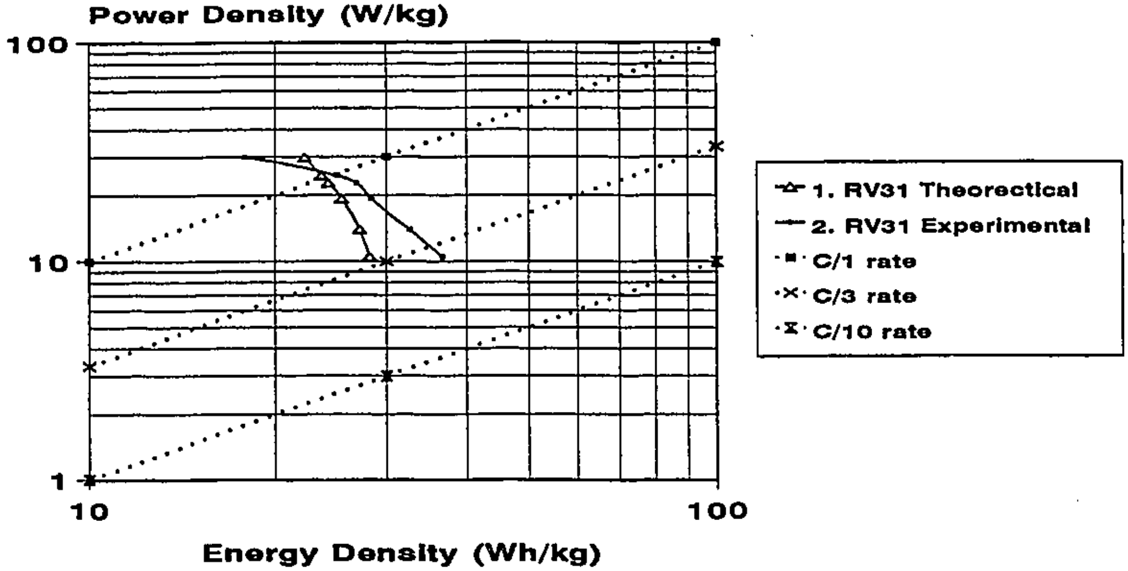

Fig. 6.9 Ragone Curve RV31 - Experimental and Theoretical Comparisons

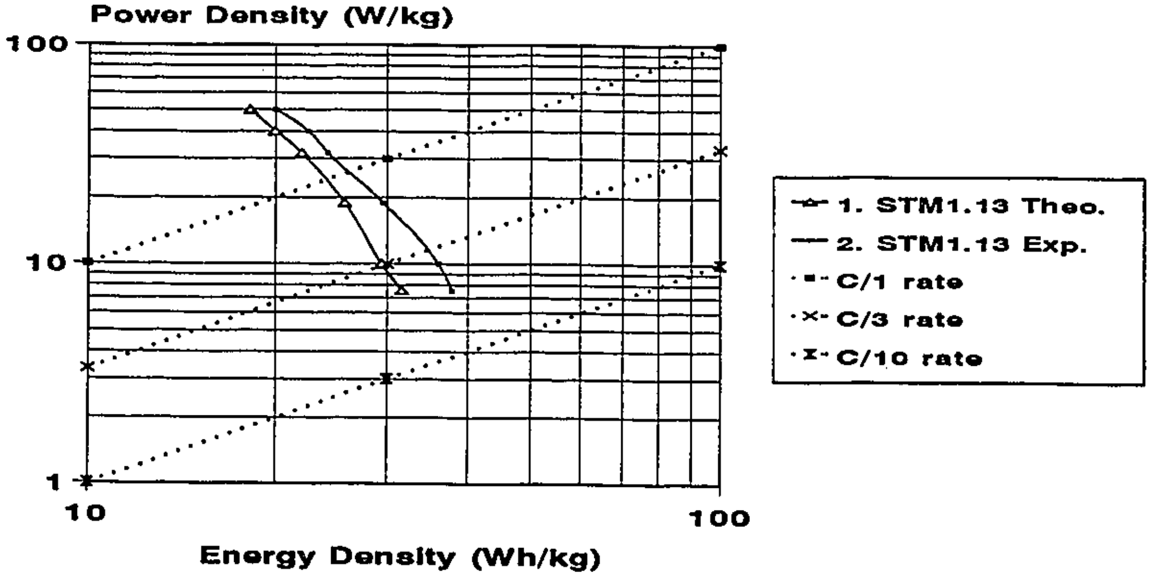

Fig. 6.10 Ragone Curve STM1.130 - Experimental and Theoretical Comparisons

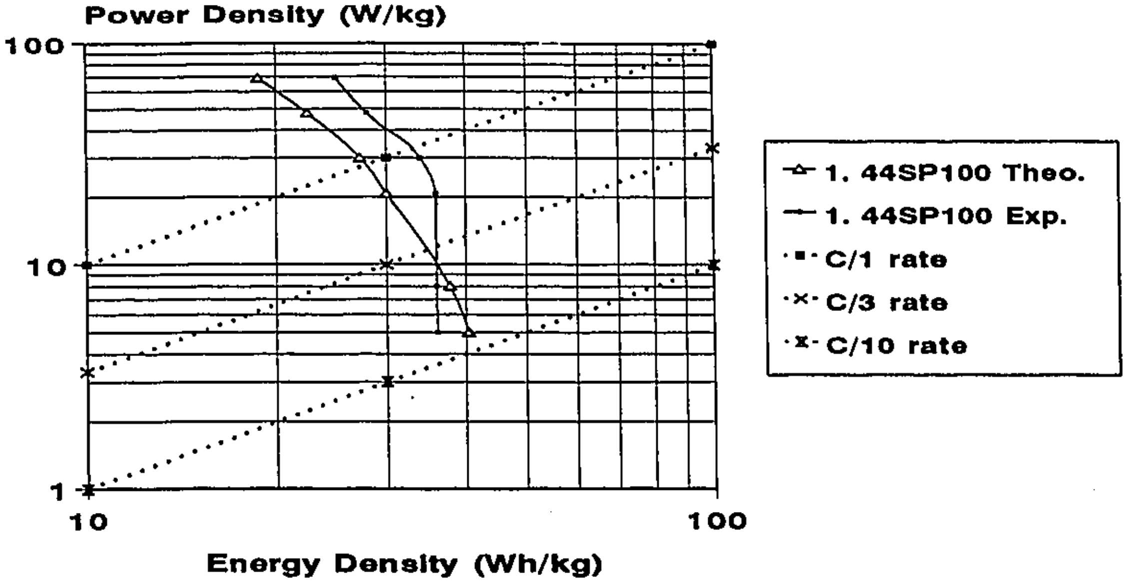

Fig. 6.11 Ragone Curve 44SP100 - Experimental and Theoretical Comparisons

The results obtained from the modified Universal Battery Model were very conservative, and therefore could be used when resources, such as time and research money are at a premium. One should not forget that the advanced battery systems are very costly; therefore with the aid of such a battery modelling technique one can obtain the essential battery characteristics required to perform a reasonable analysis. The percent deviation of the theoretical results from the experimental results for the RV31, STM 1.130 and 44SP100 batteries was 6.52%, 12.05%, and 19.3 %, respectively. This was calculated based on a C/1 basis which most effectively represents a high performance HEV or EV.

6.3 Summary

The A·h energy capacity and reserve minutes capacity were the two main battery performance ratings discussed. Thereafter, 45A constant current tests were performed on five commercially available lead-acid batteries, with the results being presented. In terms of energy, the Eastern-Penn RV31 outperformed all the tested lead-acid batteries. In order to understand the entire energy and power density spectrum of a battery system, some constant power tests were performed. The batteries tested were the lead-acid RV-31 and two nickel-cadmium batteries, namely Saft Nife STM1.130 and the Marathon 44SP100. Through the use of the constant power test results, the energy and power density of the tested batteries were obtained. To minimize the testing time and funds, an analytical means of estimated power and energy density was established by introducing an empirical correlation of energy capacity into the Universal Battery Model. Thereafter, the results of the constant power tests were compared with the analytical results obtained through the modified Universal Battery Model. The analytical results were found to be very conservative and, therefore, could be used to project the range, energy, and acceleration of a HEV, as will be the case in Chapter 7, where a multi-objective optimization procedure will be used.

7. HEV ELECTRIC MODE OPTIMIZATION

Research and development of energy storage systems and electric drive units has been very extensive in the past few years. However, a more scientific approach of selecting optimal design parameters has to be elaborated.

To increase the performance of electric vehicles, a proper selection of the battery pack mass, operating voltage, energy storage system and gear ratios is required. In order to design a complex engineering system, whose performance depends on several conflicting requirements, multi-objective optimization techniques should be applied. In this chapter, to properly understand the impact of these conflicting design parameters on the performance of the electric drive system, a graphical optimization method is being used with the aid of a simulation program. A detailed multi-parameter optimization, using nonlinear programming techniques, is also carried out and the results are presented.

7.1 Preliminaries: Electric Drive System

As proposed in Chapter 4, the electric drive system incorporates two electric motors installed in a Ford Escort Wagon. The first motor is a Solectria BRLS16 permanent magnet brushless DC motor and the second is an Advanced DC series wound motor, model 203-06-4001. Since these motors function on different electromotive principles, synchronization is necessary. This is achieved by modifying the deadband region of the permanent magnet motor through the use of electric circuitry. Another aspect is the selection of the maximum power region of each motor. The Solectria BRLS16 motor provides peak power (22 kW) at a speed of 4500 rpm, whereas the peak power of Advanced DC (33 kW) occurs at a speed of 4000 rpm (See Fig. 7.1).

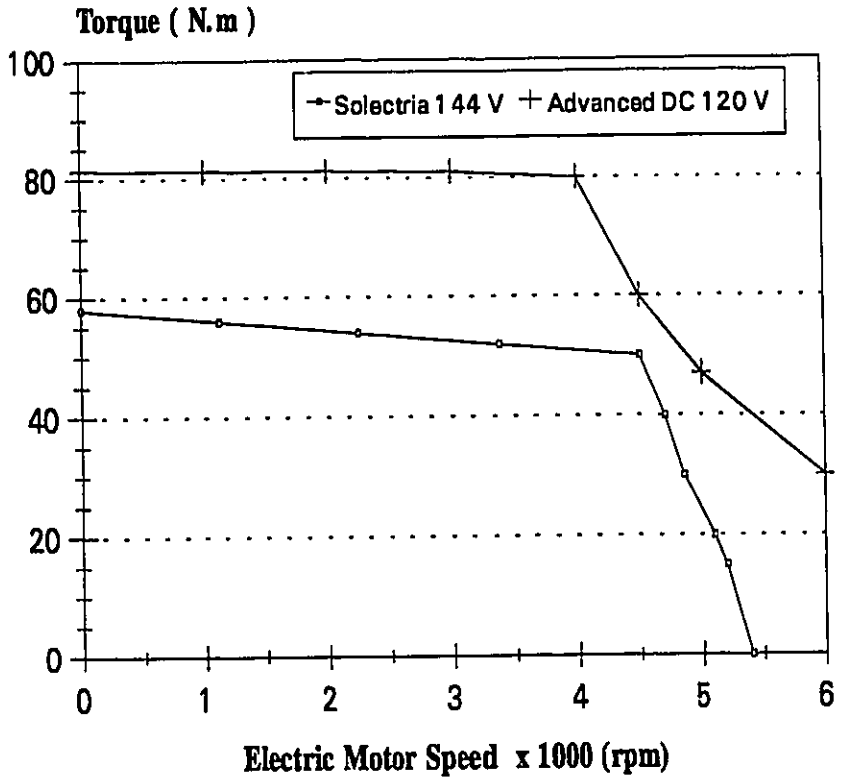

Fig. 7.1 Torque-RPM Curves, Solectria 144V and Advanced DC 120V [25][31]

To properly synchronize both electric motors at their respective peak power condition, the electric final drive ratio, which will be obtained from the optimization procedure, will be reduced according to the Advanced DC motor, since its peak design speed is lower than that of the Solectria electric motor. The electric drive final drive ratio in this context refers to the sprocket diameter ratio between the electric motor and the shaft extension, as outlined in Fig. 5.5. The electric final drive ratio (N_g) obtained from the optimization, will be the same for the Solectria electric motor, however, the following relationship will be applied for the Advanced DC electric motor ratio:

$$N_{ga} = N_g \cdot \frac{(4000)}{(4500)} = 0.89\ N_g \qquad (7.1)$$

The objective of such a design is to provide better acceleration, in comparison to a vehicle equipped with two Solectria motors. During highway driving conditions, a control system disables the series wound motor; therefore the Solectria motor provides the entire power required to maintain the vehicle at the desired speed. This enables the Solectria to take over the full load, mapping an efficiency as high as 93%.

The combined electric drive system is very attractive, for it minimizes the cost of the electric drive by incorporating the series wound motor and controller as an acceleration unit, which is three and a half times less expensive than the permanent magnet motor and controller. The series wound motor provides sufficiently greater power; on the other hand, the regenerative braking features of the permanent magnet motor provide up to 13% of energy recuperation, during city driving.

7.1.1 Design Criteria for the Electric Mode of Operation

The objectives which were selected to analyze the design parameters are as follows:

- time required to accelerate the vehicle up to a speed of 72 km/h,
- range of the vehicle (full charge basis) travelling at 72 km/h on a flat surface,
- energy capacity of the battery pack,
- cost of the battery pack, and
- anticipated cycle life at 80% DOD which is represented in terms of total obtainable range of the energy storage system during its entire life.

Each of the objectives will be mathematically modelled and thereafter analyzed by a simulation program established in FORTRAN. The design parameters of interest in this study are:

- battery pack mass (M_B),
- electric drive final gear ratio (N_g),
- operating voltage of the electric drive system (V_{OS}), and
- specific energy of the storage system (S_E).

Vehicle design parameters such as coefficient of drag and frontal area, were excluded from the optimization study, since their effect on the vehicle performance can not be varied.

A maximum weight restriction of 425 kg was placed on the energy storage system, due to the GVW rating of the vehicle. The vehicle weight without any batteries was 1308 Kg. The coefficient of drag, frontal area and tire rolling resistance used in the analysis was $c_d=0.36$, $A_f=1.976$ m^2 and , $\mu_{const}=0.0085$, respectively.

7.1.2 Mathematical Representation of the Objective Functions

In order to perform a multi-objective optimization, appropriate mathematical models were developed for each objective function.

The mathematical model used to calculate acceleration and actual loads acting on the vehicle is outlined below. The three fundamental resistive forces discussed in Chapter 4 are:

Aerodynamic drag force:

$$F_a = \frac{\rho C_d A_f}{2}(V_{HEV} \pm V_w)^2 \tag{7.2}$$

Rolling resistive force:

$$F_{ro} = \mu_r m g \cos(\theta) \tag{7.3}$$

An empirical relationship of the tire rolling resistance as a function of vehicle speed is outlined in equation (7.4) [32].

$$\mu_r = \mu_{const} + (0.0015 + \frac{V_{HEV}}{27.77}) \tag{7.4}$$

Climbing resistive force:

$$F_{inc} = mg\sin(\theta) \tag{7.5}$$

Total resistive force:

$$F_{resistive} = F_a + F_{ro} + F_{inc} \tag{7.6}$$

Force developed at the wheels:

$$F_{dw} = (F_{sm}\eta_{es} + F_{am}\eta_{ea})\eta_m \tag{7.7}$$

Since, the combined electrical efficiency map of the Advanced DC motor and Curtis Controller was strongly dependent on torque, it was simply modelled as a piece-wise linear function (See Fig. 7.2).

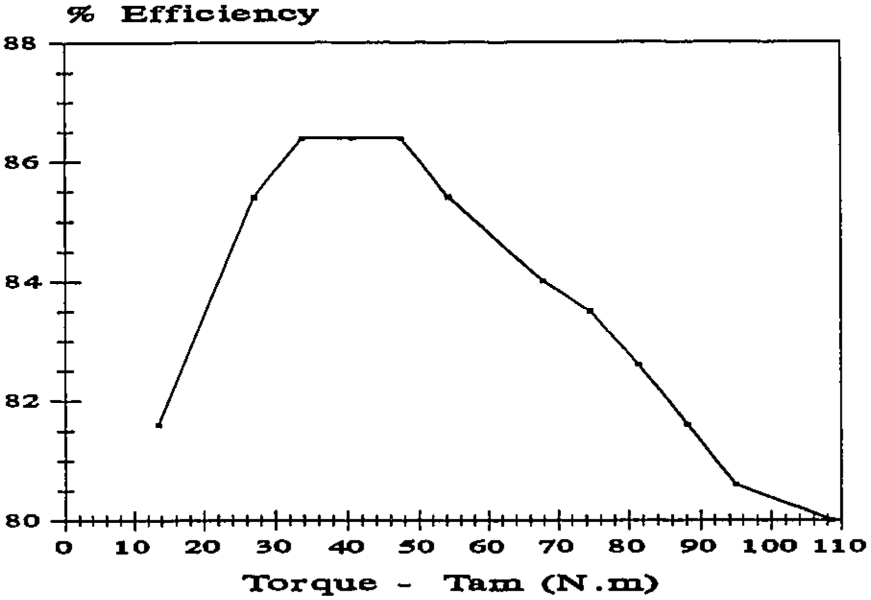

Fig. 7.2 Advanced DC and Curtis Controller Electric Efficiency Map

The electrical efficiency of the Solectria BRLS16 motor and controller was strongly dependent on the torque and speed conditions; therefore it was modelled in the form of a look-up table. Fig. 7.3 illustrates graphically the efficiency map of the Solectria BRLS16 motor and controller, which was used to formulate the look-up table.

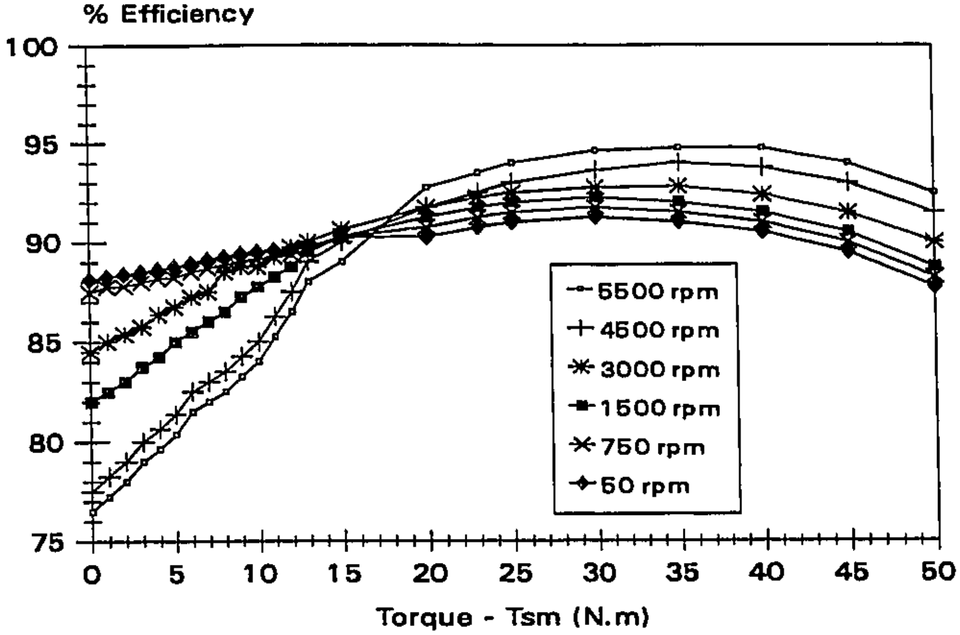

Fig. 7.3 Solectria Motor and Controller Electrical Efficiency Map

The force developed by the electric motors was modelled as a function of the operating voltage of the electric drive system. Due to the fact that the operating voltage of the system would be obtained from the optimization, some conditional constraints were imposed on the voltage of the Advanced DC, in order to ensure that its maximum operating voltage of 120 V would be respected. On the other hand, the Solectria could effectively be tuned to operate at voltages as high as 168 V. For example, if the optimization procedure would determine an operating voltage of 144 V, the battery pack could be designed to provide such a voltage. However, a DC to DC converter would be implemented to limit the voltage of the Advanced DC motor to 120 V, while the Solectria motor would be connected directly to the 144 V supply. In order to model this type of scenario, the following conditions were applied to the simulation:

Torque of Solectria is calculated as follows:

$$T_{sm} = Kt \cdot V_{OS} - Kb \cdot \omega_m \tag{7.8}$$

with

$$\omega_m = \frac{V_{HEV} \cdot N_g \cdot N_{gi} \cdot N_f}{r} \tag{7.9}$$

where :

Kt = 0.403 N·m/V (torque constant of Solectria BRLS16)
Kb = 0.0167 N·m·s/rad (slope of torque speed curve Solectria BRLS16)
V_{HEV} - velocity of the HEV (m/s)
Thereafter the force produced by the solectria is obtained as:

$$F_{sm} = \frac{T_{sm} \cdot N_g \cdot N_{gi} \cdot N_f}{r} \tag{7.10}$$

The torque of the Advanced DC was constant throughout the preset operating motor speed of 4000 rpm (See Fig. 7.1); therefore, to establish the torque relationship as a function of operating voltage, only the torque constant (Kt=0.678 N·m/V) was required. Equation (7.11) outlines the torque relationship of the Advanced DC motor as a function of operating voltage, along with the voltage constraint used in the simulation.

$$\begin{aligned} T_{am} = Kt \cdot V_{OS} \qquad & if\ V_{OS} \le 120V \\ & else\ T_{am} = Kt \cdot 120V \end{aligned} \tag{7.11}$$

The force of the Advanced DC motor is, thereafter calculated as:

$$F_{am} = \frac{T_{am} \cdot N_{ga} \cdot N_{gi} \cdot N_{f}}{r} \tag{7.12}$$

The tractive effort provided by the two electric motors is calculated as follows:

$$F_{tractive} = F_{dw} - F_{resistive} \tag{7.13}$$

The maximum tractive force which can be developed on the front wheel drive of the HEV is limited by the road adhesion, and is calculated by the following expression (See Fig. 7.4) [33].

$$F_{dw} \max = \frac{\dfrac{a \mu_s W}{L}}{1 + \dfrac{\mu_s h_{CG}}{L}} \tag{7.14}$$

By substituting, the following parameters:

- wheelbase length L= 2.541m
- center of gravity height ($h_{CG} = 0.508$m),
- coefficient of road adhesion ($\mu_s = 0.85$), and
- a=0.527·L under the assumption of a front/rear weight distribution of 47.3/52.7%.

The limitation of the tractive effort, due to the road adhesion, is obtained by simplifying equation (7.14):

$$F_{dw} \max = 0.383\, m\, g$$

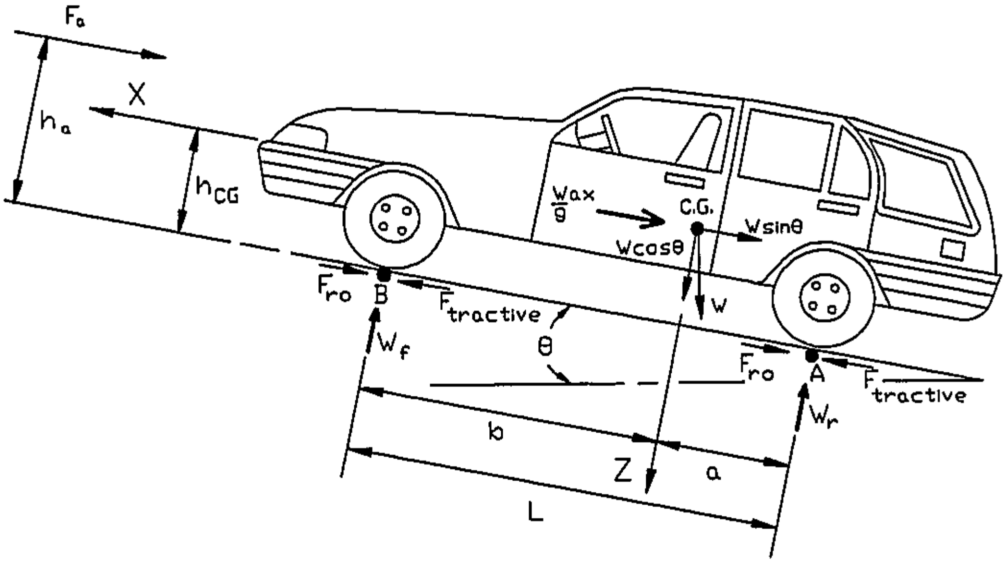

Fig. 7.4 Free Body Diagram of HEV

The effective inertia of the vehicle is obtained in a similar fashion as outlined in equation 4.14, while the effective mass outlined in equation 4.19 is slightly modified in the sense that the total vehicle mass of the HEV (m), is broken down into two components. The first component represents the battery mass variable (M_B), while the other represents the HEV's total mass excluding the battery system (M_{WB} = 1308 kg). By establishing the relationship of effective mass in this manner, the effects on acceleration can be analyzed with respect to the change in battery mass. The modified effective mass equation is as follows:

$$Meff = M_B + M_{WB} + \frac{Jeff}{r^2} \tag{7.15}$$

The first objective function, acceleration time of the vehicle can, therefore, be calculated by the following expression:

$$t = Meff \int_{V1}^{V2} \frac{dV}{F_{tractive}} \tag{7.16}$$

The energy and power density, cost and cycle life data which will be used in this analysis, have been obtain from battery testing and modelling procedures outlined in Chapter 6, and from various other sources [34], [35], [36], [37], and [38]. A voltage to mass ratio was also calculated for all energy systems. This would provide an indication of the operating voltage which the energy system in question could obtain for a specified battery mass (See Table 7.1).

Table 7.1 Cycle Life and Cost of Energy Storage Systems

Battery Number x_i	Energy Storage System	Specific Energy (W·h/kg) C/3	Cycle Life 80% DOD	Estimated Cost ($/kWh)	Ideal Voltage mass ratio
1	Pb-Acid ideal min.	27	450	80	0.71
2	Pb-Acid ideal max.	33	600	120	0.42
3	NiCd ideal min.	35	1200	1000	0.69
4	NiMH ideal min.	50	500	800	0.48
5	NiMH ideal max.	51	500	800	0.48
6	NiFe ideal	51	1000	800	0.25
7	NiCd intermed.	55	1200	1000	0.26
8	ZnBr ideal	56	500	500	0.50
9	NiCd ideal max.	64	1200	1000	0.26
10	NiZn ideal min.	72.8	600	350	0.27
11	NiZn ideal max.	79.3	600	350	0.27
12	NaS ideal min.	79	1000	650	0.35
13	NaS ideal max.	81	1000	650	0.36
14	AgZn ideal min.	117	100	1500	0.50
15	AgZn ideal max.	139	100	1500	0.50
16	Zn-Air ideal min.	144	150	1500	0.26
17	Zn-Air ideal max.	161	150	1500	0.26

The power required to maintain the vehicle at a constant speed of 72 km/h is calculated as follows:

$$Power = \frac{V_{HEV} \cdot F_{resistive}}{\eta_{es} \cdot \eta_{m}} \qquad (7.17)$$

Equation (7.17) only takes into account the electrical efficiency of the Solectria, for it is under the assumption that the Advanced DC will only be used during acceleration condition.

The ideal characteristics of energy storage systems in Table 7.1 are represented by higher order polynomials which are thereafter used in the simulation program. The polynomials correlate energy density (x_i) as a function of power density (y); the subscript refers to the battery system. Therefore,

$$y = \frac{Power}{M_B} \tag{7.18}$$

$$x_i = ay^5 + by^4 + cy^3 + dy^2 + ey + f \tag{7.19}$$

The Ragone curves of ideal battery systems are shown in Figs. 7.5, 7.6, and 7.7.

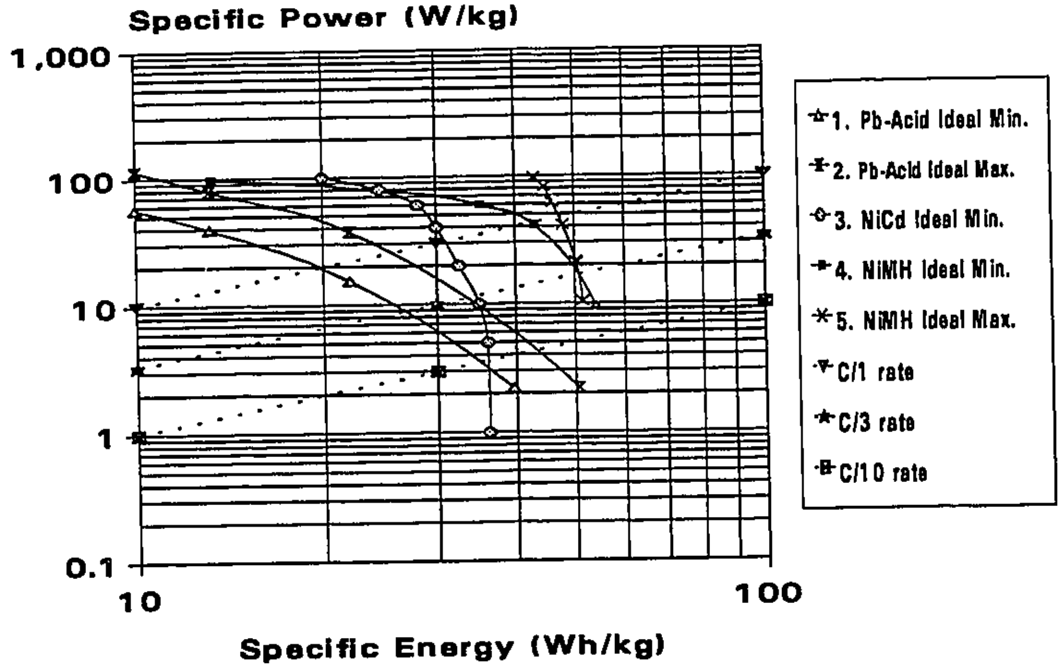

Fig. 7.5 Ragone Curve - Ideal Energy Systems 1-5

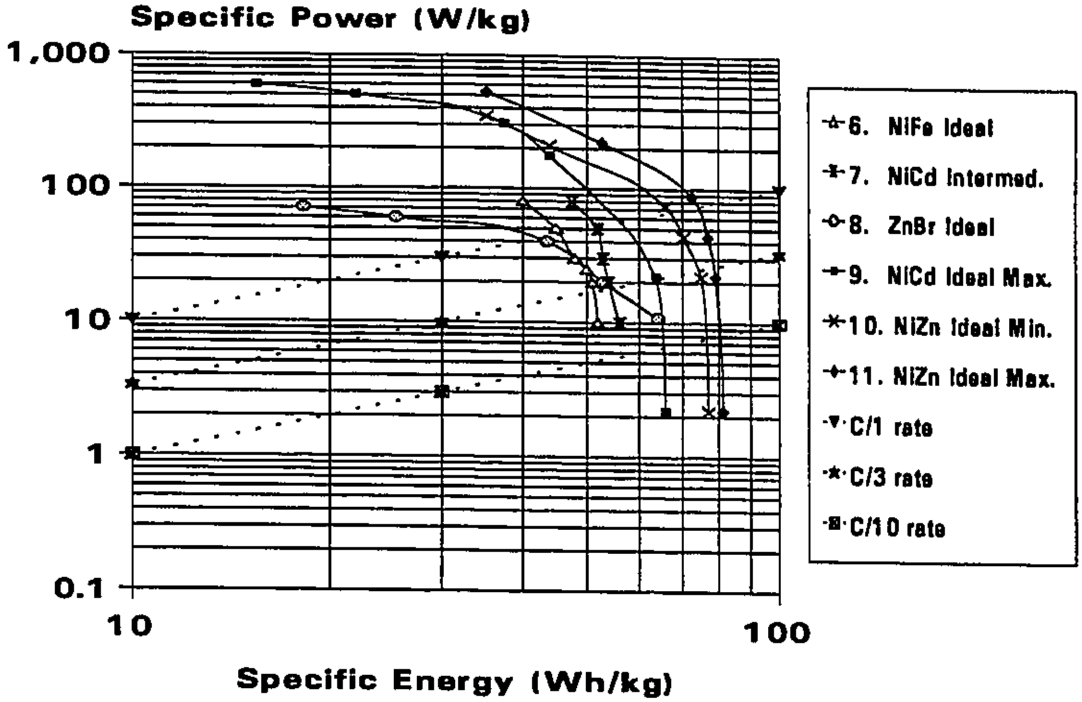

Fig. 7.6 Ragone Curve - Ideal Energy Systems 6-11

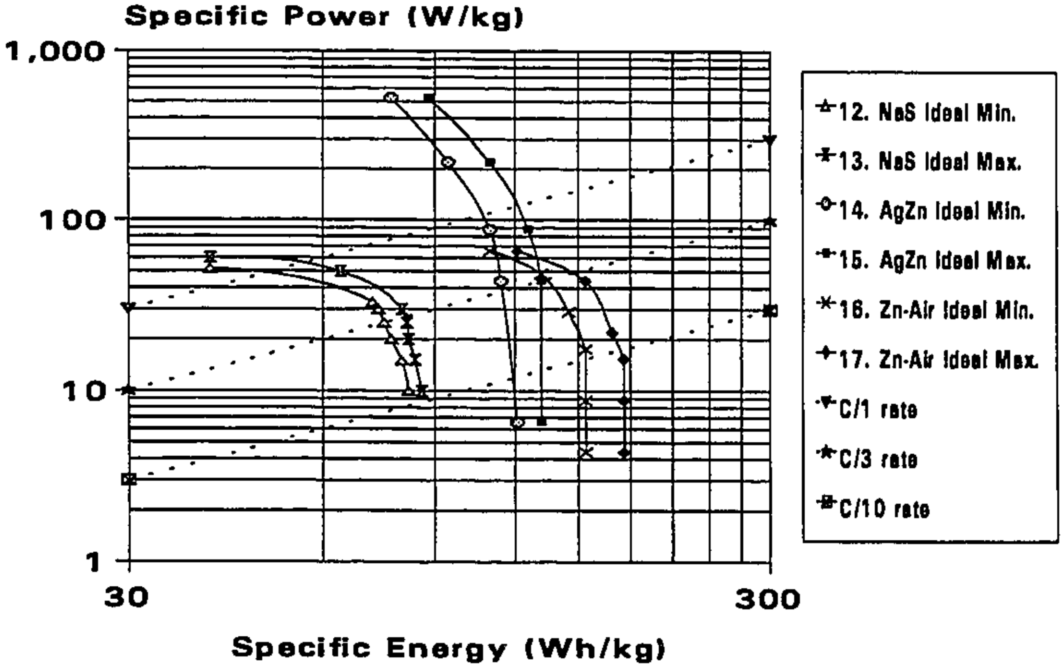

Fig. 7.7 Ragone Curve - Ideal Energy Systems 12-17

The range which the vehicle can reach with a full battery charge can, therefore be obtained from the following two equations:

$$hours = \frac{x_i}{y} \tag{7.20}$$

$$Range = V_{HEV} \cdot hours \tag{7.21}$$

Whereas, the total range the vehicle can travel over the entire cycle life of the energy system is projected as follows:

$$T_{range} = Range \cdot Cycles \tag{7.22}$$

This is under the assumption of 72 km/h constant speed, on a flat surface. The energy available in the battery system is then calculated as follows:

$$kWh_B = \frac{x_i \cdot M_B}{1000} \tag{7.23}$$

The cost of each energy system is calculated based on the C/3 specific energy rate and cost per kWh outlined in Table 7.1.

$$Cost = \frac{S_E\ (C/3)}{1000}\ M_B \cdot \frac{\$}{kWh} \tag{7.24}$$

7.1.3 Experimental Model Validation

In order to predict the behaviour and to optimize the electric drive system, the mathematical model presented above was used to develop a simulation program. The next step was to validate the model by comparing actual experimental results with those obtained by the simulation program. The validation of the vehicle's acceleration time and projected range were considered to be the most important objective, which required validation. The other objectives such as total range, cost and energy, were subsequently dependent on the range, as well as the energy storage system data presented in Table 7.1 and Figs. 7.5, 7.6 and 7.7; therefore they were not validated without any loss of generality.

The HEV was initially designed with a 144 V nominal operating system and an energy storage system consisting of 12 RV31 Eastern-Penn lead-acid batteries. A good correlation between the experimental and simulated acceleration time was established and is illustrated in Fig. 7.8. In terms of range, the simulation projected 74.6 km on a flat surface, when travelling at a speed of 72 km/h, whereas during experimental tests a range of 71.2 km was obtained. However, it should be noted that the road surface on the test track had several banks (leading to a small increase in power consumption), which could account for this deviation of 4.8%.

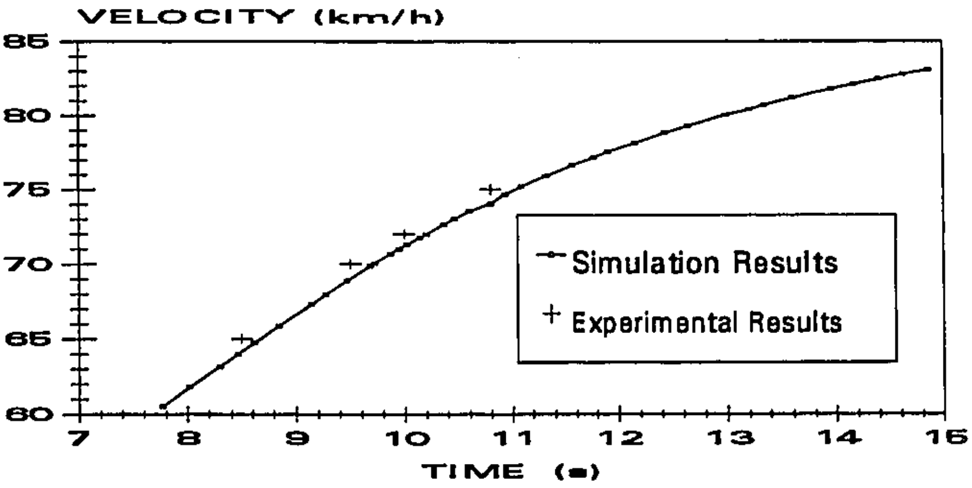

Fig. 7.8 Acceleration Time Versus HEV Velocity

7.2 Optimization Analysis

In order to perform an optimization procedure, the feasible region of the entire system must be defined, by reasonably selecting design constraints. In this research, the lower and upper limits, that define the constraints for the electric drive system optimization process, are represented in equations (7.25) through (7.28), along with nominal values for each design parameters.

Battery Mass:

$$275\,kg \le M_B \le 425\,kg \;;\quad M_{Bn} - 350kg \tag{7.25}$$

Electric drive final gear ratio:

$$1.0 \le N_g \le 3.1 \;;\quad N_{gn} - 2.04 \tag{7.26}$$

Operating voltage of the electric drive system:

$$96\,Volts \le V_{OS} \le 168\,Volts \;;\quad V_{OSn} - 132\,Volts \tag{7.27}$$

Energy density of the storage system (C/3 basis):

$$27\,\frac{Wh}{kg} \le S_E \le 161\,\frac{Wh}{kg} \;;\quad S_{En} - 33\,\frac{Wh}{kg} \tag{7.28}$$

The nominal design parameters and these design constraints were utilized to performed a design parameter study, which essentially outlines the sensitivity of the engineering system. This aids the designer in establishing the initial guess and the weighting factors of the multi-objective optimization.

7.2.1 Design Parameter Analysis

In order to better understand the engineering system which is being analyzed, a design parameter analysis was initially performed with the aid of the established simulation. By varying the design parameters within the constraints formulated previously, their impact on the objective functions could be investigated.

Each objective function was obtained by varying one design parameter, while holding the remaining nominal values constant. The energy storage system was the first design parameter which was varied. The results are represented graphically in Figs. 7.9, 7.10, and 7.11. In the design parameter analysis, the numbers 1 to 17 are used to refer to the energy storage system and their respective energy density (C/3 basis) outlined in Table 7.1.

It can be clearly seen that the only energy systems which have a fast acceleration time and relatively low cost, as energy storage system is varied, are 1, 2, 3, 4, 5, 8, 12, and 13. As the energy storage system is varied from 1 to 17, the energy and cost of each system increases. With reference to Fig. 7.11, the longest range (on a full charge basis) is obtained by the silver-zinc and zinc-air battery systems (14 to 17). However, in terms of total obtainable range, the silver-zinc only surpasses the lead-acid ideal minimum system (1), while the zinc-air surpasses the following energy storage systems: 1, 2, 3, 4, 5, 8, 14, and 15. This is due to the low inherent cycle life of silver-zinc and zinc-air battery systems.

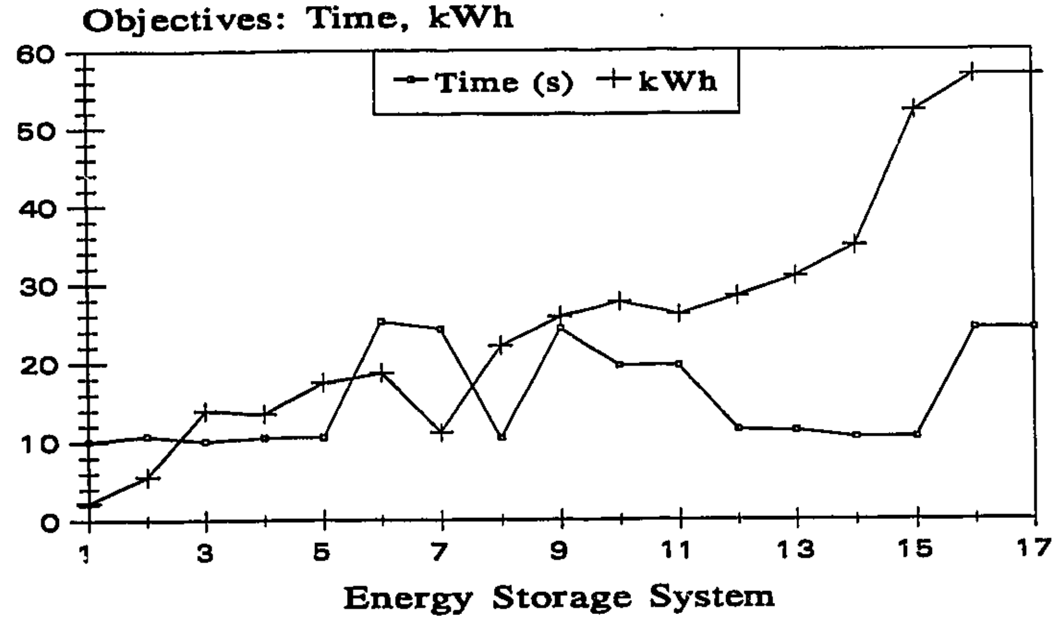

Fig. 7.9 Acceleration Time and kWh Versus Energy Storage System

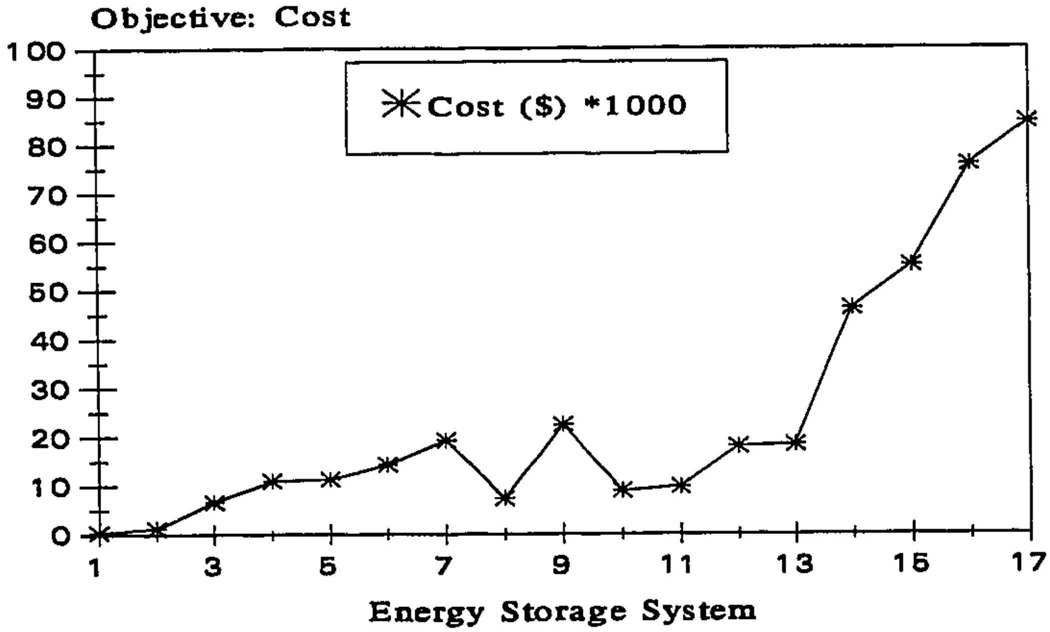

Fig. 7.10 Cost Versus Energy Storage System

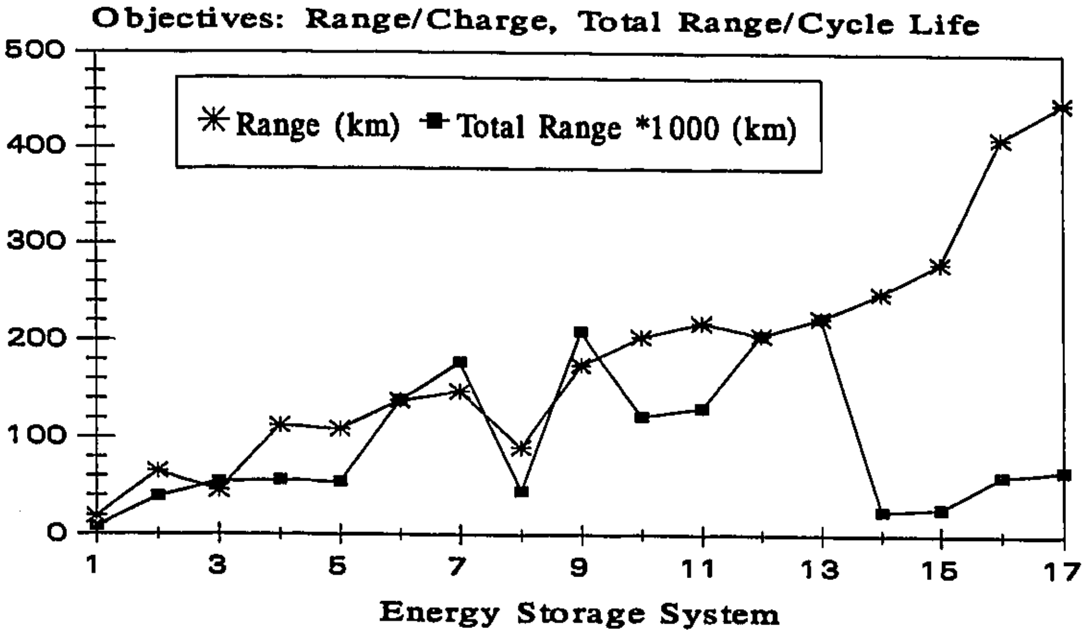

Fig. 7.11 Range and Total Range Versus Energy Storage System

As the battery mass is varied, the effects of all the objectives are represented in Figs. 7.12, 7.13, and 7.14. The energy, cost, range and total range increase in a linear fashion as the battery mass is varied from 275 to 425 kg. In order to obtain realistic results for acceleration, the voltage must be monitored and initially adjusted from the nominal value. This is due to the fact that at 275 kg the nominal operating voltage of 132 V for the ideal maximum lead-acid battery system, is unobtainable at such a small battery mass. Therefore, it is adjusted to adhere to the voltage to mass ratio outlined in Table 7.1. Once the battery mass reaches 322 kg, the nominal value of voltage is held constant at 132 V. Thereafter a slight increase in acceleration time occurs as the battery mass is increased.

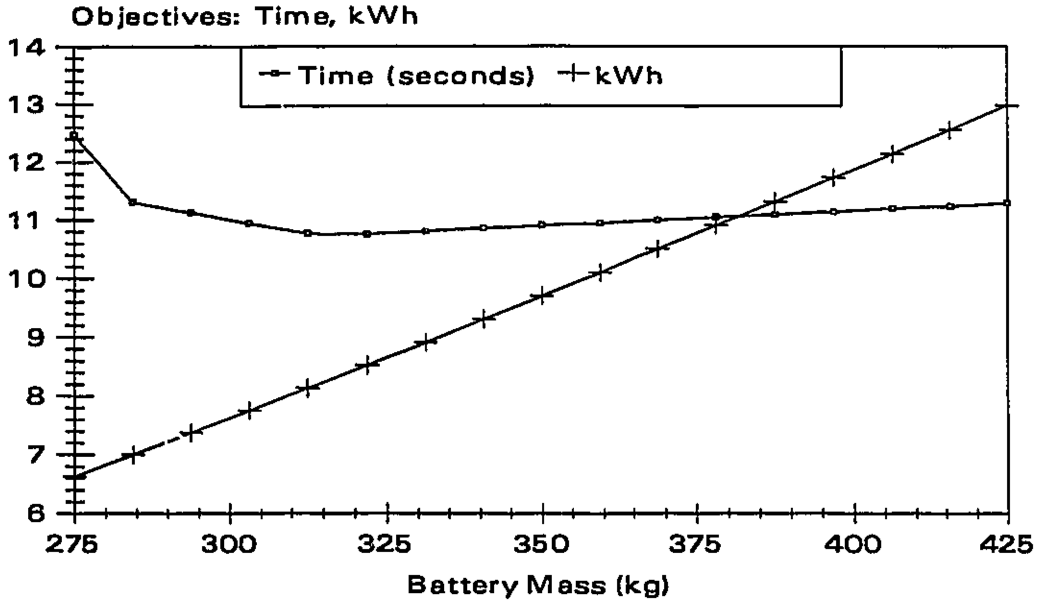

Fig. 7.12 Acceleration Time and kWh Versus Battery Mass

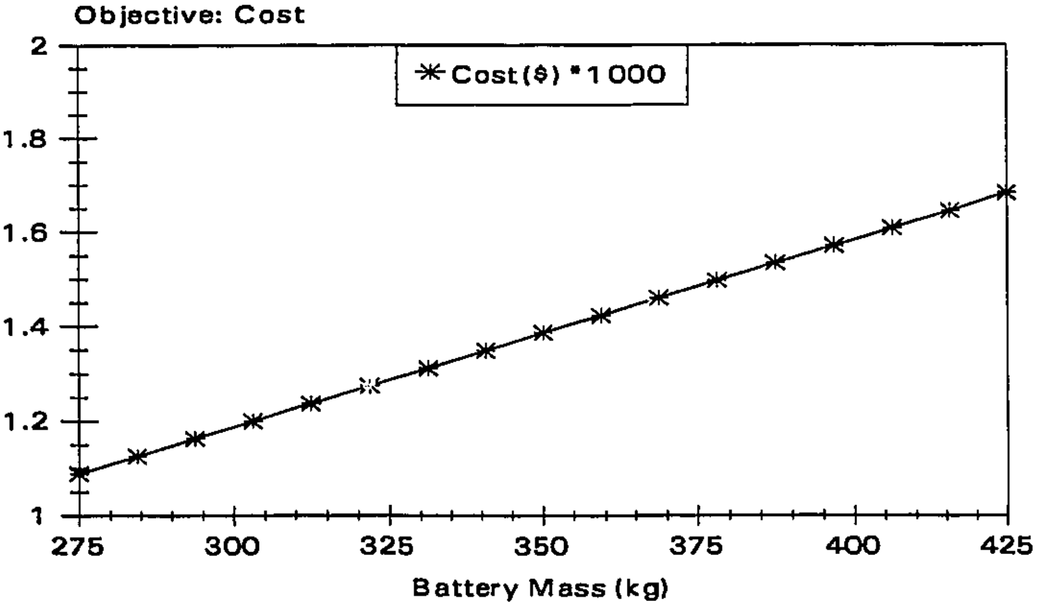

Fig. 7.13 Cost Versus Battery Mass

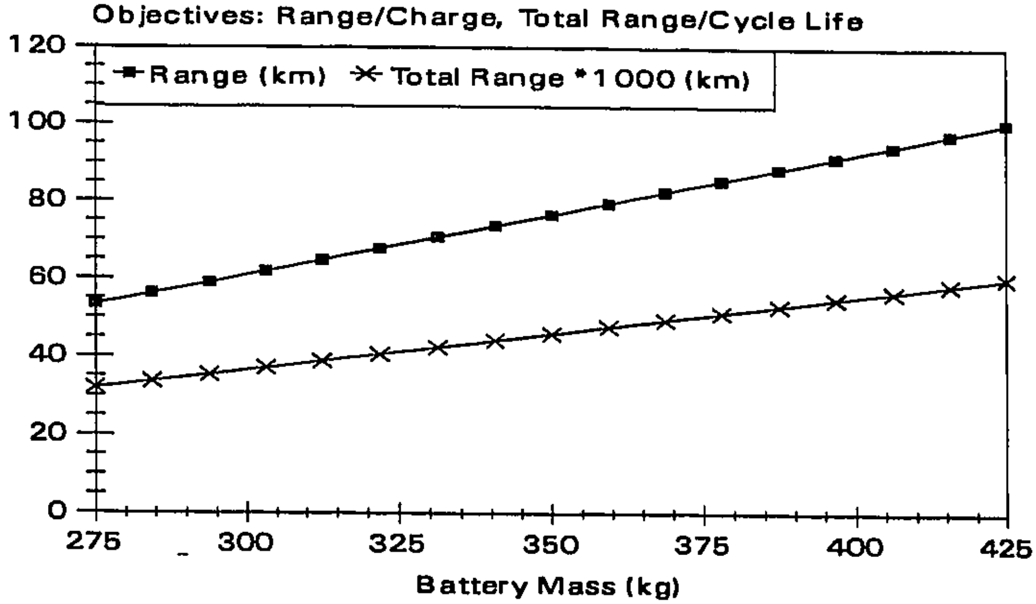

Fig. 7.14 Range and Total Range Versus Battery Mass

The electric drive final gear ratio has one distinct effect on the acceleration time, producing a global minimum within the feasible region at 2.05 (See Fig. 7.15).

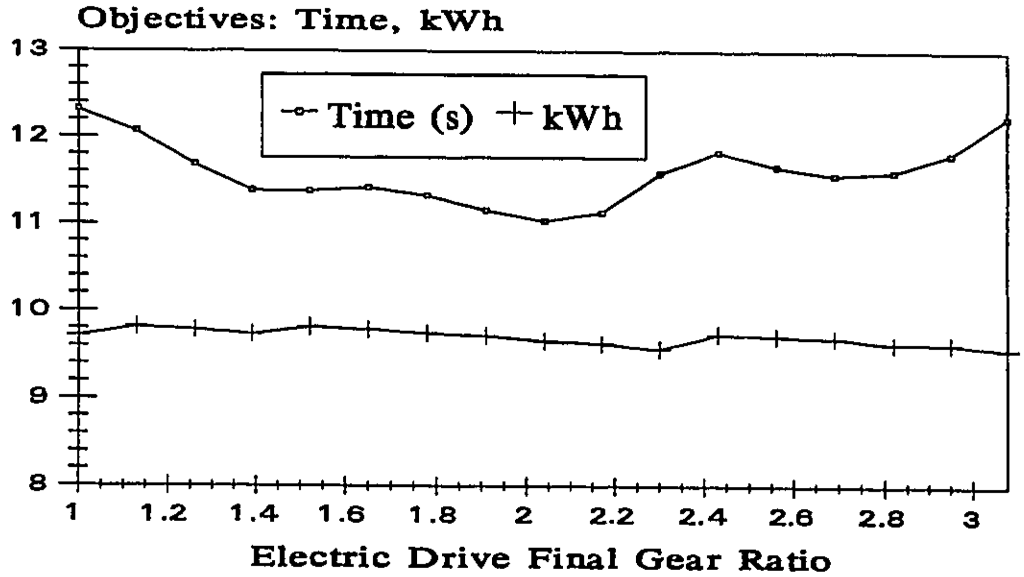

Fig. 7.15 Acceleration Time and kWh Versus Electric Drive Final Gear Ratio

As voltage is varied, a saturation region occurs, which is created by the voltage to mass ratio outlined in Table 7.1. In order to obey the pre-specified nominal value of battery mass, the voltage effect is limited to 147 volts (See Figs. 7.16 and 7.17).

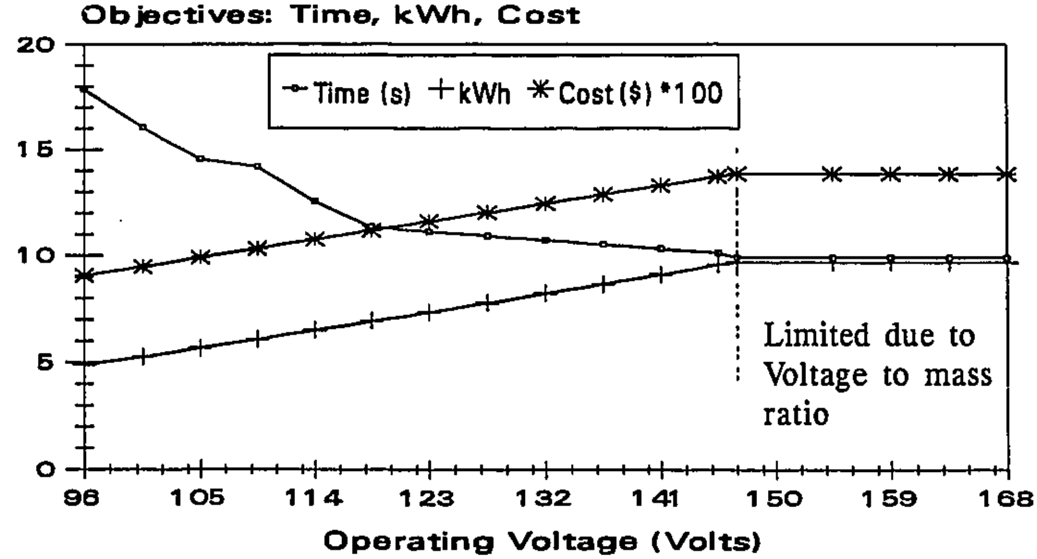

Fig. 7.16 Acceleration Time, kWh and Cost Versus Operating Voltage

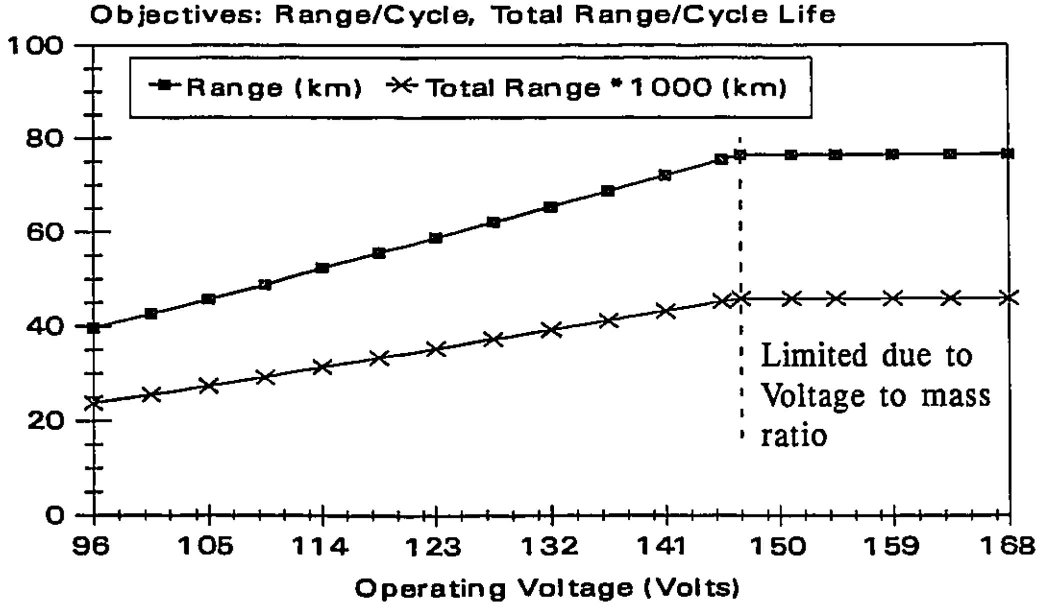

Fig. 7.17 Range and Total Range Versus Operating Voltage

With this complex optimization procedure, the graphical method of optimization becomes very time consuming because the nominal value selected for the energy storage system does not represent the general trend of the other system, due to the fact that they are represented by nonlinear functions. However, a solution can be obtained at the expense of time by progressively changing the nominal value of the energy storage system and repeating the above procedure. A more appropriate solution method for such a system is a multi-objective optimization procedure.

7.2.3 Multi-Objective Optimization

A multi-objective function was constructed in order to solve this optimization problem. The normalized multi-objective function is formulated as:

$$F(x) = [\frac{T(x)-Tmn}{Tmx-Tmn}]^2 + [\frac{C(x)-Cmn}{Cmx-Cmn}]^2 + [\frac{K(x)-Kmn}{Kmx-Kmn}]^2 + [\frac{R(x)-Rmn}{Rmx-Rmn}]^2 + [\frac{TR(x)-TRmn}{TRmx-TRmn}]^2 \qquad (7.29)$$

Having established the multi-objective function, the designer can then place more emphasis on certain objectives which are of more importance in the development of the electric drive system. This is accomplished by choosing five weighting values w_1, w_2, w_3, w_4 and w_5 and applying them in equation 7.29.

The global criterion function can be rewritten as:

$$F(x) = w_1[\frac{T(x)-Tmn}{Tmx-Tmn}]^2+w_2[\frac{C(x)-Cmn}{Cmx-Cmn}]^2+$$

$$w_3[\frac{K(x)-Kmn}{Kmx-Kmn}]^2+w_4[\frac{R(x)-Rmn}{Rmx-Rmn}]^2+$$

$$w_5[\frac{TR(x)-TRmn}{TRmx-TRmn}]^2 \tag{7.30}$$

The objective function in equation (7.30) together with the design constraints in equations (7.25) to (7.28) are solved using an interior penalty function method.

The pseudo-objective function is defined as:

$$\phi(X) = F(X) - p_p\sum_{i=1}^{m} \frac{1}{g_i(X)} \tag{7.31}$$

where $g_i(X)$ represents the inequality constraints outlined previously and p_p is the penalty parameter whose initial value is selected as:

$$p_p = \frac{F(X_1)}{-\sum_{i=1}^{m} \frac{1}{g_i(X_1)}} \tag{7.32}$$

and thereafter decremented. Minimization of the pseudo function is obtained by using the Hooke and Jeeves method [39] and [40].

The weighting factors (w_i's): 0.3, 0.5, 0.1, 0.05, and 0.05 were used on the global objective function. In return, the following design parameters were obtained when the pseudo-objective function was minimized using Hooke and Jeeves method:

- Battery mass: $M_B = 400$ kg,
- Electric drive final gear ratio: $N_g = 2.05$,
- Nominal operating voltage: $V_{OS} = 168$ V,
- Specific energy density of the storage system: $S_E = 33$ Wh/kg.

In this research the proposed weighting scheme places the emphasis on acceleration time and cost of the energy system, however these weighting factors can be changed in order to suit the designers needs. The calculated optimal design parameters were used as inputs for the simulation previously outlined. The anticipated performance of the vehicle is as follows:

- 9.31 seconds (0 to 72 km/h),
- 1600 $ battery pack cost,
- 11.9 kWh battery pack energy,
- 93 km range (full charge basis) travelling at 72 km/h on a flat surface, and
- 55 900 km obtainable range from the energy storage system during its entire life.

7.3 Summary

The effects of design parameters on the performance of an electric vehicle were presented. A detailed mathematical model was established using governing vehicle dynamics equations. Ideal energy storage systems were modelled with high order polynomial equations and represented graphically in the form of Ragone curves. This was followed by the development of a simulation program which was utilized to optimize the design parameters, such as specific energy and mass of the storage system, electric motor operating voltage and electric drive final gear ratio. The effects, these parameters had on the objective functions, namely range, acceleration, specific consumption, battery cycle life and cost, were investigated. Thereafter a detailed multi-parameter optimization using nonlinear programming techniques was carried out. The simulation and optimization results for the proposed weighting scheme on the global criterion function and design constraints, which would yield the optimal electric drive system for the vehicle in question, were also presented.

8. HYBRID MODE ANALYSIS

The main objective of this chapter is to analyze and consequently optimize the series mode of operation. An experimental investigation was first performed in order to quantitatively formulate the effects which the design parameters have on the objective functions. Thereafter, a sensitivity analysis was performed, followed by a multi-objective optimization using the Hooke and Jeeves method. After obtaining the optimal design parameters for the series mode of operation, the value of the sprocket ratio for the parallel mode of operation was established.

8.1 Series Mode Experimental Investigation

Experiments were performed with the series mode of operation in order to establish the relationship between the design parameters, namely engine speed, as well as the carburettors' idle mixture setting, and the following objective functions: net alternator power, fuel consumption, and exhaust gas emissions, such as NOx, CO, and HC. The test set-up consisted of a NOVA 7550P5B exhaust gas analyzer, a FLOSSCAN 201B-18 flow meter, a DYNAPAR 54Z digital speed sensor, and a data acquisition unit. In order to create a load for the alternator, the batteries were discharged to 60% DOD. This was deemed to be the most effective method of loading the alternator for it represented the actual condition under which the alternator would function during the competition. In this context, the net power of the alternator corresponds to, the obtainable charging power after the rectifier bridge. The concentrations of the exhaust gas emissions were measured after the three way catalytic converter. Fig. 8.1 illustrates the test set-up utilized to perform the experiments with the series mode of operation. The instrumentation specifications and calibration curve of the flow meter are presented in the Appendix 2.

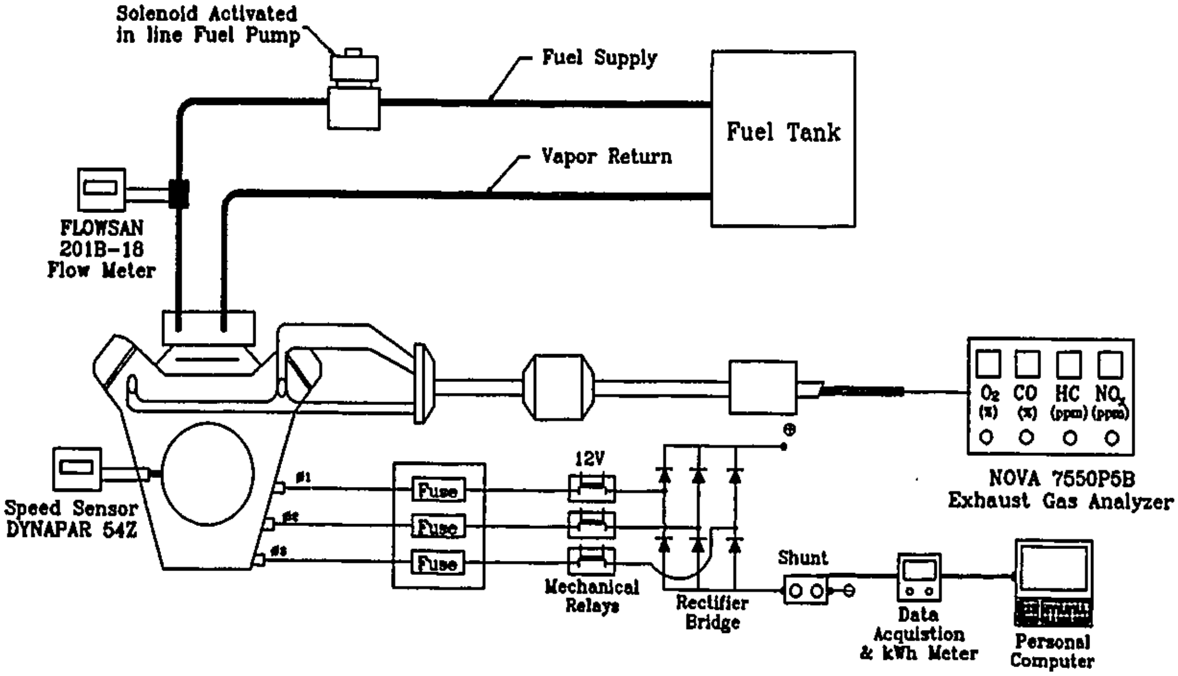

Fig. 8.1 Test Set-Up Series Mode of Operation

The two design parameters of key interest were the speed governor lever position and the idle mixture setting, represented in terms of engine speed (rpm) and counter clockwise (ccw) idle screw rotational position (degree), respectively. The engine speed was varied from 2800 rpm up to 3600 rpm, while the idle mixture setting was held constant at a nominal screw position of 720° (ccw). Thereafter, the idle fuel mixture screw position was varied from 0° to 1350°

(ccw), while the engine speed was held constant at a nominal value of 3150 rpm. The experimental results are graphically represented in Figs. 8.2, 8.3, 8.4 and 8.5. The results obtained when the idle mixture was held constant at a nominal screw position of 720° (ccw) and the engine speed was varied from 2800 to 3600 rpm, are shown in Figs. 8.2 and 8.3.

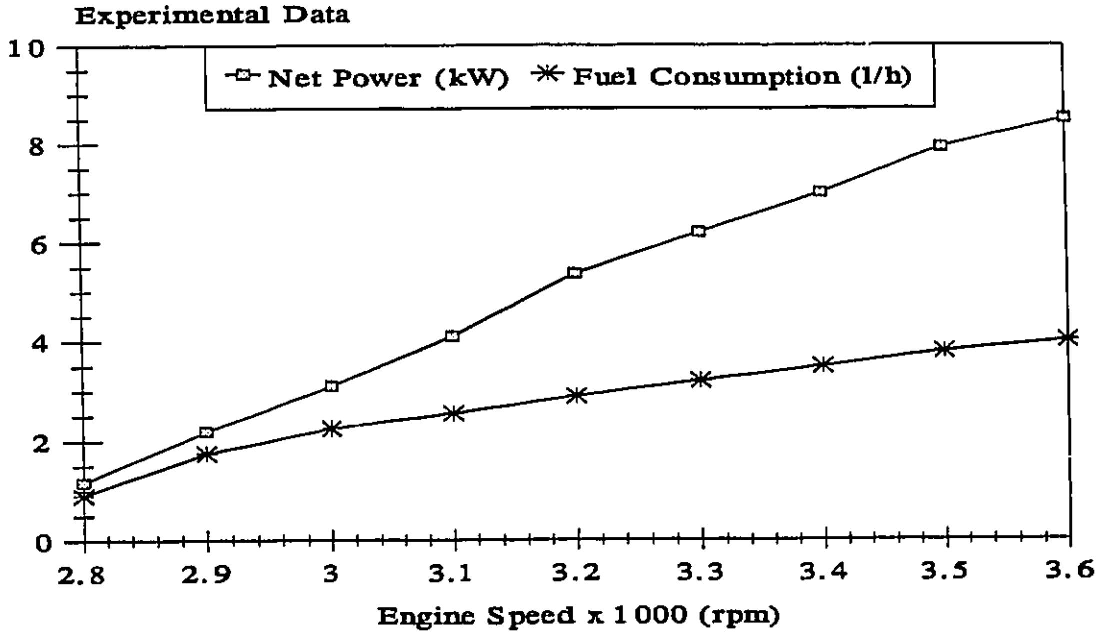

Fig. 8.2 Power and Fuel Consumption Versus Engine Speed

The design specifications of the alternator, outlined to Fisher Electric Motor Technology (See Section 5.2.1), were not respected, as the alternator unit provided less than 0.2 kW at an operating speed of 2700 rpm, instead of 9 kW. Therefore, the engine speed design constraints had to be modified in order to assure that the net power of the alternator obtained by the optimization procedure would be between 6 and 9 kW.

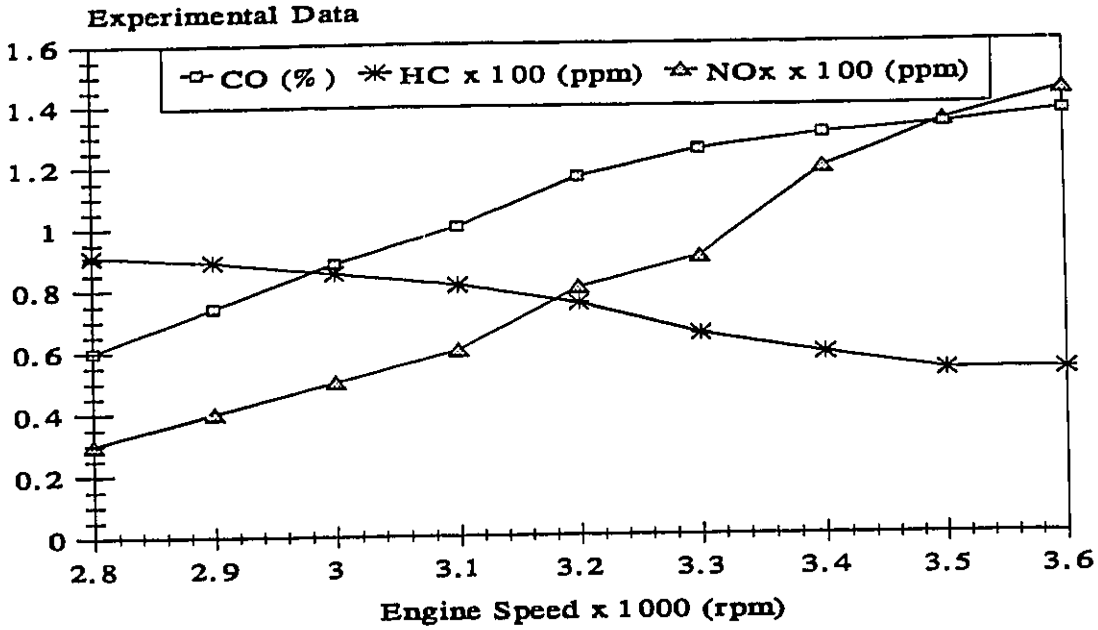

Fig. 8.3 Exhaust Gas Emissions Versus Engine Speed

The results obtained when the speed was held constant at a nominal value of 3155 rpm and the idle mixture screw setting was varied from 0° to 1350°, are shown in Figs. 8.4 and 8.5.

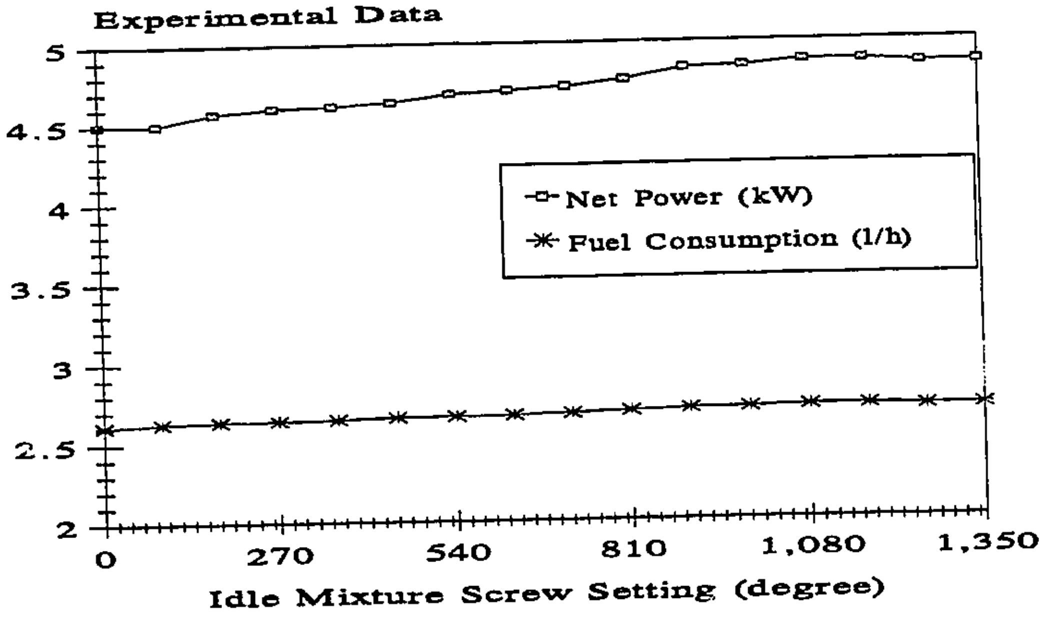

Fig. 8.4 Power and Fuel Consumption Versus Idle Mixture Screw Setting

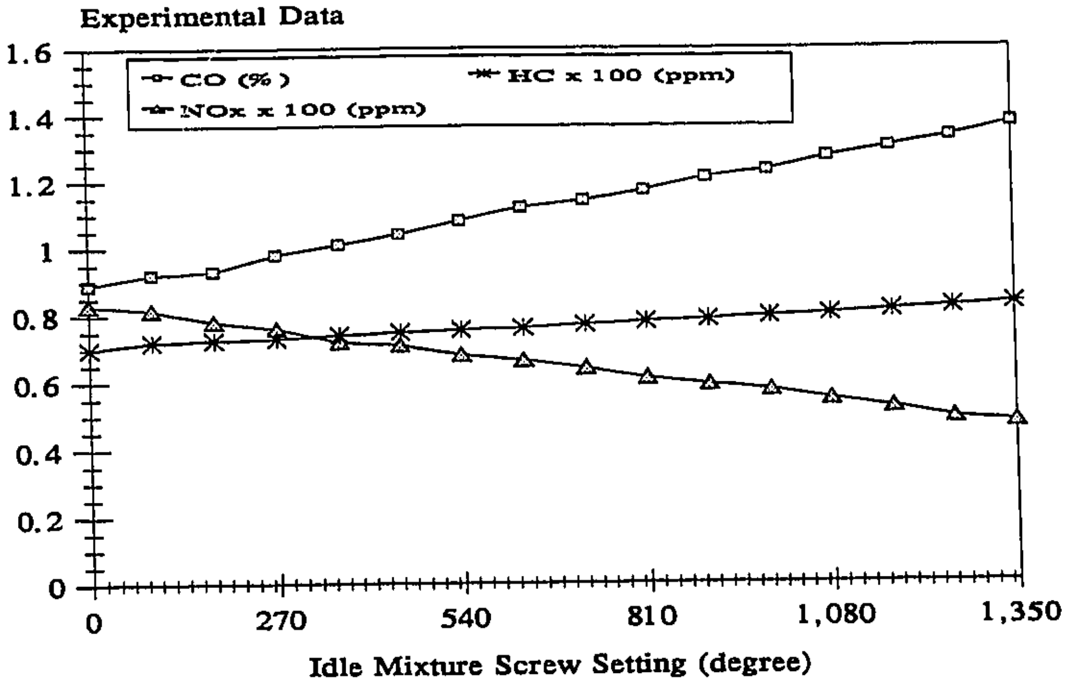

Fig. 8.5 Exhaust Gas Emissions Versus Idle Mixture Screw Setting

Several tests were performed in this manner with different nominal values for engine speed and idle mixture setting, in order to properly analyze the complete spectrum of the series mode design criteria. Without any loss of generality the experimental results were used to formulate objective functions using multi-parameter regression analysis. The objective functions obtained through the regression analysis are as follows:

- Net Power (kW) Objective Function (PN)

$$PN = -2.510\times10^{1} + (9.384\times10^{-3})\cdot\omega_{ICE} + (2.630\times10^{-4})\cdot IM \tag{8.1}$$

- Fuel Consumption (ℓ/h) Objective Function (FC)

$$FC = -8.505 + (3.523 \times 10^{-3}) \cdot \omega_{ICE} + (6.378 \times 10^{-5}) \cdot IM \qquad (8.2)$$

- CO Exhaust Gas Emissions (%) Objective Function (COE)

$$COE = -2.213 + (9.741 \times 10^{-4}) \cdot \omega_{ICE} + (3.378 \times 10^{-4}) \cdot IM \qquad (8.3)$$

- HC Exhaust Gas Emissions (ppm) Objective Function (HCE)

$$HCE = 2.512 \times 10^{2} - (5.732 \times 10^{-2}) \cdot \omega_{ICE} + (8.142 \times 10^{-3}) \cdot IM \qquad (8.4)$$

- NOx Exhaust Gas Emission (ppm) Objective Function (NOE)

$$NOE = -3.228 \times 10^{2} + (1.304 \times 10^{-1}) \cdot \omega_{ICE} - (2.495 \times 10^{-2}) \cdot IM \qquad (8.5)$$

where:

ω_{ICE} - Speed of the ICE (rpm)

IM - Idle mixture screw setting (ccw) rotational position (degree)

8.1.1 Sensitivity Analysis

A 3-dimensional sensitivity analysis was performed in order to visualize the map of the objective functions with respect to the design parameters. The design parameters were represented on the x and y axes of the graphs, while the various objective functions were mapped on the z axis. Figs. 8.6, 8.7, 8.8, 8.9 and 8.10 illustrate the 3-dimensional maps of the objective functions versus both design parameters, engine speed and idle mixture fuel setting.

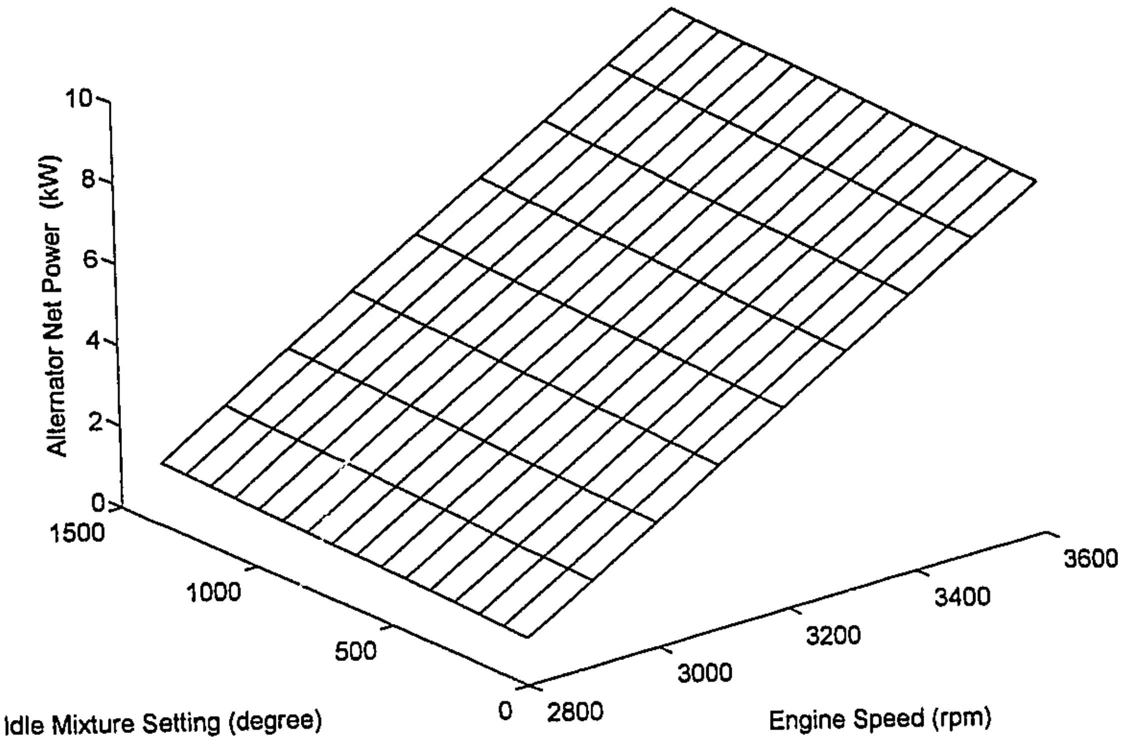

Fig. 8.6 Net Power Versus Idle Mixture Setting and Engine Speed

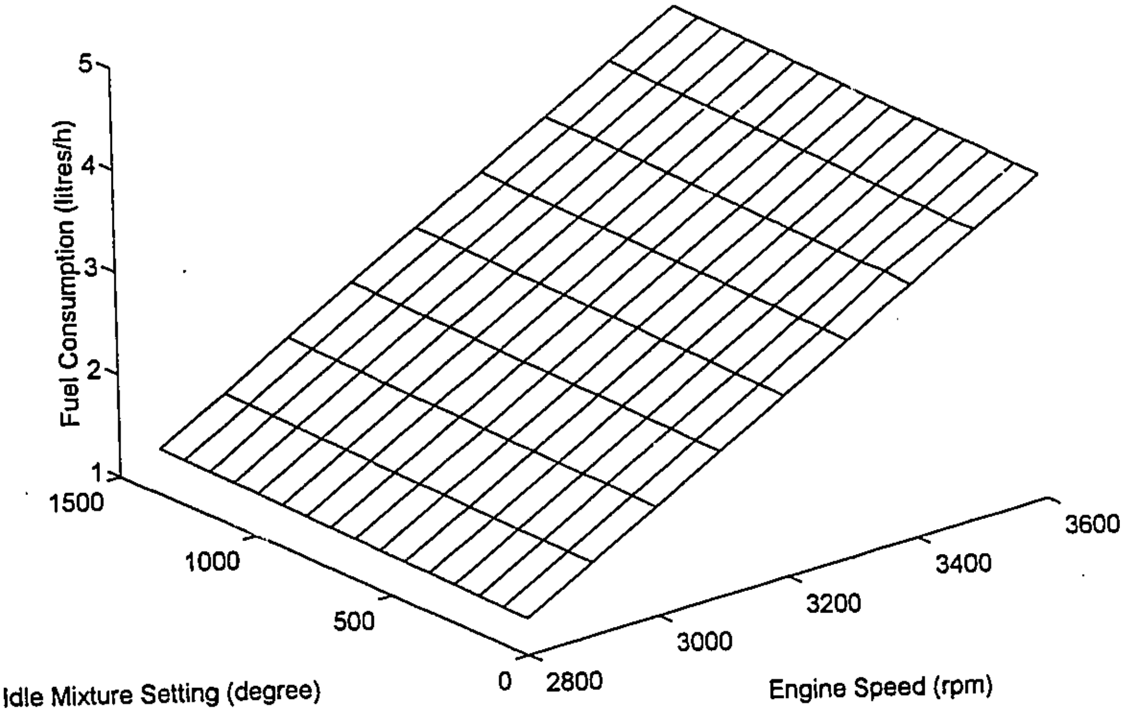

Fig. 8.7 Fuel Consumption Versus Idle Mixture Setting and Engine Speed

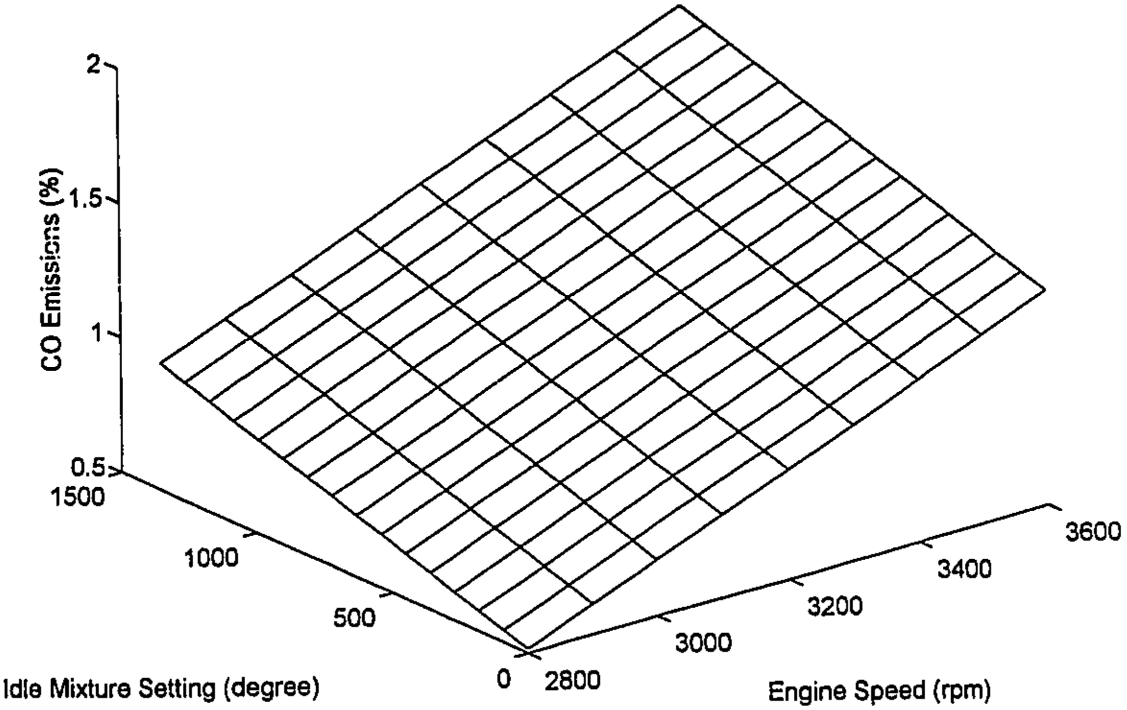

Fig. 8.8 CO Exhaust Gas Emissions Versus Idle Mixture Setting and Engine Speed

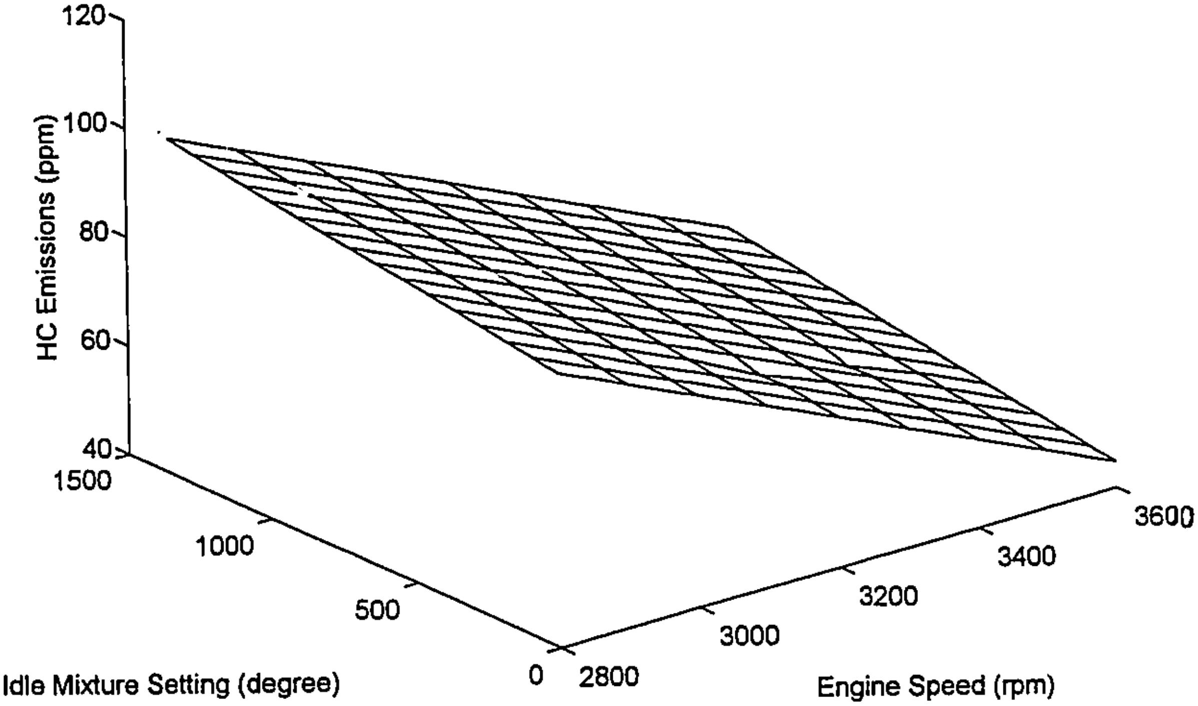

Fig. 8.9 HC Exhaust Gas Emissions Versus Idle Mixture Setting and Engine Speed

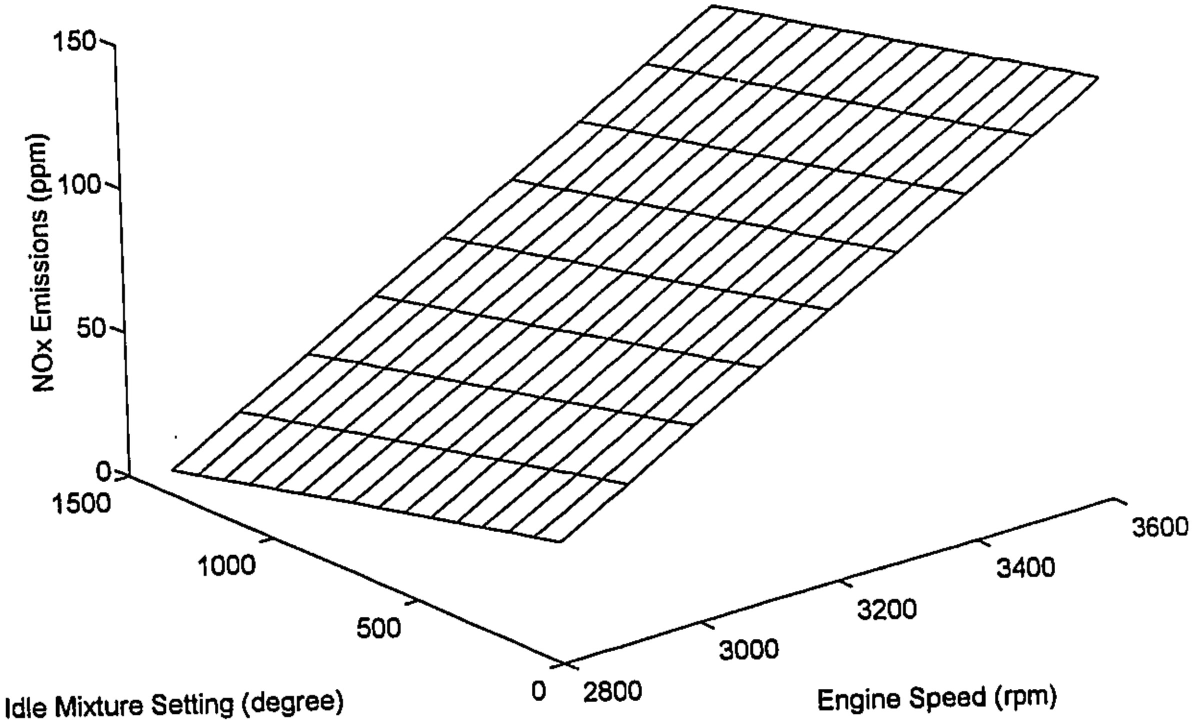

Fig. 8.10 NOx Exhaust Gas Emissions Versus Idle Mixture Setting and Engine Speed

8.2 Series Mode Multi-Objective Optimization

After investigating the sensitivity of the system, a multi-objective function was constructed in order to analytically solve this optimization problem. The lower and upper limits of the design parameters, which were used to formulate the design constraints of the optimization procedure are as follows:

$$3300 rpm \leq \omega_{ICE} \leq 3600 rpm \tag{8.6}$$

$$180° \leq IM \leq 1350° \tag{8.7}$$

The normalized multi-objective function formulated for the series mode optimization is outlined as:

$$F(x) = [\frac{PN(x)-PNmn}{PNmx-PNmn}]^2+[\frac{FC(x)-FCmn}{FCmx-FCmn}]^2+$$

$$[\frac{COE(x)-COEmn}{COEmx-COEmn}]^2+[\frac{HC(x)-HCmn}{HCmx-HCmn}]^2+$$

$$[\frac{NOE(x)-NOEmn}{NOEmx-NOEmn}]^2 \qquad (8.8)$$

Having established the multi-objective function, five weighting values w_1, w_2, w_3, w_4 and w_5 are applied in equation (8.8). Consequently, the global criterion function is rewritten as:

$$F(x) = w_1[\frac{PN(x)-PNmn}{PNmx-PNmn}]^2+w_2[\frac{FC(x)-FCmn}{FCmx-FCmn}]^2+$$

$$w_3[\frac{COE(x)-COEmn}{COEmx-COEmn}]^2+w_4[\frac{HCE(x)-HCEmn}{HCEmx-HCEmn}]^2+$$

$$w_5[\frac{NOE(x)-NOEmn}{NOEmx-NOEmn}]^2 \qquad (8.9)$$

An interior penalty function method was used to solve the objective function in equation (8.9) together with the design constraints in equation (8.6) and (8.7). A similar pseudo-objective function and penalty parameter were formulated as in

Chapter 7 (See equation (7.31) and (7.32), respectively). The minimization of the series mode pseudo function is obtained using the Hooke and Jeeves method. The weighting factors (w_i's): 0.05, 0.05, 0.05, 0.425, and 0.425 were used on the global objective function. In return, the pseudo-objective function obtained the following optimal design parameters:

- ω_{ICE} = 3460 rpm
- IM = 816° (ccw)

The iteration history of the design parameters, obtained during the series mode optimization procedure, is outlined in Fig. 8.11.

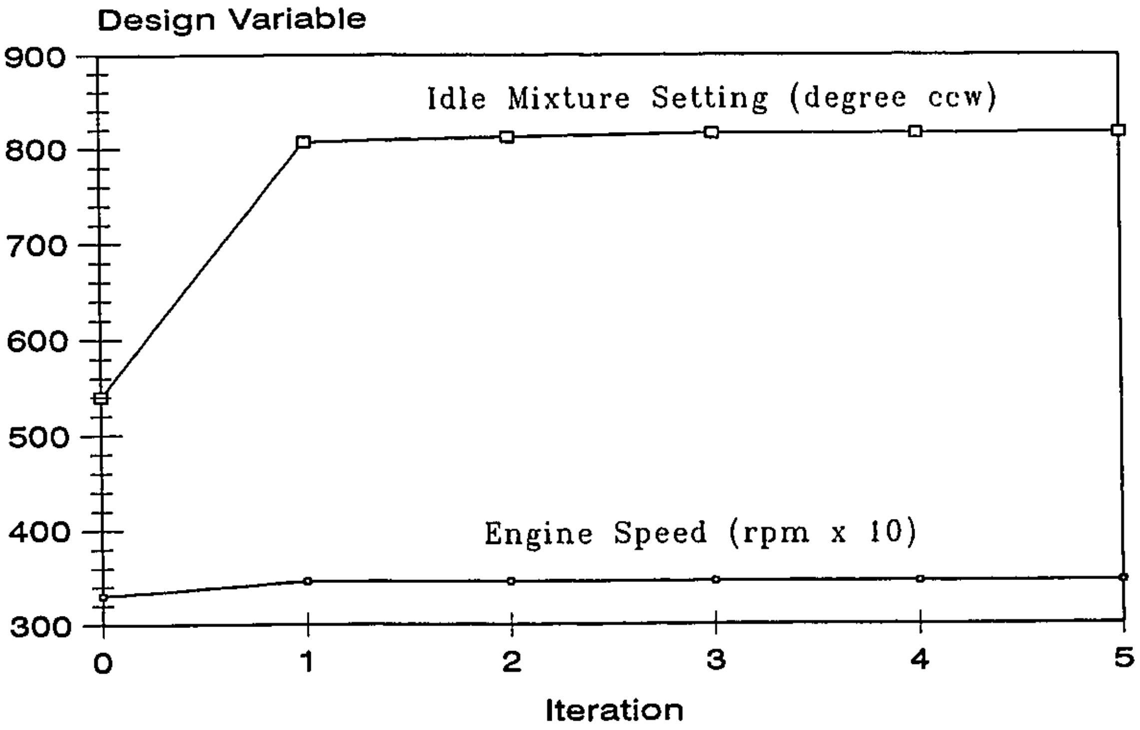

Fig. 8.11 Iteration History of the Design Variables

An alternative graphical optimization method was established by constructing a computer program, which effectively analyzed the design parameters with respect to the global criterion function outlined in equation (8.9) and with the proposed weighting values. The computer program increased the idle screw setting by a sample interval of 45°, and thereafter varied the entire range of the engine speed. The effect this had on the normalized multi-objective function was closely monitored, and thereafter graphically illustrated in a 3-dimensional map, which is outlined in Fig. 8.12.

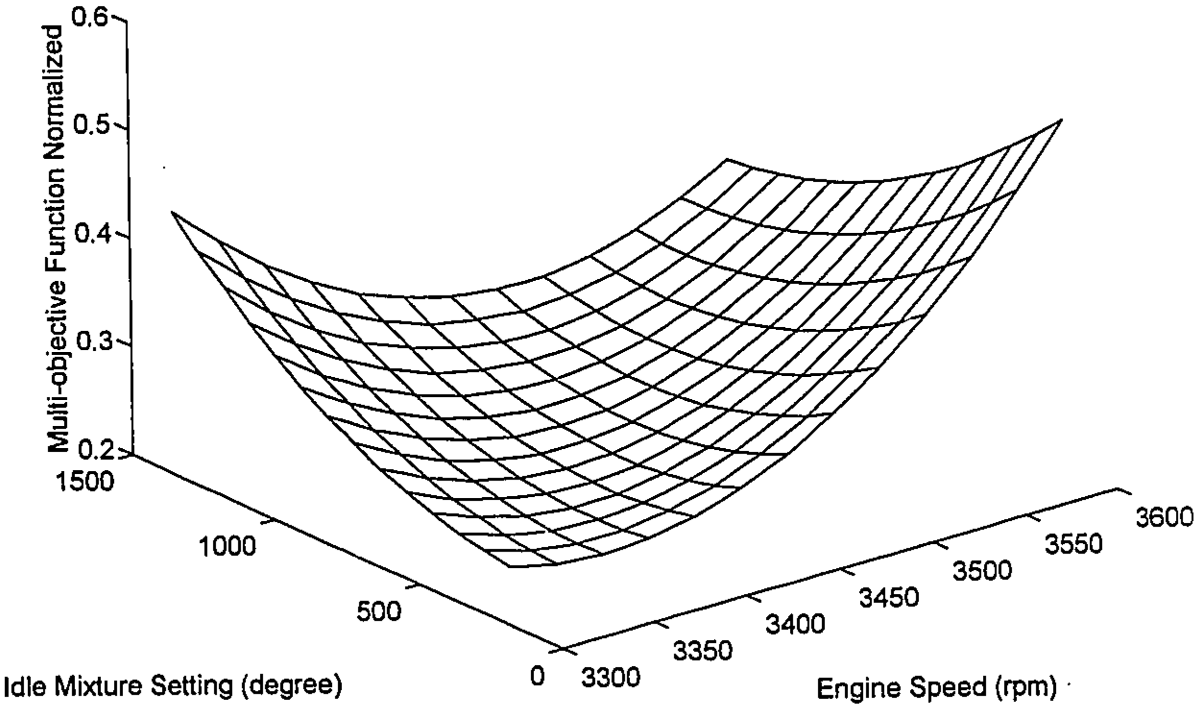

Fig. 8.12 Normalized Multi-Objective Function Versus Engine Speed and Idle Mixture Setting

Since, this analysis involved two design parameters, the 3-dimensional graphical optimization obtained the same results as Hooke and Jeeves method. When a multi-objective optimization would involve more than two design parameters, it could become very difficult to predict the optimal design parameters with a graphical optimization procedure.

The calculated optimal design parameters were used as inputs for the objective functions formulated by the linear regression analysis. Thereafter, the anticipated performance of the series mode of operation was predicted with the aid of equations (8.1) to (8.5). Alternatively, the internal combustion engine was tuned using the optimal design parameters and, thereafter, the fuel consumption, net power, and emissions were tested. The results obtained with the optimal design parameters through the formulated linear regression objective functions and the testing, is outlined in Table 8.1. The good correlation of the calculated and experimental results assured that the objective functions of the experimental optimization were well represented by the linear regression analysis.

Table 8.1 Calculated and Actual Test Performance - Series Mode of Operation

Objective	Calculated Results (Linear Regression)	Test Results	% Difference
Net Power (kW)	7.58	7.52	0.80
Fuel Consumption (litres/h)	3.74	3.71	0.81
CO Exhaust Gas Emissions (%)	1.43	1.38	3.62
HC Exhaust Gas Emissions (ppm)	59	58	1.72
NOx Exhaust Gas Emissions (ppm)	108	112	3.70

8.3 Parallel Mode Analysis

Having established the operating conditions of the engine, in series mode of operation, the sprocket ratio of the parallel mode could be found. The objective of the parallel mode of operation was to maintain the vehicle speed at 72 km/h in 4th gear. The sprocket ratio of the parallel mode of operation consisted of the sprocket installed on the electro-magnetic clutch and that installed on the ICE shaft (See Figs. 5.10 and 5.11, respectively). In order to ensure that the HEV would obtain 72 km/h the following sprocket ratio was required:

$$N_{sp} = \frac{\omega_{ICE} \cdot r}{V_{HEV} \cdot N_f \cdot N_{g4}} = 1.474 \qquad (8.11)$$

where:

N_{sp} - Parallel mode sprocket ratio

ω_{ICE} - Optimal engine speed (362.3 rads/s)

V_{HEV} - Velocity of HEV (20.1 m/s)

N_f - Final gear ratio (3.619)

N_{g4} - 4th gear ratio (0.972)

8.4 Summary

An experimental investigation was performed on the series mode of operation, in order to quantitatively formulate the effects the engine speed, and idle mixture screw setting have on the following parameters: net alternator power, fuel consumption, and exhaust gas emissions. The sensitivity of the system was analyzed and presented graphically in three-dimensional maps. A multi-objective function was formulated and solved using Hooke and Jeeves method. Consequently, the optimal design parameters obtained from the optimization were used to tune the ICE. Thereafter, the design of the sprocket ratio of the parallel mode of operation was established.

9. CONCLUSIONS AND RECOMMENDATIONS

The main objectives of this investigation was to experimentally and analytically study and design a parallel-series Hybrid Electric Vehicle.

A mathematical model, Laplace transform technique and TUTSIM computer programming, were used in order to simulate the electric drive system of the hybrid electric vehicle and to analyze the performance of several electric motors matched with a fixed gear ratio configuration and a five speed transaxle configuration.

Two test-set ups were developed, in order to perform constant current and constant power battery testing. By performing constant current testing an effective battery comparison was performed on several lead-acid batteries. Thereafter, the complete energy and power density spectrum of two nickel-cadmium batteries (Saft Nife STM1.130 and Marathon 44SP100) and one lead-acid battery (Eastern-Penn RV31) was investigated experimentally with the established constant power test set-ups. The experimental results of the constant power testings were then compared to analytical results obtained from a modified Universal Battery Model.

A mathematical model was developed to analyze the entire electric drive system, namely the electric motors and energy storage system. The good agreement between the calculated and experimental results provided confidence to use the mathematical model for carrying out a multi-objective optimization on the electric drive system.

Thereafter, an experimental investigation was performed on the series mode of operation. Using multi-regression analysis the experimental results were formulated into objective functions and used to construct a multi-objective procedure for the series mode of operation.

The following conclusions have been drawn from the investigation of a parallel-series configured hybrid electric vehicle:

1) The electric motors equipped with a five speed transaxle were found to outperform similar motors interfaced with a fixed gear ratio configuration. The performance was analyzed in terms of acceleration and overall efficiency of the electric drivetrain. The concept of incorporating a low cost series wound motor as an acceleration helper motor was a very effective means of minimizing the cost to power ratio of the electric drive system, while still maintaining high performance. This was validated in the 1993 Ford HEV Challenge, were the Concordia HEV placed 1st in the electric mode acceleration category and 2nd in the most cost effective performance category.

2) The regenerative braking feature of the Solectria BRLS16 motor was found to be very beneficial, during city driving conditions. The experimental investigation found that approximately 13 % energy recuperation was obtained during city driving. Regarding the parallel-series configuration, the series mode of operation provided low emission outputs due to the engine's fixed speed and load environment, however at the expense of overall efficiency. In parallel mode, the engine was capable of maintaining the vehicle at a speed of 72 km/h in 4th gear.

3) Constant current battery testing was found to be the best means of effectively comparing different battery systems. On the other hand, the constant power testing allowed for the understanding of the complete energy and power

spectrum of a battery system. In the absence of time and resources, an empirical correlation introduced to the Universal Battery Model enabled the prediction of very conservative energy and power density results. On a C/1 basis, the following deviation between the experimental and calculated results were found for the RV31, STM1.130, and 44SP100 battery systems, 6.52%, 12.05%, and 19.3%, respectively.

4) In this research the proposed weighting scheme of the electric drive multi-objective optimization procedure placed the emphasis on acceleration time and cost of the energy storage system. The optimal design parameters for the electric drive system were as follows:

- Battery mass: 400 kg,
- Electric drive final gear ratio: 2.05,
- Nominal operating voltage of: 168V,
- Specific energy density of the storage system: S_E = 33 Wh/kg, which represents an idle maximum lead-acid battery system.

5) The linear regression techniques used in the series mode analysis were very effective in modelling and simulating the experimental results obtained for exhaust gas emissions, fuel consumption, and net alternator power. Thereafter, multi-objective optimization procedure enabled for the proper tuning of the auxiliary power unit, with an effective compromise being established between net alternator power, fuel consumption, and exhaust gas emissions.

Based on the conclusions drawn, the following recommendations are proposed:

1) A different size internal combustion engine, more suitable to perform in an automotive environment, should be introduced to the present design. The engine's power should be obtained based on an optimization procedure, which incorporates engine power as a design variable, and exhaust gas emissions and fuel consumption as objectives.

2) Thereafter, a closed-loop control strategy should be incorporated to the series mode of operation, in order to enable the engine to function in an "on" "off" concept. To elaborate on this issue, in series mode, the engine would be turned "on" and "off" based on the feedback received from a battery state-of-charge indicator and a thermocouple which would measure the temperature of the battery enclosure. This would minimize the deterioration of the battery which occurs due to excess loading from the alternator.

3) A closed-loop fuel delivery system, as well as a stepper motor controlled throttle position which would function exactly as a cruise control unit should be incorporated on the HEV. This will enable the driver to select any desirable driving speed in parallel mode, making the vehicle more practical. Furthermore, the electronic control unit of the fuel delivery system can be used to adjust the engine speed at the appropriate setting, during series mode of operation.

4) A cleaner fuel, such as natural gas could be beneficial from an emissions point of view, if it would be introduced as the alternative energy source.

5) In order to improve the ride and handling quality of the HEV a detailed investigation on the suspension and steering system is also required.

REFERENCES

1. Bedard, P., "Why Alternative Fuels Make No Sense," Car and Driver, Vol. 38, No. 6, December, 1993, pp. 97-105.
2. Unnewehr, L.E., and Nasar, S.A., "Electric Vehicle Technology," John Wiley & Sons, New York, 1982.
3. Shepherd, C.M., "Design of Primary and Secondary Cells, Part II: An Equation Describing Battery Discharge," U.S. Naval Laboratories Report NRL6129, November, 1964.
4. Ragone, D.V., "Review of Battery Systems for Electrically Powered Vehicles," SAE Paper No. 680453, 1968.
5. Unnewehr, L.E., and Knoop, C.K., "Electrical Component Modelling and Sizing for EV Simulation," SAE Paper No. 780215, 1978.
6. Hayden, C.L., "Electric Vehicle Battery Management," SAE Paper No. 810417, 1981.
7. McNicol, B.D., and Rand, D.A.J., "Power Sources for Electric Vehicles," Elselvier Science Publisher B.V., New York, 1984, pp. 931-1007.
8. Altmejd, M., and Spek, E., "Capabilities of NaS Batteries for Vehicle Propulsion," SAE Paper No. 890784, 1989.
9. Shemmans, M. J., Sedgwick, D., and Pekarsky, A., " NaS Batteries for Electric Vehicles," SAE Paper No. 900136, 1990.

10. Faust, K., Goubeau, A., and Scheuerer, K.,"Introduction to the BMW-E1," SAE Paper No. 920443, 1992.
11. Reisner, D., and Eisenberg, M., "A New High Energy Stabilized Nickel-Zinc Rechargeable Battery System for SLI and EV Applications," SAE Paper No. 890786, 1989.
12. Dickinson, B.E., Swan, D.H., and Lalk, T.R., "Comparison of Advanced Battery Technologies for Electric Vehicles," SAE Paper No. 931789, 1993.
13. Lucas, T., "How to Convert to an Electric Car," Crown Publishers, Inc., New York, 1976.
14. Slicker, J.M., and Kalns, I., "Advanced AC Powertrain for Electric Vehicles," SAE Paper No. 850200, 1985.
15. Kahlen, H., and Drumm, H.T., "A New Compact Drive-System with a Microcomputer Controlled Dual DC-Chopper," SAE Paper No. 891694, 1989.
16. Morris, P.E., and Adams, D.S., "Design Considerations and Component Selection for Volume-Produced EV Controllers," SAE Paper No. 900578, 1990.
17. Wyczalek, F.A., and Wang, T.C., "Regenerative Braking Concepts for Electric Vehicles - A Primer," SAE Paper No. 920648, 1992.
18. King, R.D., Park, J.N., Clock, A.W., and Watrous, D.L.," EXT-II 70 Hp MCT Inverter Electric Drive System Performance Tests," SAE Paper No. 920445, 1992.

19. Ellers, C., "The Evolution and Design of an Operational Hybrid/Electric Drive System," SAE Paper No. 901530, 1990.

20. Reuyl, J.S., "XA-100 Hybrid Electric Vehicle," SAE Paper No. 920440, 1992.

21. Triger, L., Paterson J., and Drozdz, P., "Hybrid Vehicle Engine Size Optimization," SAE Paper No. 931793, 1993.

22. Frantzeskakis, P., Dionatos, D., Kekedjian, H., Nikopoulos, A., and Theofanopoulos, J., "The Concordia University Hybrid Electric Conversion Vehicle," SAE Special Publication No. SP-980, 1993.

23. TUTSIM Products, "TUTSIM Users Manual," Palo Alto, CA, 1989.

24. Dorf, R.C., "Modern Control Systems," 5th ed., NY, NY, Addison-Wesley Publishing Company, 1989.

25. Solectria Electronics Division, "Technical Specifications Pamphlet," Arlington, MA.

26. Briggs and Stratton, "Engine Specifications Manual," Mississauga, Toronto.

27. Fisher Electric Motor Technology, Inc., "Technical Specifications," St. Petersburg, Florida.

28. Curtis Instruments, Inc., "Installation and Maintenance Manual," Dublin, CA.

29. Bussman Copper Industries," SPD Electrical Protection Handbook," 1992, Bridgeton, MO.

30. Unnewehr, L.E., and Knoop, C.W.,"Electrical Component Modelling and Sizing for EV Simulation," SAE Paper No. 780215, 1978.

31. Advanced DC Motor Inc., "Advanced DC Technical Specifications," Syracuse, NY.

32. Adler, U., "Bosch Automotive Handbook," 2nd ed., PA, Warrendale.: Society of Automotive Engineers, Inc., 1986.

33. Gillespie, D.T., "Fundamentals of Vehicle Dynamics," 1st ed., PA, Warrendale.: Society of Automotive Engineers, Inc., 1992.

34. DeLuca, W.H., Gillie, K.R., Kulaga, J.E., Smaga, J.A., Tummillo, A.F., and Webster, C.E., " Performance and Life Evaluation of Advanced Battery Technologies for Electric Vehicle Applications," SAE Paper No. 911634, 1991.

35. Dickinson, B.E., Swan, D.H., and Lalk, T.R., "Comparison of Advanced Battery Technologies for Electric Vehicles," SAE Paper No. 931789, 1993.

36. Reisner, D., and Eisenberg, M.," A New High Energy Stabilized Nickel-Zinc Rechargeable Battery System for SLI and EV Applications," SAE Paper No. 890786, 1989.

37. Ragone, D.V., " Review of Battery Systems for Electrically Powered Vehicles," SAE Paper No. 680453, 1968.

BIBLIOGRAPHY

1. Kucera, G., Plust, H.G., and Schneider, C., "Nickel-Zinc Storage Batteries as Energy Sources for Electric Vehicles," SAE No. 750147, 1975.
2. Rao, S.S., "Optimization - Theory and Practice," John Wiley & Sons, New York, 1984.
3. Tummala, M., Krepec, T., and Ahmed, A.K.W., "Simulation, Testing and Optimization of Natural Gas On-Board Storage System for Automotive Applications," SAE Paper No. 931820, 1993.
4. Danczyk, L.G., Scheffler, R.L., and Hobbs, R.S., " A High Performance Zinc-Air Powered Electric Vehicle," SAE Paper No. 911633, 1991.
5. Henrikesen, G.L., Patil, P.G., Ratner, E.Z., and Warde, C.J., "Assessment of EV Batteries and Application to R&D Planning," SAE Paper No. 890781, 1989.
6. Shemmans, J.M., Sedgwick D., and Pekarsky, A., " NaS Batteries for Electric Vehicles," SAE Paper No. 900136, 1990.
7. Kordesch, K.V., "Batteries," Marcel Dekker Inc., New York, 1977.
8. Tuck, C.D.S., "Modern Battery Technology," Ellis Horwood Ltd., West Sussex, England, 1986.
9. Papalambros, P.Y., and Wilde, D.J., "Principles of Optimal Design," McGraw-Hill Book Company, New York, 1978.

10. Rao, S.S., "Design of Vibration Isolation Systems Using Multiobjective Optimization Techniques," ASME Paper No. 84-DET-60, 1984.

11. Sinha, N.S., "Control Systems," 1st ed., NY, NY.: Holt, Rinehart and Winston, 1988.

12. Gopal, K.D., "Power Semiconductor Controlled Drives," 1st ed., NJ, Eaglewood Cliffs.: Prentice-Hall, Inc., 1989.

13. Winter, U., and Brandes, J., "Influence of Battery Characteristic on Traction Drive Performance," SAE Paper No. 940293, 1994.

14. Mackay, R., "Development of a 24 kW Gas Turbine-Driven Generator Set for Hybrid Vehicles," SAE Paper No. 940510, 1994.

15. Davis, G.W., Hodges, G.L., and Madeka, F.C., "The Development and Performance of the Amphibian Hybrid Electric Vehicle," SAE Paper No. 940337, 1994.

16. Madeka, F.C., Davis, G.W., and Hodges, G.L., "The Selection of Lead-Acid Batteries for Use in Hybrid Electric Vehicles,: SAE Paper No. 940338, 1994.

17. Frantzeskakis, P., Krepec, T., and Sankar, S., "Specific Analysis on Electric Vehicle Performance Characteristics with the Aid of Optimization Techniques," SAE Paper No. 940336, 1994.

APPENDIX 1

Electric Motor and Controller Specifications

Advanced D.C. Motors, Inc.

ELECTRIC VEHICLE APPLICATIONS
S-2 THERMAL DATA PER ISO STANDARDS
203-06-4001 8" DIA. MOTOR

75 - .031
96 - .031

Voltage Curves

Class - H Temperature

Time On	*Volts*	*Amps*	*RPM*	*H.P.*	*KW*
		75 Volts			
5 Minutes	**64**	**360**	**2750**	**26.2**	**19.8**
15 Minutes	**67**	**290**	**3150**	**22.5**	**16.9**
30 Minutes	**68**	**248**	**3520**	**19.5**	**14.6**
1 Hour	**69**	**218**	**3650**	**17.5**	**13.2**
Continuous	**69**	**200**	**3750**	**16.0**	**12.1**
				Peak H.P. - 38	
		96 Volts			
5 Minutes	**86**	**322**	**3600**	**31.5**	**23.8**
15 Minutes	**88**	**260**	**4100**	**26.5**	**20.0**
30 Minutes	**90**	**210**	**4500**	**22.8**	**16.8**
1 Hour	**91**	**190**	**4800**	**20.6**	**15.5**
Continuous	**91**	**178**	**5000**	**19.0**	**14.4**
				Peak H.P. - 52	

Test performed with fully seated brushes

Date: 2/13/92

XC-69 Sheet 3

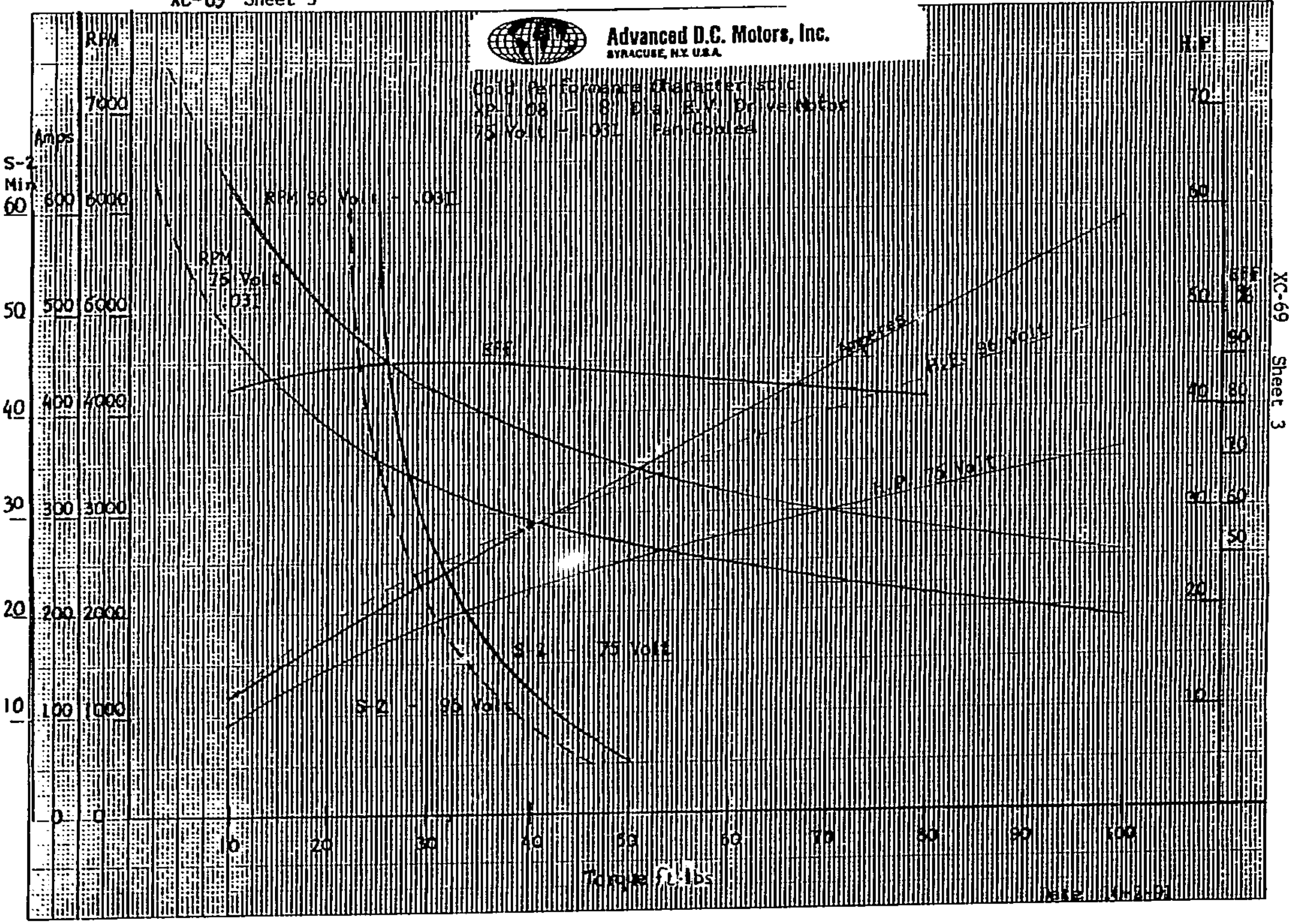
Advanced D.C. Motors, Inc.
SYRACUSE, N.Y. U.S.A.
Cold Performance Characteristic
XP-1108 - 8" Dia. E.V. Drive Motor
75 Volt - .031 Fan Cooled
S-2 Min
Amps
RPM
H.P.
EFF %
RPM 96 Volt - .031
RPM 75 Volt .031
EFF
Amperes
H.P. 96 Volt
H.P. 75 Volt
S-2 - 75 Volt
S-2 - 96 Volt
Torque ft. lbs
10
20
30
40
50
60
70
80
90
100
0
1000
2000
3000
4000
5000
6000
7000
100
200
300
400
500
600
XC-69 Sheet 3

CURTIS PMC

DATA

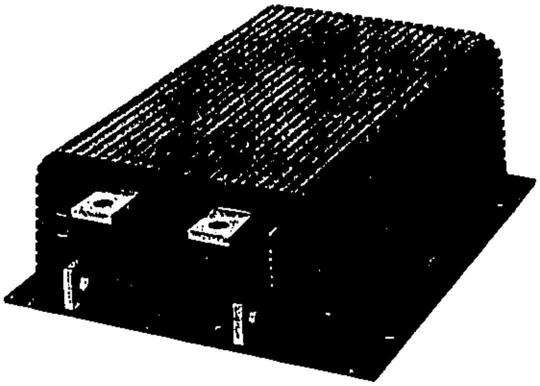

CURTIS PMC MODEL 1209/1221
HIGH POWER ELECTRONIC
MOTOR SPEED CONTROLLER

The **Curtis PMC 1209&1221** are high power electronic motor speed controllers designed to provide smooth, silent, efficient and cost effective speed and torque control for a wide variety of industrial electric vehicle applications. The **1209/1221** combines proven Curtis PMC 1204 power MOSFET controller technology with extended operating features and power ranges. Typical applications include industrial trucks, airport equipment, tow tractors, personnel carriers, forklift applications, on-road vehicles, scissors lift and boom trucks, etc.

FEATURES:

- High frequency switching and ultra low voltage drops provides very high efficiency, silent operation. Costs, heatsinking requirements and motor and battery losses are reduced. Low end torque, range and battery life are increased.
- Total environmental protection provided by epoxy sealed (factory serviceable) rugged anodized aluminum extrusion housing. Simple mounting and wiring with push-on type connectors for control signals. Large solid copper buses used for all power connections.
- Thermal protection and compensation circuit provides undertemperature cutback, constant current limit over operating range and linear rollback in overtemperature. No sudden loss of power under any thermal conditions.
- Adjustable acceleration rate, current limit (protected against exceeding controller rating) and plugging current limit. Adjustments are accessed through sealed screws on side of housing.
- Variable plugging current feature provides throttle position control over braking to improve driveability.
- Full fault detect circuitry monitors power supply, throttle connections, output transistors, etc., to prevent runaway. Neutral start option requires that throttle be returned to neutral before output is allowed. Static return-to-off option requires that F/R selector be returned to neutral before output is allowed.
- Arcless contactor switching for F/R contacts and bypass contacts (if opened below controller current limit).
- Delayed bypass (1A) output drives optional bypass contactor, after throttle reaches 90% and bypass delay times out. Short circuit protected F/R and bypass contactor drivers. (These features only for models ≤36 volts)

WARRANTY : One year from date of delivery, subject to conditions of warranty.

CURTIS PMC • AL SION OF CURTIS INSTRUMENTS, INC., • 6591 SIERRA LANE • DUBLIN, CA 94566 15) 828-5001
CURTIS INSTRUMENTS, INC., • 200 KISCO AVENUE • MT. KISCO, NY 10549 • (914) 666-2971 • FAX (914) 666-2188

SPECIFICATIONS:

MODEL NUMBER	INPUT VOLTAGE (volts)	CURRENT LIMIT (amps)	2 MIN RATING (amps)	5 MIN RATING (amps)	1 HOUR RATING (amps)	VOLTAGE DROP@ 100 A	UNDER-VOLTAGE CUTBACK (volts)
1209-46xx	24-36	500	500	350	225	<.15V	16
1209-55xx	36-48	450	450	300	200	<.30V	21
1209-64xx	48-72	400	400	275	175	<.30V	32
1209-62xx	48-72	275	275	200	125	<.45V	32
1209-61xx	48-72	175	175	125	75	<.70V	32
1209-72xx	72-120	275	275	175	100	<.70V	48
1221-48xx	24-36	600	600	425	250	<.10V	16
1221-57xx	36-48	550	550	375	225	<.25V	21
1221-66xx	48-72	500	500	350	200	<.25V	32
1221-74xx	72-120	400	400	250	150	<.50V	48

LB

Frequency of operation: 15 kHz
Standby Current: <20 ma
Standard Throttle Input: 0-5KΩ (others available)
Weight: 1209=8.8 lb, 1221=10.8 lb

DIMENSIONS :

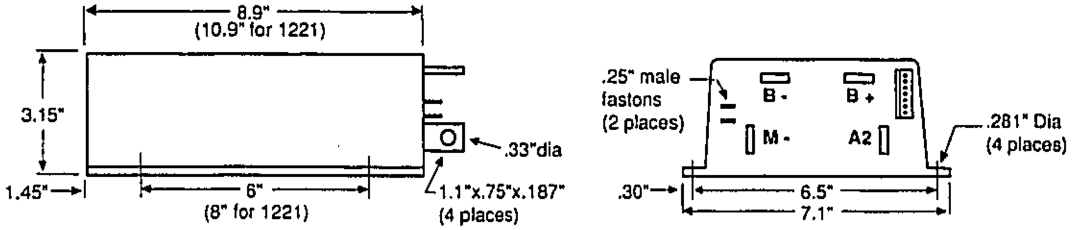

TYPICAL INSTALLATION :

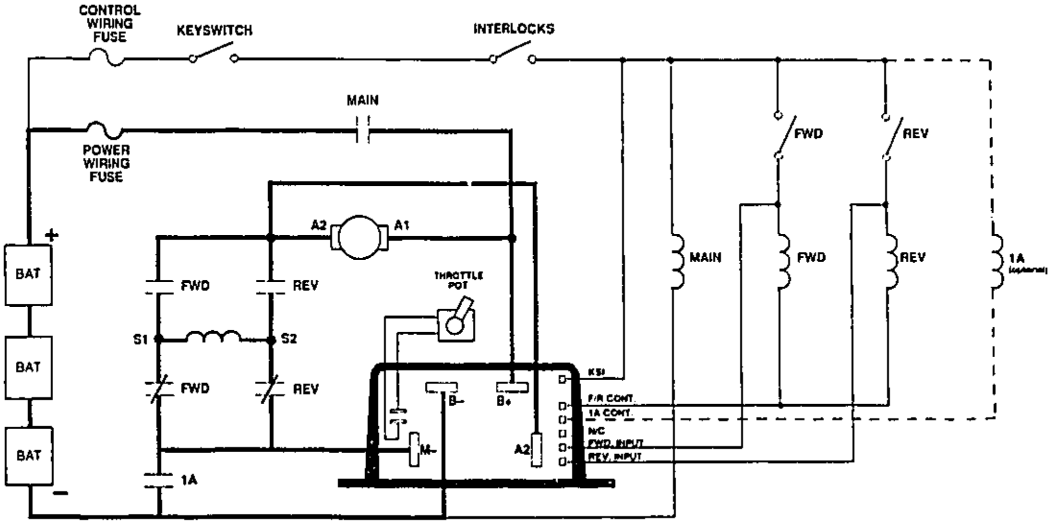

Brushless Permanent Magnet Motors

SOLECTRIA
Electronics Division
27 Jason Street
Arlington, MA 02174

• Models BRLS8 / BRLS11 / BRLS16

- highest efficiency
- no brushes
- sealed motor
- low rotating loss
- very low electrical resistance
- best power-to-weight ratio
- compact
- efficient cooling

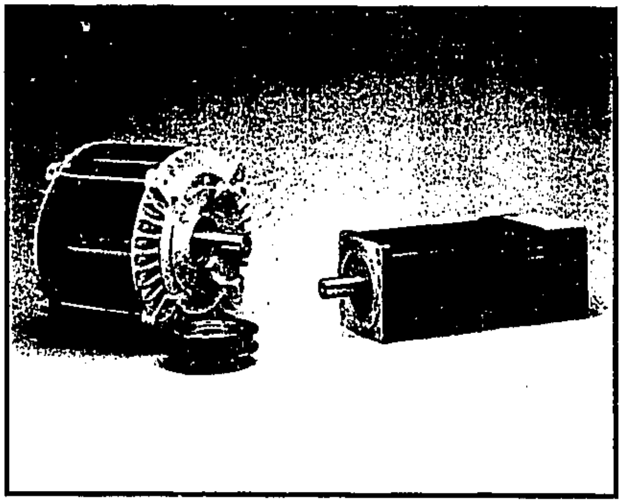

• Description

The brushless permanent magnet motor drive system is the ultimate in power, efficiency, reliability and minimized weight. From the Spirit of Biel to the Solectria 5 to the Flash and Force GT, it is the technology that has won more races around the world.

Solectria brushless motors use rare earth magnets for maximum power density in size and weight.
The motors have the best cooling because the windings are on the outside shell of the motor. Because of this geometry, there is more room for copper, offering lower electrical resistance.

To double the torque of the motor, a two speed switch can be used. This switch system involves two windings which are placed in series for 1st speed and parallel for 2nd speed. The first speed allows twice the torque to be produced with the same current from the controller. Ask one of our engineers about this!

•Dimensions

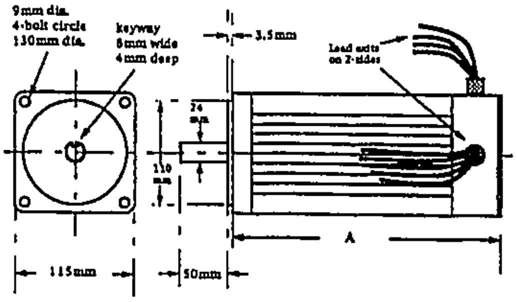

motor	Dim "A"
BRLS8	300 mm
BRLS11	375 mm

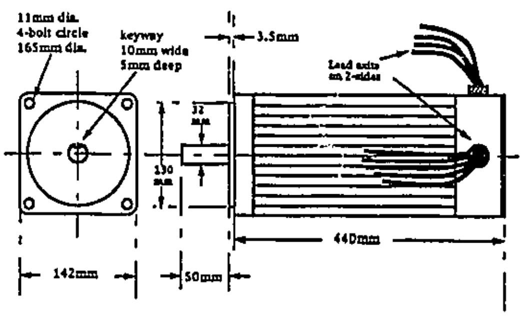

motor
BRLS16

•Specifications

Model	BRLS 8	BRLS11	BRLS16	
continuous power output	8	11	16	HP
peak power output	15	20	30	HP
nominal voltage	60 /120	120	144	V
continuous stall current	140 / 70	100	120	A
peak current	280 / 140	200	240	A
continuous stall torque	12	17	28	NM
peak torque	25	32	56	NM
peak motor efficiency	95	95	94	%
operating speed	6000	7000	5000	rpm
winding resistance	0.021 / 0.085	0.050	0.012	Ω
weight	26	32	64	lbs

•Units
Mechanical power out
= (NM) π rad / sec
= Watts out (π rad / sec = 0.105 x rpm)
So, Power
= NM x 0.105 x rpm = Watts
1ft-lb = 1.357 NM
1HP = 746 Watts = 550 ft-lb / sec

...ask about other system voltages.

•Speed-Torque Curves

BRLS8

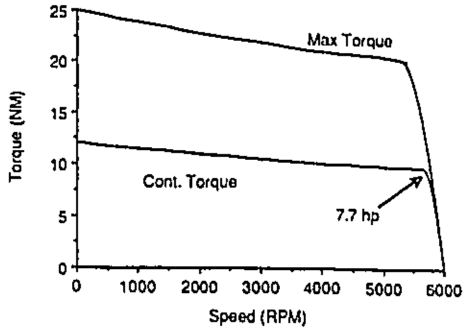

BRLS11

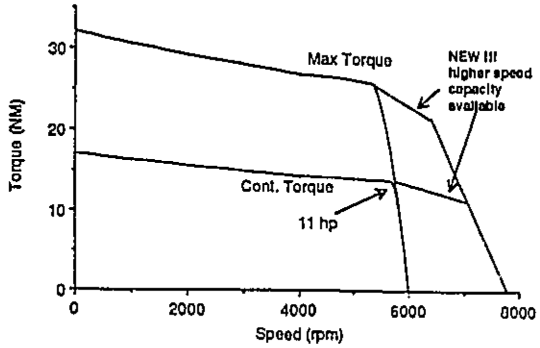

BRLS16

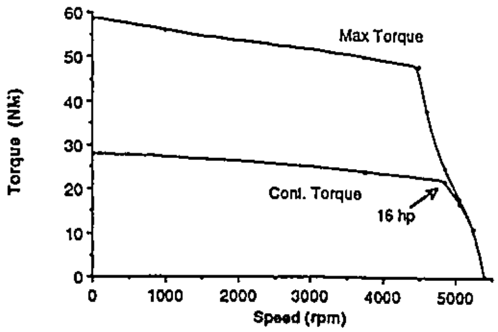

•Efficiency

BRLS8

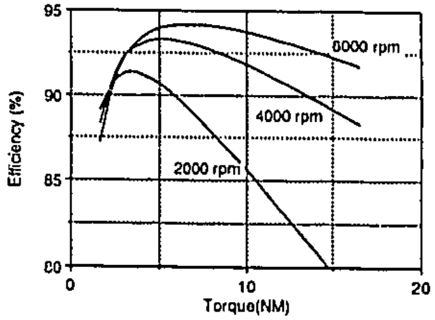

BRLS11

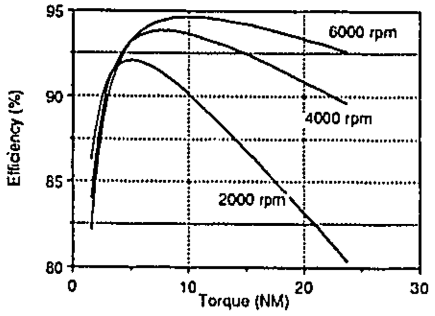

BRLS16

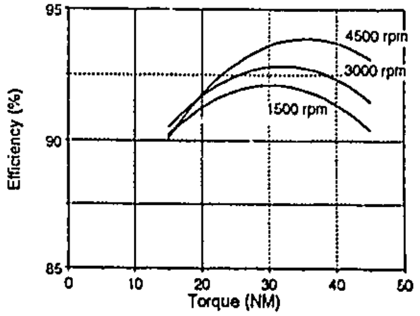

Solectria
27 Jason Street
Arlington, MA 02174
(508) 658-2231
fax: (508) 658-3224

SET-UP

MOTOR CONTROLLER FACE PLATE

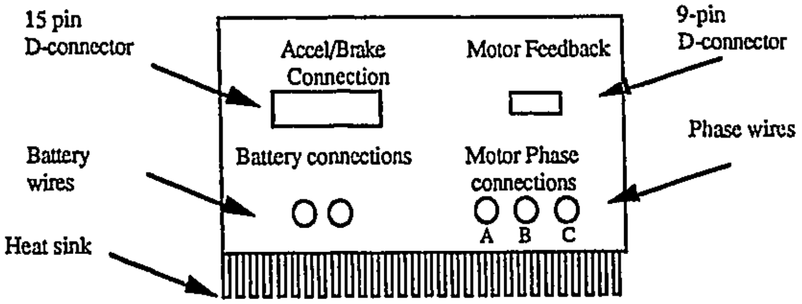

Accel/Brake Connection

To connect the accelerator and brake controls to the Motor Controller, you will need:

1. two (2) 10KΩ potentiometers (or 2 of Solectria's 5KΩ accelerator/brake controller, model ABC1)
2. one (1) 15 pin male D connector
3. one (1) double-pole, single throw switch

Please use good quality potentiometers and be sure that the connecting work, soldering etc. is done by a skilled person. The motor controller is designed with some protection for bad pot connections, but shorting certain pins could damage the controller. Wrong or faulty potentiometer connections can be very hazardous — Remember, you are dealing with automobiles, boats and other powerful potentially dangerous machines.

Potentiometer (Pot.)

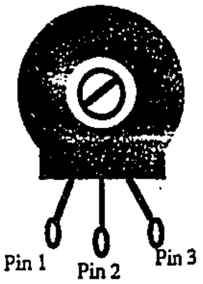

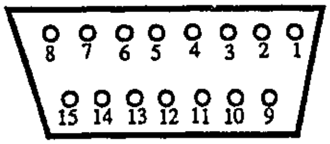

Close Up of 15-pin female D Connector (found on the controller box)

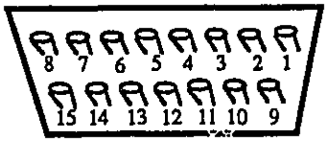

Close Up of soldering side of 15-pin male D connector (This connector plugs into the controller box female D connector)

To connect the potentiometer that controls acceleration:

1. Connect pin 1 of the pot. to pin 1 of the male D connector.
2. Connect pin 2 of the pot. to pin 2 of the male D connector.
3. Connect pin 3 of the pot. to pin 3 of the male D connector.

To connect the potentiometer that controls regenerative braking:
1. Connect pin 1 of the pot. to pin 9 of the male D connector.
2. Connect pin 2 of the pot. to pin 10 of the male D connector.
3. Connect pin 3 of the pot. to pin 11 of the male D connector.

Solectria
27 Jason Street
Arlington, MA 02174
(508) 658-2231
fax: (508) 658-3224

BRUSHLESS MOTOR CONTROLLER

(with regenerative braking)

ModelS BRLS100H, BRLS150, BRLS250, BRLS240H

Caution!

Follow these instructions carefully. Improper set-up may damage equipment or injure user.
→ THE UNIT IS <u>NOT</u> WATER SEALED-PLACE IN A WATER TIGHT CLIMATE! ←

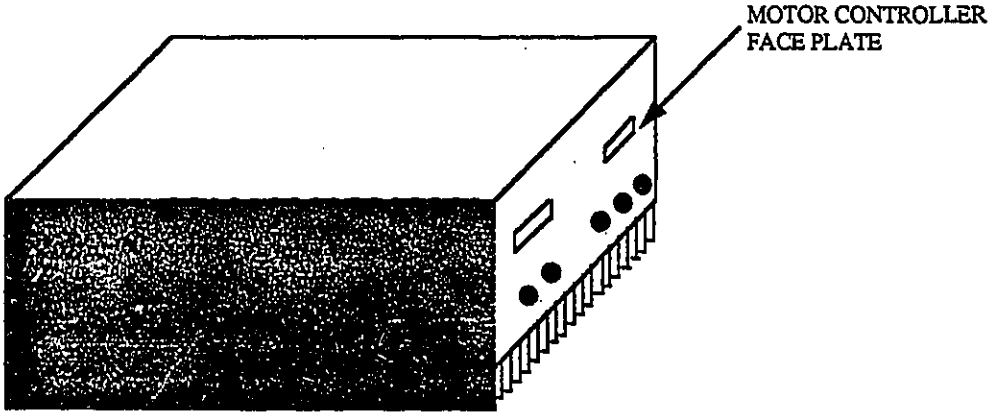

THE UNIT

The Solectria brushless motor controller is specifically designed to control the speed and torque of a brushless permanent magnet motor. This brushless motor controller is a variable frequency, current controlled, current limited control system. It is based on a super low-resistance MOSFET switched at up to 20kHz. This controller requires an inductive load which must be within a prescribed range or the MOSFET devices could be damaged. A very low or high motor inductance must be accounted for in the values of the power stage and circuit board elements which are installed at the factory.

Depending on the model, the controller can control up to 100A, 150A, 200A, or 240A of motor current in drive or regenerative braking mode. The basic control topology is that of a down converter. If the motor is running at half speed, its peak voltage per phase will be half that of the battery and the peak motor current per phase will be double that of the battery. At full speed, the peak voltages and peak currents will be similar.

SR180LC/CR20-300
at 200 Vdc

MOTOR PARAMETERS:

Rated Power (kW)	24.6
Peak Torque Continuous @ 6,500 rpm (in-lb)	320
Peak Torque - Continuous Stall (in-lb)	358
Peak Torque - Intermittent Stall (in-lb)	840
Max No-Load Speed @ 200 Volts (rpm)	7,500
Motor EMF Constant (K_E, V/Krpm)	30
Motor Torque Constant (K_T, in-lb/Amp)	2.2
Cooling Type - Water Cooled	-
Max Winding Temperature (°F)	300
Winding DC Resistance ℓ-ℓ @ 25°C (ohms)	.056
Winding Inductance @ 25°C (µH)	88
Number of Poles	18
Rotor Inertia (in-lb-sec^2)	.200
Motor Weight (lbs)	44

Multiple Winding Configurations are Available.

SYSTEM FEATURES:

- Rugged Design
- Lighter Weight and Reduced Electrical Losses
- High Energy Neodymium Iron Boron Magnets and High Pole - Count Design for Highest Power Density
- High Efficiency
- Regeneration to Zero Speed
- 4 Quadrant Operation
- Closed Loop Speed Control
- Adjustable Current Limit - Factory Preset
- +/- 10 V Speed Setpoint and Feedback

CONTROLLER PARAMETERS:

Max Vin (Vdc)	200
Min Vin (Vdc)	30
Min - No Load Current (amps)	0.150
Input Capacitance (µf)	19,040
Controller Weight (lbs)	48

- All data subject to change without notice.

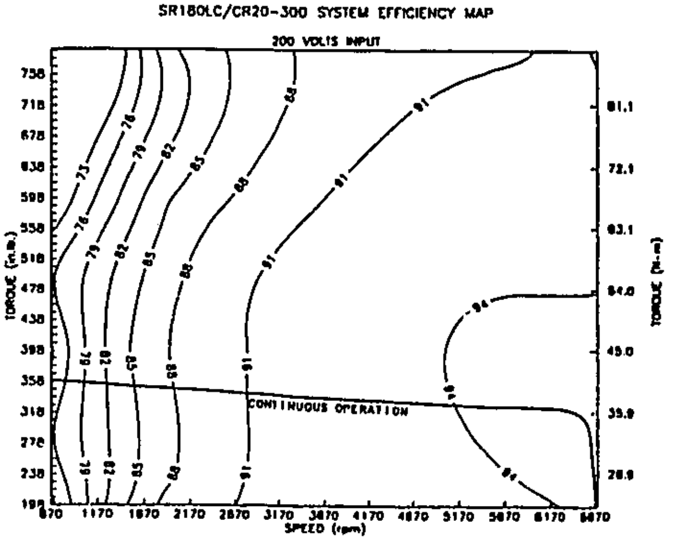

SR218L/(2) CR20-300
at 200 Vdc

MOTOR PARAMETERS:

Rated Power (kW)	60
Peak Torque Continuous @ 5,800 rpm (in-lb)	875
Peak Torque - Continuous Stall (in-lb)	920
Peak Torque - Intermittent Stall (in-lb)	1,320
Max No-Load Speed @ 200 Volts (rpm)	7,000
Motor EMF Constant (K_E, V/Krpm)	30
Motor Torque Constant (K_T, in-lb/Amp)	2.5
Cooling Type - Water Cooled	-
Max Winding Temperature (°F)	300
Winding DC Resistance ℓ-ℓ @ 25°C (ohms)	.038
Winding Inductance @ 25°C (µH)	48
Number of Poles	18
Rotor Inertia (in-lb-sec^2)	.420
Motor Weight (lbs)	110

Multiple Winding Configurations are Available.

CONTROLLER PARAMETERS:

Max Vin (Vdc)	200
Min Vin (Vdc)	30
Min - No Load Current (amps)	0.150
Input Capacitance (µf)	19,040
Controller Weight (lbs)	44

2 Controllers Required

- All data subject to change without notice.

SYSTEM FEATURES:

- Rugged Design
- Lighter Weight and Reduced Electrical Losses
- High Energy Neodymium Iron Boron Magnets and High Pole - Count Design for Highest Power Density
- High Efficiency
- Regeneration to Zero Speed
- 4 Quadrant Operation
- Closed Loop Speed Control
- Adjustable Current Limit - Factory Preset
- +/- 10 V Speed Setpoint and Feedback

SR218L/(2) CR20-300 SYSTEM EFFICIENCY MAP

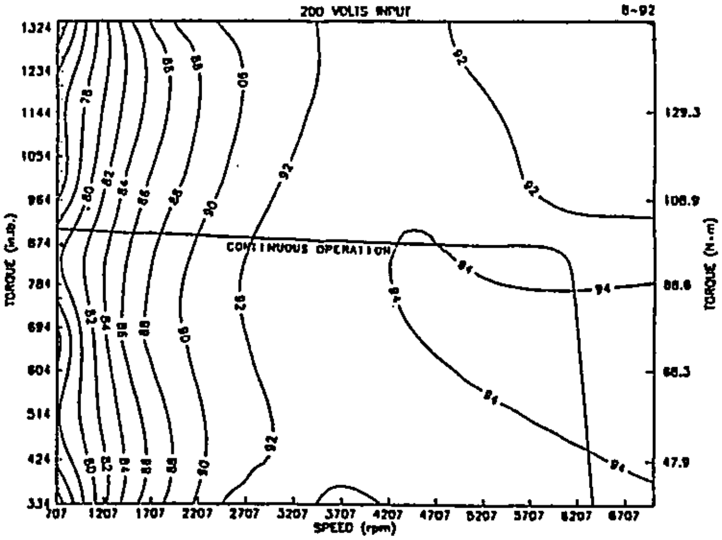

APPENDIX 2

Instrumentation Specifications

INSTALLATION MANUAL KILOWATT-HOUR+ METER

KILOWATT-HOUR+ Meters are designed to monitor battery systems up to 500V. The KILOWATT-HOUR+ Meter measures the number of Kilowatt-hours (Kwhr) consumed from a fully charged battery. It also measures the voltage of the battery and the current being consumed from or supplied to it.

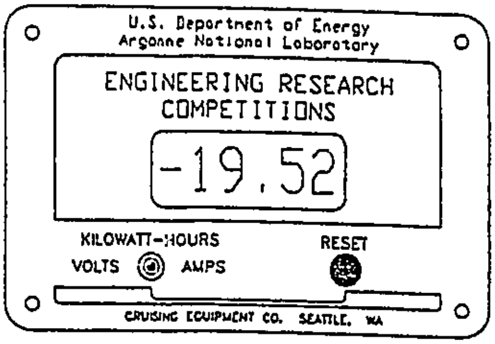

Dimensions: 4.5' x 3.0" x 1.5" Deep Cutout 3.5" x 2.5"

This installation manual is designed to provide you with the information necessary to install and use your KILOWATT-HOUR+ Meter. Please read it!

TABLE OF CONTENTS

DESCRIPTION OF THE FRONT PANEL SWITCHES

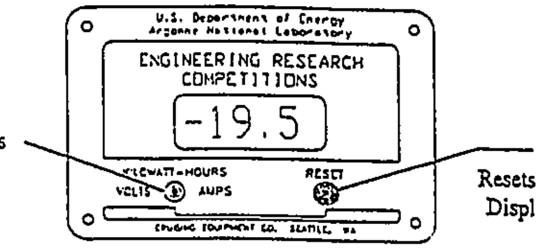

Display Function Switch
Chooses what is displayed:
Volts, Amps, or Kilowatt-Hours

Reset Switch
Resets Kilowatt-Hours to Zero.
Displays time since last reset.

DISPLAY FUNCTION SWITCH

The Display Function switch chooses which battery parameter is displayed: Volts, Amps, or Kilowatt-hours consumed from the battery.

VOLTS FUNCTION

When the Display Function switch is in the VOLTS position the battery voltage is displayed as a positive number with 0.5 Volts resolution. The range is from 0.0V to 500.0V.

AMPS FUNCTION

When the Display Function switch is in the AMPS position, current being consumed from the battery is displayed as a negative number. If current is being supplied to the battery it is displayed as a positive number. The current is displayed with 1 Amp resolution. The range is from -500A to 500A.

KILOWATT-HOUR FUNCTION

KILOWATT-HOURS CONSUMED: When the Display Function switch is in the KILOWATT-HOURS position the number of Kilowatt-hours (Kwhr) consumed from the battery is displayed as a negative number. During discharge the negative number will grow as Kwhrs are consumed and the meter counts down. During charging the number of Kwhrs consumed will decrease as the meter counts back up toward zero. The range is ± 99.99Kwhrs.

CHARGE EFFICIENCY FACTOR: The meter uses a Charge Efficiency Factor (CEF) of 100%. During charging the meter counts back up toward zero at the same rate that it counted down. The CEF of a battery system may be calculated by logging the Kwhrs consumed, charging until the battery meets the Charged Parameters, and comparing the Kwhrs returned. An example is shown on Page 6.

RESET SWITCH

TIME SINCE LAST RESET: When the Reset Switch is depressed, the time since the last reset is displayed with 0.1min. resolution. The maximum display is 999.9 minutes. This is equal to 16.67 hours. The display rolls over and continues counting from 0.0 if the time exceeds the maximum. Do not press for longer than 10 seconds to avoid a reset.

RESETTING THE METER: The Kilowatt-hours consumed display is reset to Zero if the reset button is pressed for 10 seconds. The long delay is to avoid unintentional resets.

When the battery has met the Charged Parameters, the meter may be reset. If charging continues, overcharge Kwhrs will be counted and displayed as a positive number. After charging, and just prior to using the battery system, the meter should again be reset to remove any accumulated Kwhrs.

SPECIAL FEATURES:

RS-232 OUTPUT

The RS-232 output allows the KILOWATT-HOUR+ Meter to input data to a Personal Computer. The ASCII space delimited output may be read to a file and captured for later input to a database, spreadsheet, or graphing program of your choice. The format of the data is as follows:

TIME (SECONDS)	KWHRS	AMPS	VOLTS
XXXXX	±XX.XX	±XXX	XXX.X

The RS-232 output generates one line of data per second. At that rate about 90 Kbytes of file space is used per hour of data logging.

The easiest way to log data is to use Windows*. The following description should only be considered an introductory guide. Please consult your Windows documentation.

Start Windows
Choose Accessories
Choose Terminal
Choose Settings
Choose Communication
Select the Following:

9600	Baud Rate
8	Data Bits
1	Stop Bit
None	Parity
None	Flow Control

Leave Parity check and Carrier Detect "Off" (No 'x')
Choose the serial port that the cord is plugged into (typically COM1 or 2).
OK

You are prepared to receive data.

To Save to a File:

Choose Transfer
Choose Receive Text File
Type the full path and the name of the destination file or use the mouse to choose the directory and type the file name. Example: C:\WORK\DATA\TEST1.TXT
OK
STOP. (when done click stop)

The file may be imported into the spreadsheet or data base of your choice.

SYNCHRONIZING KILOWATT-HOUR+ Meters TO A CHARGED BATTERY

The KILOWATT-HOUR+ Meter may be used to indicate the actual number of Kwhrs consumed from the battery only if it is synchronized with its state of charge. A charged battery has zero Kwhrs removed. Resetting the meter to zero when the battery has met the Charged Parameters synchronizes the meter to the battery. The following charged parameters are examples of when a charging system has put as much energy into a battery as it normally can.

CHARGED PARAMETERS

The wide variety of battery chemistries that the KILOWATT-HOUR+ Meter may be used with prevents a universal definition of the Charged Parameters for a "full battery". Typically a maximum charge voltage is specified. When that voltage is maintained and the current flowing into the battery drops to 1% or 2% of capacity the battery may be considered full. The manufacturer may also specify a length of time at a particular voltage as a full battery. The following are examples of charged parameters for Lead-Acid battery chemistry. Please consult your manufacturer for the Charged Parameters appropriate for your battery.

CONSTANT VOLTAGE CHARGING SYSTEMS

Constant voltage charging systems have restored as much charge to a battery as they can when the voltage reaches the maximum regulation point and the charging current drops to less than 1% of the battery capacity. A full charged voltage of 2.3 to 2.45 Volts per cell would be typical. It can take more than 8 hours for a battery to reach this state of charge.

MULTIPLE STAGE CHARGING SYSTEMS

With a Multiple Stage Charging system, the battery is charged when the system switches to the Float cycle. If properly setup, the transition from Acceptance Charging to Float will occur when the charging current, at the Acceptance Voltage (about 2.4 Volts per cell), drops to about 1% or 2% of the battery capacity. (See description below of Multiple Stage Charging.)

USING SPECIFIC GRAVITY

Specific gravity of the battery can also be used to determine the charge level of a battery. Regardless of the charging system a battery is charged when the specific gravity shows no increase for three hours, when measured at 30 minute intervals.

ABOUT MULTIPLE STAGE CHARGING

IDEAL CHARGE CURVE

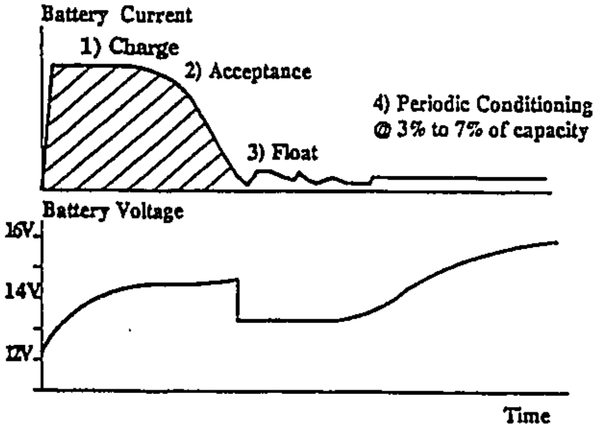

The CHARGE CYCLE supplies a bulk current to the batteries at a rate limited by charging source capacity or battery capacity. The CHARGE CYCLE continues until the battery reaches about 2.4 Volts per cell. ACCEPTANCE CHARGING now begins as the battery accepts whatever current it can, until it is accepting only a small current (1% or 2% of capacity). At this point the battery is charged. The FLOAT cycle begins, maintaining the batteries at about 2.2 Volts per cell. The CONDITION cycle is constant current "equalization" at a charge rate of 3% to 7% of battery capacity. The volatage is allowed to rise to a a maximum of 2.7 Volts per cell. The batteries should be CONDITIONED every 30 days, particularly during deep cycling service.

Series 54Z *Pickups*

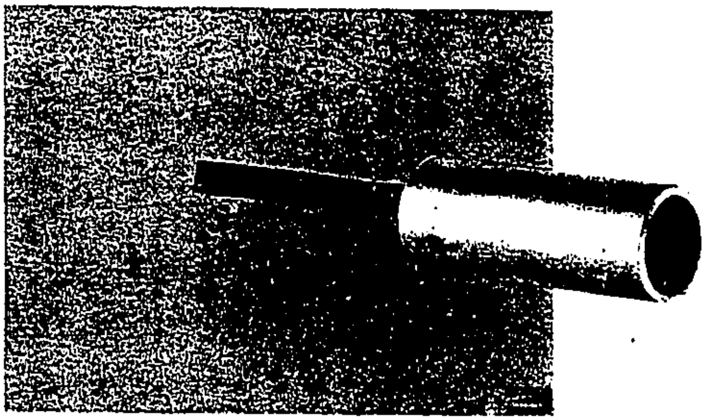

- *Low Cost Pickup*
- *Compact Design*
- *Simple Installation*
- *Wide Operating Range*

The Series 54Z pickups offer new levels of economy, performance and convenience to sensing devices. The Series 54Z sensors operate over a wide range of air gaps, making them suitable for parts counting and speed sensing applications. The wide operating voltage makes them compatible with most counters, indicators or controllers. The Series 54Z does not require a minimum target speed, and can operate from zero up to 20,000 targets per second. Commonly used targets include gear teeth, slotted discs, shafts with keyways, bolt heads, etc. made of carbon steel, iron, or magnetic stainless steel. This low cost sensor offers reliable operation in wet, dirty and high temperature environments.

Applications

- Parts counting
- Speed sensing
- Sensor for PLC's and indicators

Application Guidelines:

For ease of installation and optimum performance, a keyway is provided so that the sensor may be visually aligned with the target's direction of travel.

```
Target Requirements:

Gap: 0.005 to 0.003 inch
Length: 0.081 inch min.
Separation: 0.081 inch min.
Width: 0.375 inch min.
Height: 0.081 inch min.
Speed: 0 to 20,000 targets/sec. max.
```

Target Requirements

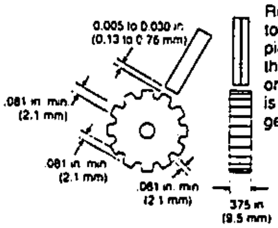

Remember to rotate the pickup so that the line on the side is parallel to gear travel.

SPECIFICATIONS

Power Requirements: 5 to 18 VDC, 10 mA plus load

Weight: 2 oz.

Operating Temperature: -40 to +105 °C (-40 to +220 °F.)

Cable: 105 °C, PVC insulation, 10 foot length

Material: Stainless 303 Steel

Approximate Dimensions

54Z Pickup

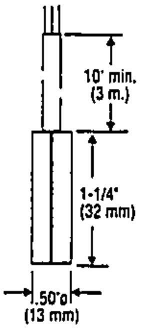

Mounting Clamp

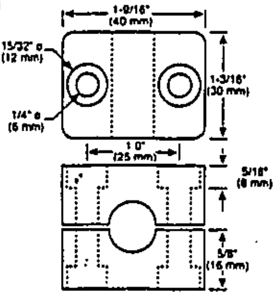

Typical Application

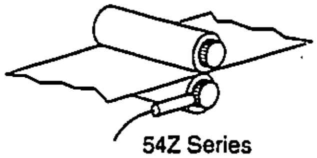

Electrical Output Ratings

Outputs	Voltage Range	Sink (mA)	Source (mA)	Operating Speed
Current Sink (open collector w/2.2 kΩ pull-ups)	5 to 18 VDC	17	0.9 mA @Vcc–2V output	20 kHz max.

Electrical Connections

Function	Series 54Z Wire Color Code
5 to 18 VDC	RED
Signal	YEL
Common	BLK

60 Tooth Gears

Part No.	Dia.	Bore
16002070081	3-1/10"	3/8"
16002070083	3-3/4"	1/2"
16002070184	3-3/4"	5/8"
16002070185	3-3/4"	7/8"
16002070216	5-1/2"	1-1/8"
16002070217	5-1/2"	1-3/8"
16002070218	5-1/2"	1-5/8"
16002600314	5-1/2"	1-7/8"
16002600315	5-1/2"	2"
16002600316	5-1/2"	2-1/8"
16002600317	5-1/2"	2-1/4"
16002600318	5-1/2"	2-3/8"
16002600319	5-1/2"	2-1/2"
16002600320	5-1/2"	2-7/8"

Ordering Information

Output Waveform	Description	Model No.
Unidirectional A 	Pickup	54Z
	Clamp	605213

FloScan Instrument Company, Inc.

3016 N.E. Blakely Street, Seattle, Washington 98105
Phone (206) 524-6625

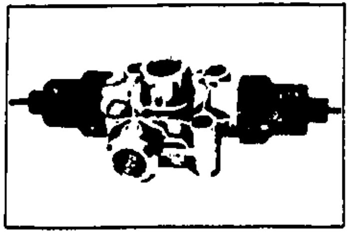

Series 100
Flow Transducers

Application Series 100 Flow Transducers measure non-pulsating flows of gasoline, light oils, and organic liquids in marine engines, diesel truck engines, bearing test stands, etc. Compatible low cost rate meters and totalizers are available.

Description Turbine flow transducers with removable opto-electronic pickups using either an incandescent or solid state light source. Zinc die cast construction with jewel bear-ings. 12VDC operation.

Features

- 3 models with 10/1 linear range 1.5-15 GPH, 2.5-25 GPH, 5-50 GPH
- Low pressure drop
- 9,000 - 15,000 pulses/gal.
- ¼" NPT port size
- Price: From $85 singly to $15 in quantity

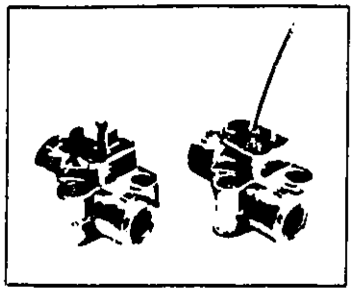

Series 200
Flow Transducers

Application Series 200 Flow Transducers measure non-pulsating flows of gasoline, diesel oil, hydraulic oil, and organic liquids in aircraft and diesel engine fuel monitoring systems, industrial furnaces, engine test stands, etc. Used in both OEM and laboratory applications. Compatible readouts are available.

Description Flow transducers of a proprietary turbine type design. Permanent solid state opto-electronic pickup gives a pulse signal. Models available with or without internal preamplifiers. Zinc or aluminum die cast constructions with sapphire bearings. 5-15VDC operation.

Features

- 2 models with 100/1 linear range
- Linearity of ±2.5% of reading for gasoline or #2 diesel oil
- Low pressure drop
- 80,000 - 100,000 pulses/gal.
- FAA approved for aircraft use
- Price: From $120 singly to $46 in quantity

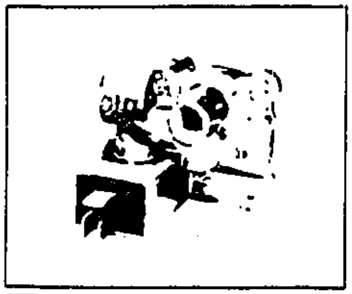

Series 261PB-15
Flow Transducers

Application The Series 261PB-15 Flow Transducer measures pulsating flows of gasoline in carbureted engines for automotive fuel monitoring systems and engine test stands. Used in both OEM and laboratory applications. Compatible MPG meters, rate meters and totalizers for lab and vehicle use.

Description Turbine flow transducers with an integral diaphragm pulsation bypass and provision for vapor return to insure accuracy in automotive fuel systems using carburetors and/or diaphragm fuel pumps. Permanent solid state opto-electronic pickup with internal preamplifier. Aluminum and zinc die cast construction. 5-12VDC operation.

Features

- 0.5-25 GPH linear flow range
- Linearity ±2% of reading, 1.5-5 GPH
  ±3% of reading, 0.5-25 GPH
- 48,000 pulses/gal.
- Very low pressure drop, 0.1 psi @ 8 GPH
- Price: From $165 singly to $63 and below in quantity

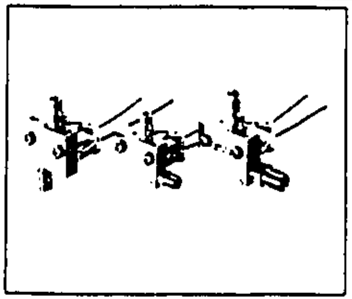

Series 300
Flow Transducers

Application Series 300 Flow Transducers measure low flows of clear liquids in solar collectors, beverage dispensing systems, chemical metering systems, etc. Their low flow capability and low cost have opened up many new OEM as well as general instrumentation applications for turbine type flow transducers. Compatible low cost electronic readouts are available.

Description Flow transducers of a proprietary turbine type design with an opto-electronic pickup isolated from the liquid. Corrosion resistant plastic and stainless steel construction with sapphire bearings. Models available with FDA approved materials.

Features

- 3 models with 10/1 linear range 2-30 GPH, 12-120 GPH, 30-300 GPH
- Linearity, ±2.5% of reading on water
- ⅛" NPT and ¼" NPT ports
- Max operating temperature 100°C
- Price: From $165 singly to $66 in quantity

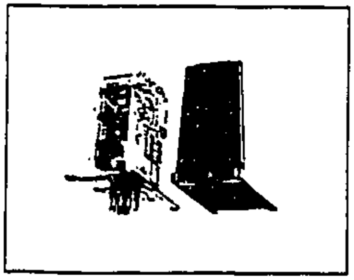

Series 3000
Electronic Readouts

Applications Series 3000 Electronic signal conditioners, digital to analog outputs, totalizers, and batch counters are compatible with Series 200, 261PB-15, and 300 flow transducers. Analog output models available with analog or digital panel meters.

Description Series 3000 readouts are versatile, electronic instruments which supply regulated power to flow transducers, compensate for variations in transducer signals, and discriminate against electrical interference. Acrylic inclosures with octal socket assemblies. Excellent technical performance at moderate cost.

Features

- Power input: 12VDC or 10VAC
- 0-5VDC analog output
- Fixed or variable K-Factor totalizers and batch counters
- 0-12VDC square wave output (all models)
- 5VDC power supply on analog outputs for panel meters, etc

FloScan Instrument Company, Inc.

3016 N.E. Blakely St.
Seattle, WA 98105
(206) 524-6625

ELECTRONIC MODULES

SERIES 3000

Description

Series 3000 electronic modules interface FloScan turbine flow transducers with various readout and control devices. These modules contain an integral power supply to drive the light emitting diode in FloScan Series 100-S, 200, 261 and 300 flow transducers. Series 3000 input circuitry compensates for opto-electronic pickups with different sensitivities, for liquids with different light transmitting characteristics, and for different transducer signal peak-to-valley ratios. To accomplish this the input circuitry contains a variable gain stage coupled to a peak current detector. This is followed by a low pass filter and a Schmitt trigger for optimum noise rejection. The buffered output of the Schmitt trigger is available to drive frequency counters, oscilloscopes, etc.

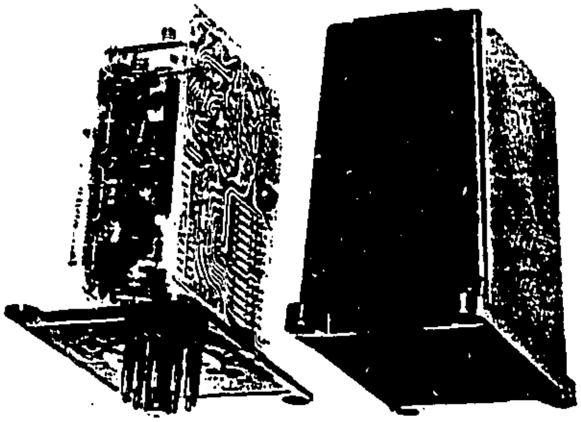

Analog output modules have a precision frequency to voltage converter; the voltage is the analog equivalent of the flow rate. The analog output voltage is filtered by a two pole low pass active filter to give a steady display on analog or digital panel meters. The 3002 module contains a 5VDC, 200mA power supply to operate a digital panel meter. Modules with analog outputs can have one of three different input frequency ranges to match any specified FloScan transducer.

Totalizer modules have a programmable binary divide-by-"n" counter inside the module and a separate electromechanical counter. When the module has received "n" pulses from the flow transducer the electromechanical counter is advanced one digit. The division factor is wired in at the factory or can be programmed in the field with optional switches.

Batch Dispenser modules couple a flow transducer and a solenoid valve to dispense a measured quantity of fluid on command. The cycle is initiated by grounding the "batch trigger" input. The solenoid valve is then opened until a pre-set number of pulses is received from the flow transducer. The valve is then shut until another trigger command is received.

Features

Model Number	Power Supply for FloScan Flow Transducer	Square Wave Output	Analog Output O-5VDC	Totalizer	Batch Dispenser	Auxiliary Power Supply 5VDC, 200mA
3001	X	X				
3002	X	X	X			X
3003	X	X		X		
3004	X	X			X	
3005	X	X	X	X		
3006	X	X	X		X	

Optional Features

A. Separate 115VAC/10VAC transformer for use with all models.
B. Field programmable division factor for 3003, 3004, 3005, or 3006.
C. Analog panel meter for use with 3002, 3005, or 3006.
D. Digital panel meter for use with 3002.

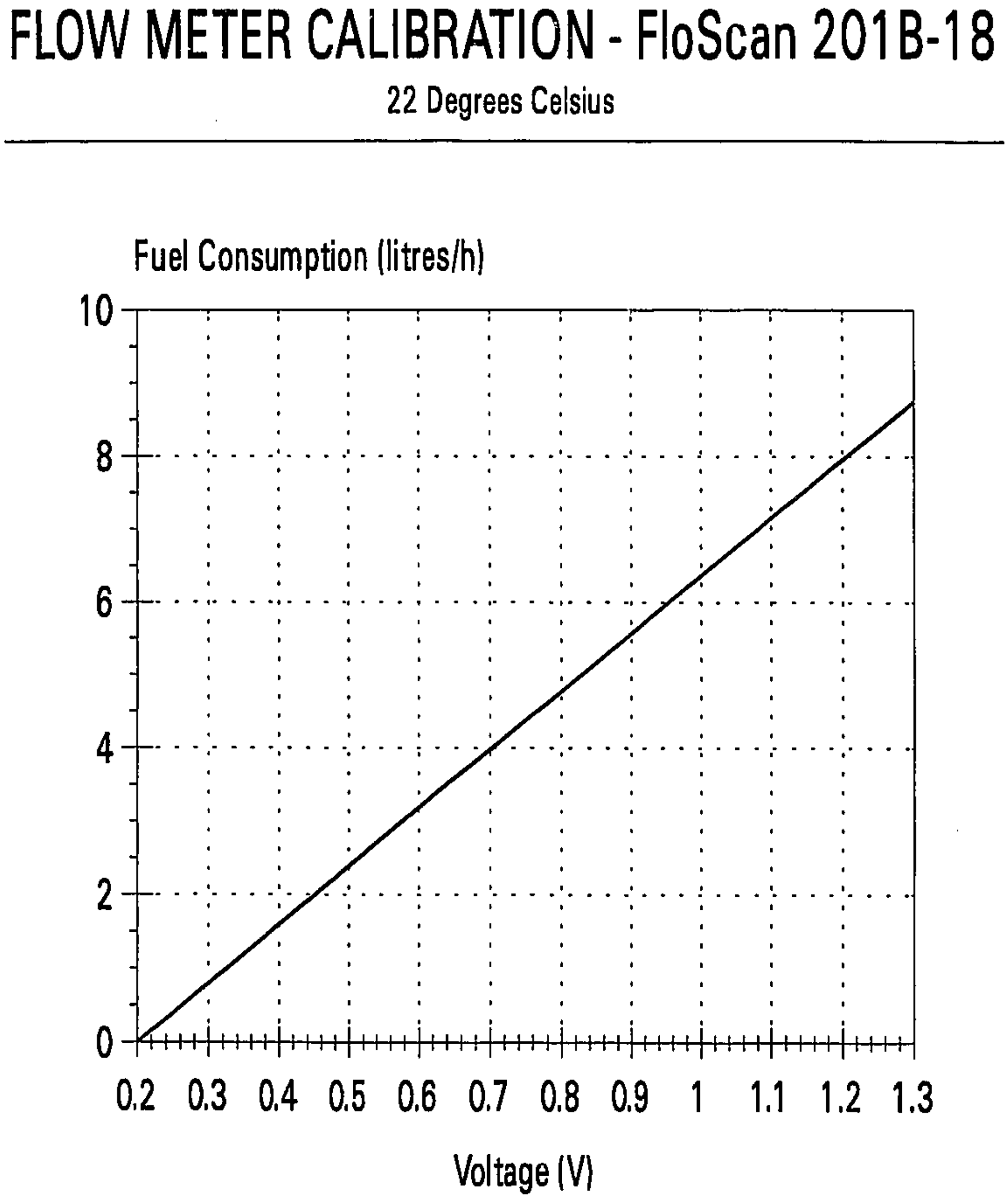

Fig. A2.1 Flow Meter Calibration Curve

APPENDIX 3

Design of the Electric Drive Shaft Extension: Stress Analysis

Reduction Ratio of electric motors (See Fig. 5.5):

$$\frac{N_2}{N_1} = \frac{N_4}{N_3} = 3 \qquad \text{(A3.1)}$$

Torque on the shaft at point A:

$$T_2 = \frac{N_2}{N_1}(T_1) = 243 N.m \qquad \text{(A3.2)}$$

Torque on the shaft at point B:

$$T_4 = \frac{N_4}{N_3}(T_3) = 174 N.m \qquad \text{(A3.3)}$$

Radius of the driven sprockets:

$$R_S = \frac{N_2 \cdot Pitch}{2\pi} = 0.091\, m \qquad \text{(A3.4)}$$

where: $N_2 = N_4 = 36$ tooth
T_2 = Advanced DC electric motor peak torque (81 N·m)
T_3 = Solectria electric motor peak torque (51 N·m)
Pitch = Sprocket pitch 0.0158 m

<u>Assumption</u>: Slack side of the chain for both driven sprocket is assumed to be 10% of the tension side.

Force produced on the shaft by the Advanced DC driven sprocket was calculated as follows:

Force on Tension side (Advanced DC):

$$F_{AS} = \frac{T_2}{R} = 2670 N \qquad \text{(A3.5)}$$

Force on Slack side (Advanced DC):

$$F_{AS} = 0.1F_{AT} = 267N \tag{A3.6}$$

Total force produced by Advanced DC:

$$F_{AD} = F_{AT} + F_{AS} = 2937N \tag{A3.21}$$

Force produced on the shaft by the Solectria motor driven sprocket;
Tension side:

$$F_{ST} = \frac{T_4}{R} = 1912N \tag{A3.22}$$

Slack Side:

$$F_{SS} = 0.1F_{ST} = 191N \tag{A3.23}$$

Total force produced by Solectria:

$$F_S = F_{ST} + F_{SS} = 2103N \tag{A3.24}$$

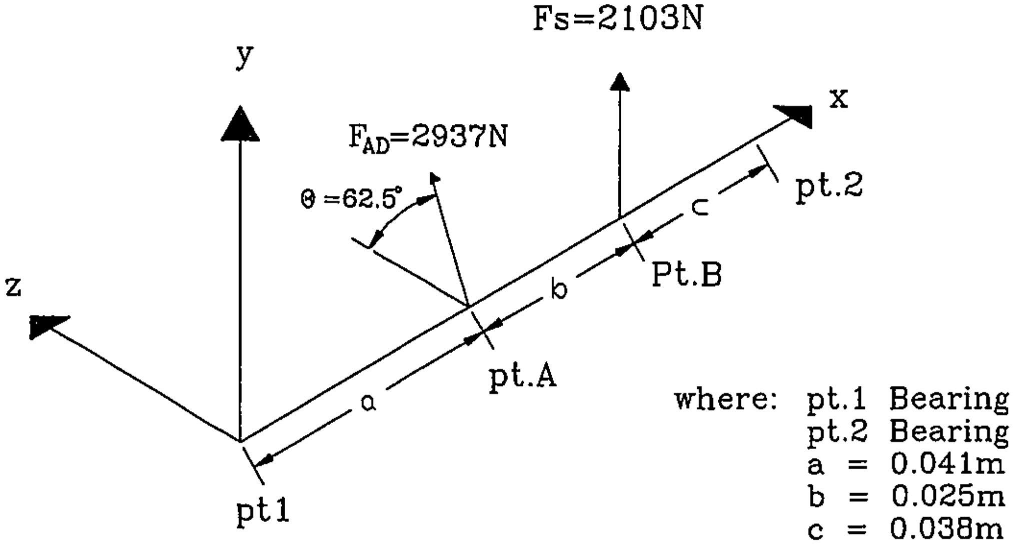

where: pt.1 Bearing
pt.2 Bearing
a = 0.041m
b = 0.025m
c = 0.038m

Fig. A3.1 Free Body Diagram

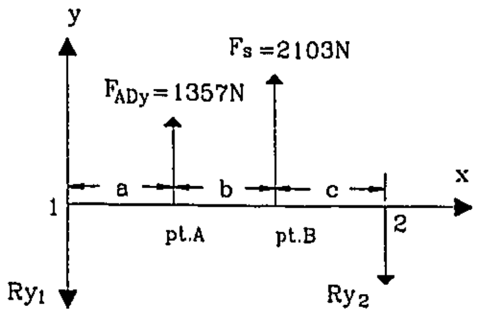

Fig. A3.2 Free Body Diagram X-Y Axes

$$F_{AD_y} = F_{AD} \cdot \cos 62.5^{o} = 1357N$$

Using moment about point 1 and point 2, the following reactions were solved:

$$R_{y2} = 1869.5N$$

$$R_{y1} = 1590.5N$$

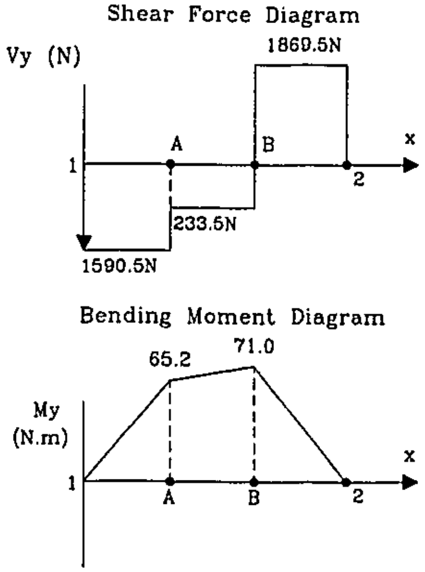

Fig. A3.3 Shear Force and Bending Moment Diagram X-Y Axes

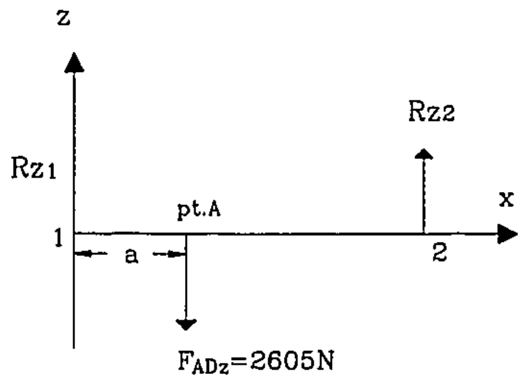

Fig. A3.4 Free Body Diagram X-Z Axes

$$F_{AD_z} = F_{AD} \cdot \sin 62.5^o = 2605N$$

Using moment about point 1 and point 2, the following reactions were solved:

$$R_{z2} = 1027N$$

$$R_{y1} = 1578N$$

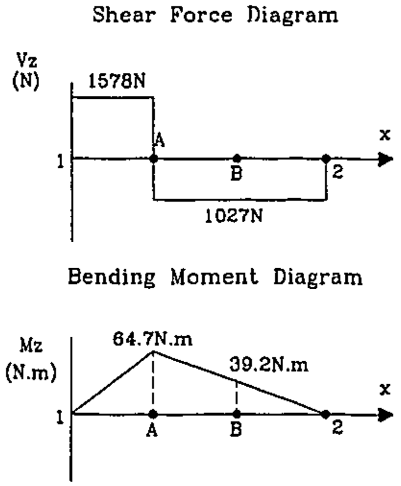

Fig. A3.5 Shear Force and Bending Moment Diagram X-Z Axes

Point A worst loaded analysis on element k

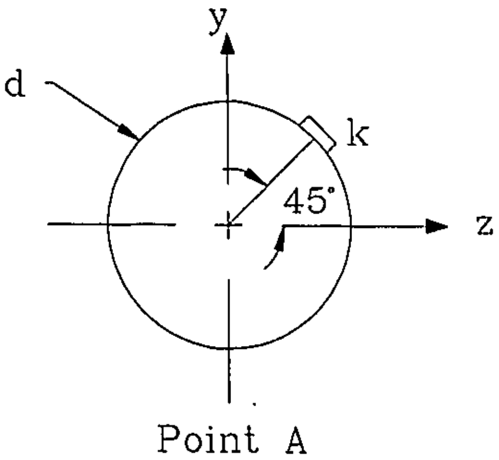

Fig. A3.6 Shaft Cross Sectional Area at Point A

where: $I_y = I_z$ (second moment of area about y axis and z axis, respectively)

$$I_z = \frac{\pi d^4}{64}, \quad C = \frac{d}{2} \tag{A3.11}$$

Point A

$$\sigma_{m_z} = \frac{M_{zA} \cdot C}{I_z} = \frac{659.1}{d^3} \tag{A3.12}$$

$$\sigma_{m_y} = \frac{M_{yA} \cdot C}{I_y} = \frac{664.1}{d^3} \tag{A3.13}$$

Using Distortion Energy Theorem:

$$\sigma_m = \sqrt{(\sigma_{m_z})^2 + (\sigma_{m_y})^2 - \sigma_{m_z}\sigma_{m_y}} \tag{A3.14}$$

Substituting equations (A3.12), and (A3.13) into (A3.14) yields the following:

$$\sigma_m = \sqrt{(\frac{659.1}{d^3})^2 + (\frac{664.1}{d^3})^2 - (\frac{437708.3}{d^6})}$$

Alternating stress component is calculated by assuming, 8 g's acting on mass of Advanced DC electric motor (m_{AD}).

Alternating force component:

$$F_a = m_{AD} 8(g) = 7848 N \tag{A3.15}$$

Alternating stress:

$$\sigma_a = \frac{F_a}{\frac{\pi d^2}{4}} = \frac{9992}{d^2} \tag{A3.16}$$

The Soderberg equation for infinite life:

$$\frac{\sigma_a}{S_e} + \frac{\sigma_m}{S_{yt}} = \frac{1}{n} \tag{A3.17}$$

where: $n = 3.5$ safety factor

Shaft material: SAE 1006 $S_{yt} = 170$ MPa

$k_e = 1/k_f$

$k_f = 3.0$ stress concentration factor for shaft keyway

$k_a = k_b = k_c = k_d = 1$ (Assumption)

$Se' = 0.5\ S_{yt}$ = endurance limit of a test specimen.

Se = endurance limit

Solving the Soderberg equation (A3.17):

$$\frac{\frac{9992}{d^2}}{28.3x10^3} + \frac{\sqrt{(\frac{659.1}{d^3})^2 + (\frac{664.1}{d^3})^2 - (\frac{427708.3}{d^6})}}{170x10^6} = \frac{1}{3.5}$$

The shaft diameter for infinite life was calculated to be:

$$d = 39.73 mm = 40 mm$$